Final Report

Project Title: Effects of Impurities on Fuel Cell Performance and Durability

Project Period: March 1, 2007 – August 31, 2011

Date of Report: December 30, 2011

Recipient: The University of Connecticut

Award Number: DE-FG36-07GO17020

Working Partners: The University of Connecticut – Center for Clean Energy

Engineering, FuelCell Energy, Inc., United Technologies - Hamilton Sundstrand

Cost-Sharing Partners: The University of Connecticut – Center for Clean Energy

Engineering, FuelCell Energy, Inc., United Technologies – Hamilton Sundstrand

Contact: Trent M. Molter

Associate Research Professor and Business Development Officer The Connecticut Global Fuel Cell Center – The University of

Connecticut

44 Weaver Rd. Unit 5233

Storrs, CT 06269

Phone: (860) 486-2898; Fax: (860) 486-8378

E-mail: tmolter@engr.uconn.edu

DOE Managers: DOE Technology Development Manager: Nancy Garland

Phone: (202) 586-5873; Fax: (202) 586-9811

E-mail: Nancy.Garland@ee.doe.gov

DOE Project Officer: Reg Tyler

Phone: (303) 275-4929; Fax: (303) 275-4753

E-mail:Reginald.Tyler@go.doe.gov

Project Objective: This program is focused on the experimental determination of the effects of key hydrogen side impurities on the performance of PEM fuel cells. Experimental data will be leveraged to create mathematical models that predict the performance of PEM fuel cells that are exposed to specific impurity streams. These models will be validated through laboratory experimentation and will be utilized to develop novel technologies for mitigating the effects of contamination on fuel cell performance. Results will be publicly disseminated through papers, conference presentations, and other means.

Background: While Proton Exchange Membrane (PEM) fuel cells show significant promise to provide efficient, clean power for stationary and transportation applications, today's technology falls short of meeting existing and contemplated product performance and durability standards. One of the limiting factors is that the operational lifetime of membrane electrode assemblies (MEA's) becomes reduced when impurities are introduced into the system. These impurities impact the functionality of ion exchange groups within the electrolyte, degrade catalyst activity, and function as a diluent for the fuel and oxidant stream thereby negatively impacting overall cell efficiency and operational performance.

The initial technical issues being addressed concern the identification of impurity species located in the fuel stream that may have an effect on overall fuel cell performance, and evaluation of these effects against standard test protocols. The U.S. Fuel Cell Council in conjunction with JARI and others have been developing hydrogen quality standards as well as procedures for impurity testing of PEM fuel cells. These studies provide the background and basis for the initiation of our research.

Program Structure: This program is organized around 7 major tasks further broken down in to more detailed levels of effort. A summary of the major tasks and accompanying development objectives are provided in the chart below.

Task	Objectives
1.0 Contaminant	 Identify specific contaminants and contaminant families present in both fuel and
Identification	oxidant streams.
2.0 Analytical Method	 Development of analytical methods to study contaminants.
Development	 Experimental design of analytical studies.
	 Novel in situ detection methods.
3.0 Contaminant	 Develop contaminant analytical models that explain these effects.
Studies	 Establish an understanding of the major contamination-controlled mechanisms that cause material degradation in PEM cells and stacks under equilibrium and especially dynamic loading conditions
4.0 Contaminant Model Development	 Construct material state change models that quantify that material degradation as a foundation for multiphysics modeling Establish the relationship between those mechanisms and models and the loss of PEM performance, especially voltage decay
5.0 Contaminant Model Validation	 Validate contaminant models through single cell experimentation using standardized test protocols.
6.0 Novel Mitigation Technologies	 Develop and validate novel technologies for mitigating the effects of contamination on fuel cell performance.
7.0 Outreach	 Conduct outreach activities to disseminate critical data, findings, models, and relationships etc. that describe the effects of certain contaminants on PEM fuel cell performance.

Progress relative to each of these tasks is shown below.

Task 1.0 Contaminant Identification

This major program activity has involved identifying which contaminants the fuel cell will be exposed to during normal operation for both stationary and transportation applications. This has been done by deriving input from ongoing DOE development activities and historical data relative to operational demonstrations. This has included coordination with activities supported by the U.S. Fuel Cell Council including efforts to identify the appropriate fuel specification for transportation-based fuel cell applications.

<u>Organic Impurities</u> - Through technical interchange activities and coordination with other laboratories investigating the effects of impurities on fuel cell performance, our team focused on the evaluation of hydrocarbons and halogenated compounds using very specific test protocols developed as part of a multi-laboratory collaborative effort. The focus has been on evaluating simple hydrocarbons such as methane and ethane, ethylene, formaldehyde, acetaldehyde, and formic acid.

Our strategy is to evaluate molecules that may be present in a candidate hydrogen fuel stream in order of both functionality and molecular size (eg. # of carbon atoms). These classes of impurities are shown in Figure 1 below.

In support of the development of a fuel quality standard in the Fall of 2009, early evaluations focused on formaldehyde and formic acid at very low concentrations, as well as an evaluation of a simple halogenated hydrocarbon (chloromethane, for example). In addition, prior studies have suggested that there may be synergistic effects of CO₂/CO on fuel cell performance. These effects are mapped as part of this activity.

Specifications for Draft CD

ISO/SAE Specs	
99.97+	
4 ppb	
.2 ppm	
2 ppm	
.1 ppm	
2 ppm	
1 ug/L (10 um size)	
<.03% (300ppm)	
5 ppm	
5 ppm	
300 ppm	
100 ppm	
10 ppb	
.2 ppm	
50 ppb	

Figure 1 Impurity Evaluation Process – Items in Red Are Our Research Focus

<u>Cationic Impurities</u> - Our team has further focused on the evaluation of different metallic cation contaminants on the fundamental properties of perfluoroionomer membranes (gas/water permeability, ionic conductivity, mechanical properties, etc.). Our initial efforts have focused on investigating group IA ions with the goal of establishing whether contaminant atomic mass substantially affects membrane properties. Further studies have focused on common multivalent metal cations including Ca, Mg, Ni, Fe, Al, Cu, and Cr. Recent efforts have focused on more closely examining the effects of more dilute cation concentrations on membrane properties. Membrane physio-chemical properties were measured as part of this process, including gas transport, mechanical properties and ionic conductivity.

Task 2.0 Analytical Method Development

Based on the nature and levels of impurities identified in Task 1.0, our team has developed techniques to regulate the levels of contamination entering the fuel cell through the hydrogen stream. We have also developed techniques to determine the fate of these contaminants through exit stream analysis and post mortem analysis to assess contaminant accumulation. In this regard, both a gas chromatograph and a mass spectrometer have been inserted into the system in order to investigate the effects of these impurities on fuel cell performance. In order to achieve this, a gas drier has been added to the system to remove water vapor prior to the chromatographic analysis without disturbing the concentration of contaminant fed to the cell.

The system schematic is shown in Figure 2.

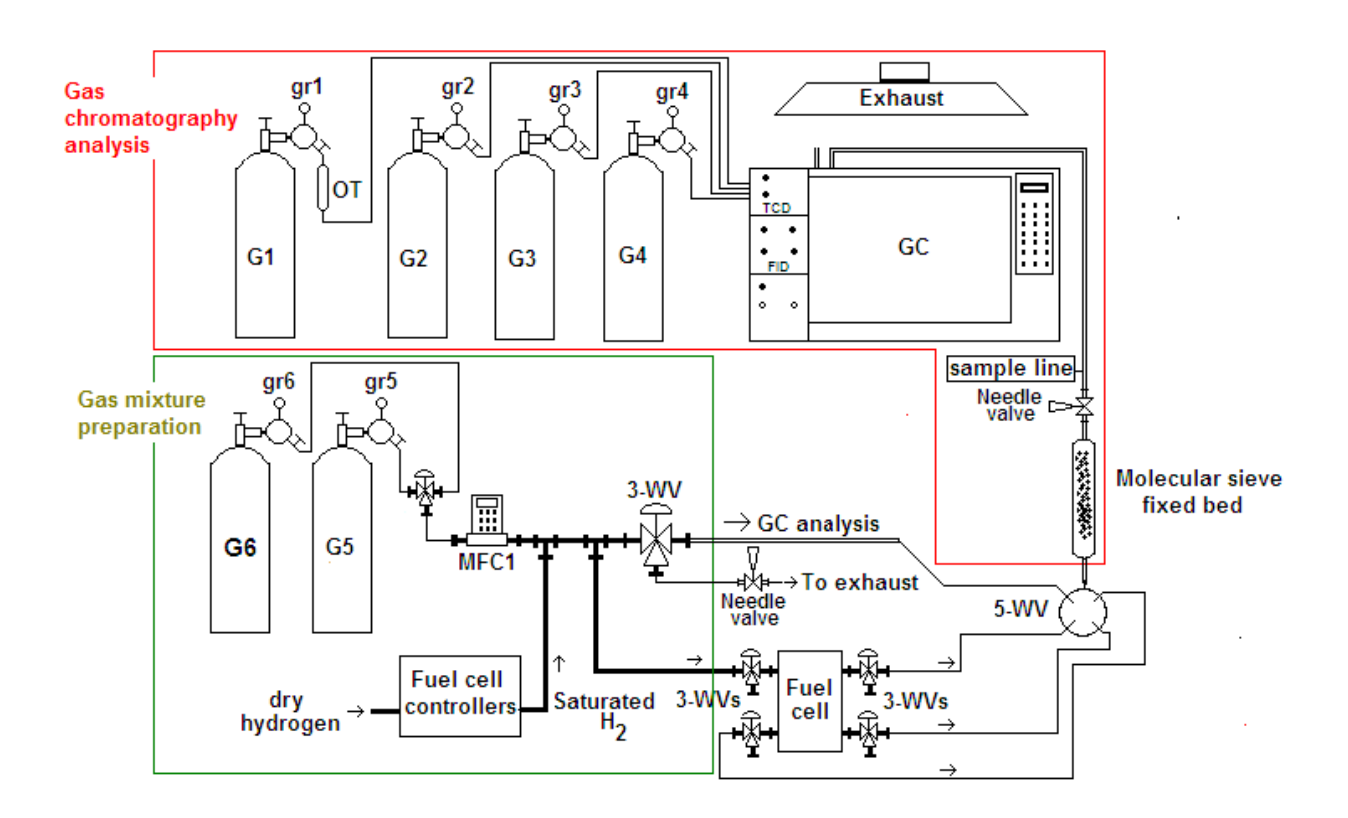


Figure 2 System Schematic for Fluids Mixing and Analysis

While the gas mixture needs to be humidified in order for the fuel cell to function properly, a slip stream is taken from this mixture and must be dried prior to analysis.

This process is critical and must be carried out without removing the impurity from the fluids stream. Several drying agents and techniques were evaluated as part of this process and a molecular sieve material was chosen. The data pertaining to each of these candidate materials is shown in Table I.

Table I Candidate Drying Agents

Material	Description	Geometry Particle size (mesh)	H₂0 Adsorption Capacity (% weight)	Temperature regeneration (°C)	Applications	Temperature Operation (°F)
Molecular sieve	Type 3A Pore diameter 3A	Beads 8-12 4-8	22 (60 °F and 40 % RH)	175-260	Natural gas drying CO ₂ and NH ₃ removal	30-200
Silica gel	Orange indicator	Pearls	30 (77 °F and 80 % RH	130-160		
Drierite	Moisture indicator	Irregular 4,6,8	26	180-200		

A swing-bed system has been constructed to remove water from the hydrogen fuel stream. The features of this design are shown below in Table II.

Table II Features of the Molecular Sieve Bed

Feature	Description
Length of packed bed	250 cm
Weight of packed molecular sieve	78 g
Flow rate control	Backpressure control using a needle valve
Tubing diameter	7.1 mm
Humidity indicator	Drierite with indicator
Water adsorption (60°F and 40% R.H)	17.71 g
Water adsorption under fuel cell conditions (rough calculation based on 10 % of the data reported before)	1.771 g
Drop pressure at room temperature > 2 sccm > 5 sccm > 7.5 sccm > 10 sccm > 15 sccm > 20 sccm	0.00 psi 0.07 psi 0.10 psi 0.11 psi 0.12 psi 0.20 psi
Packed bed total volume (Void + occupied)	130 cm ³
Life time	11 hours (2.7 atm, 80 °C, 100 % R.H., 5 sccm dry gases, 10 % adsorption)
Residence time 2 sccm 5 sccm 7.5 sccm	45 min 18 min 12 min

A photograph of part of the system used for fluids analysis is shown in Figure 3.

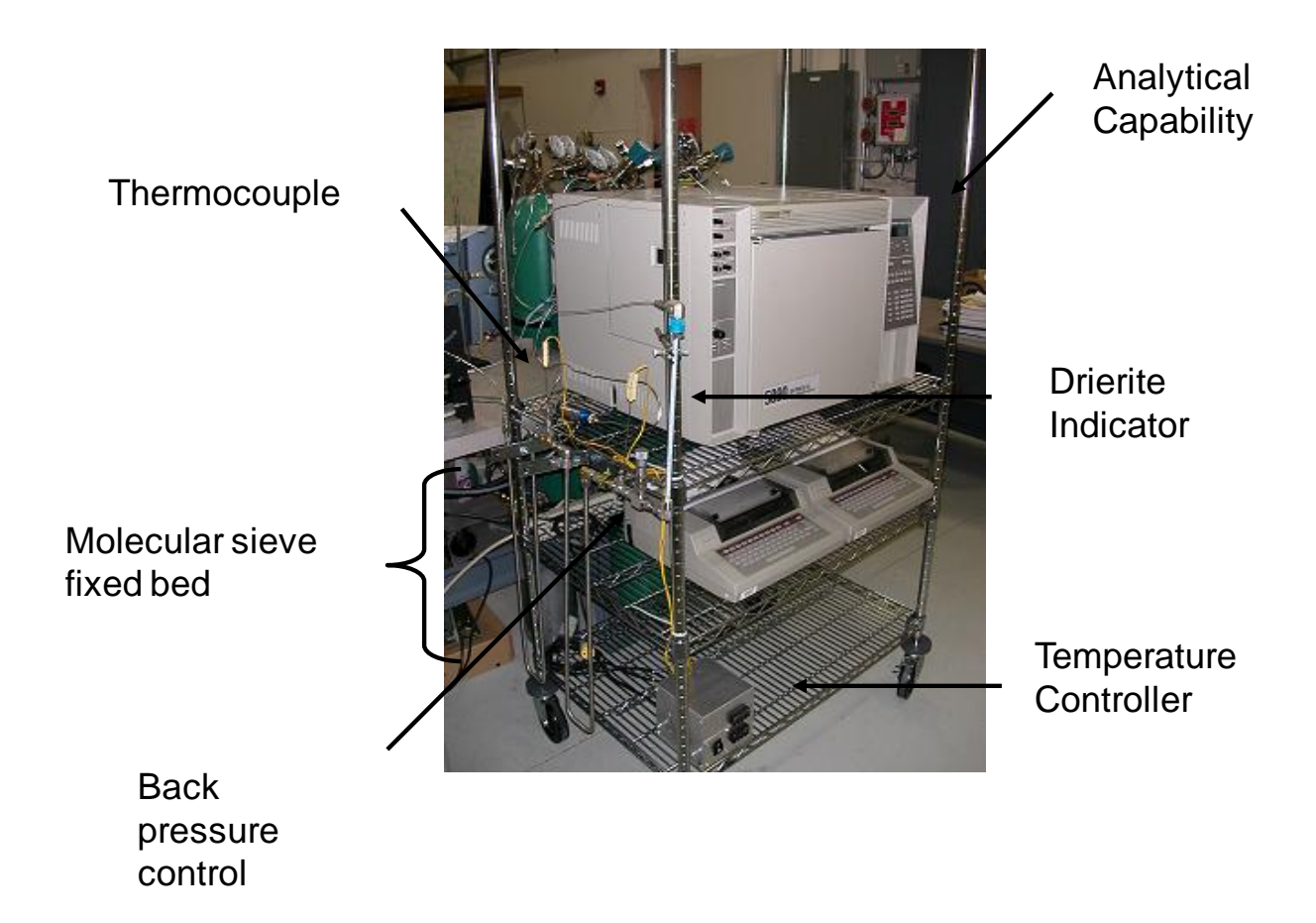


Figure 3 Photograph of Gas Chromatograph Utilized in Fluids Analysis

Since we are dealing with a variety of hydrocarbons, ie. those that are gaseous, and those that are liquid, we have tailored both our mixing process and our analysis process to the specific impurity of interest.

For simple gaseous hydrocarbons, we have obtained standard gas mixtures and diluted these mixtures with hydrogen prior to introducing them to the fuel cell. Our gas chromatograph has been modified for hydrocarbon analysis in accordance with the features and parameters set forth in Table III. These are the parameters utilized for the analysis of methane, ethane, and ethylene.

Table III Gas Chromatography Parameters Utilized for the Analysis of Methane, Ethane and Ethylene

Feature	Description
Carrier gas flow rate	3 ml/min
Oven temperature program	130 °C isothemal
Injector and auxiliary temperature	180 °C
Detector temperature	200 °C
Mode of operation	Split, split ratio 30:1
Sample loop volume	100 µl
Type of column	Carbonplot 1010
Detector	FID (flame ionization detector)

During testing, we track the variability in concentration of the impurity in the injected hydrogen fuel mixture. Figure 4 shows this variability for methane, and similarly, Figure 5 shows this variability for ethane.

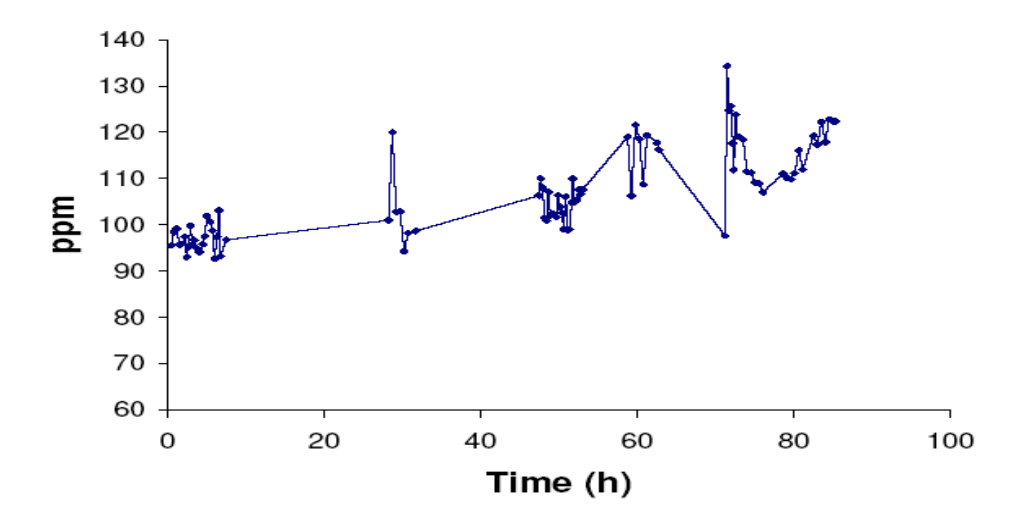


Figure 4 Variability in Concentration of Methane in Hydrogen Fed to the Fuel Cell Over a 100-Hour Test Period (Target Concentration 100 ppm)

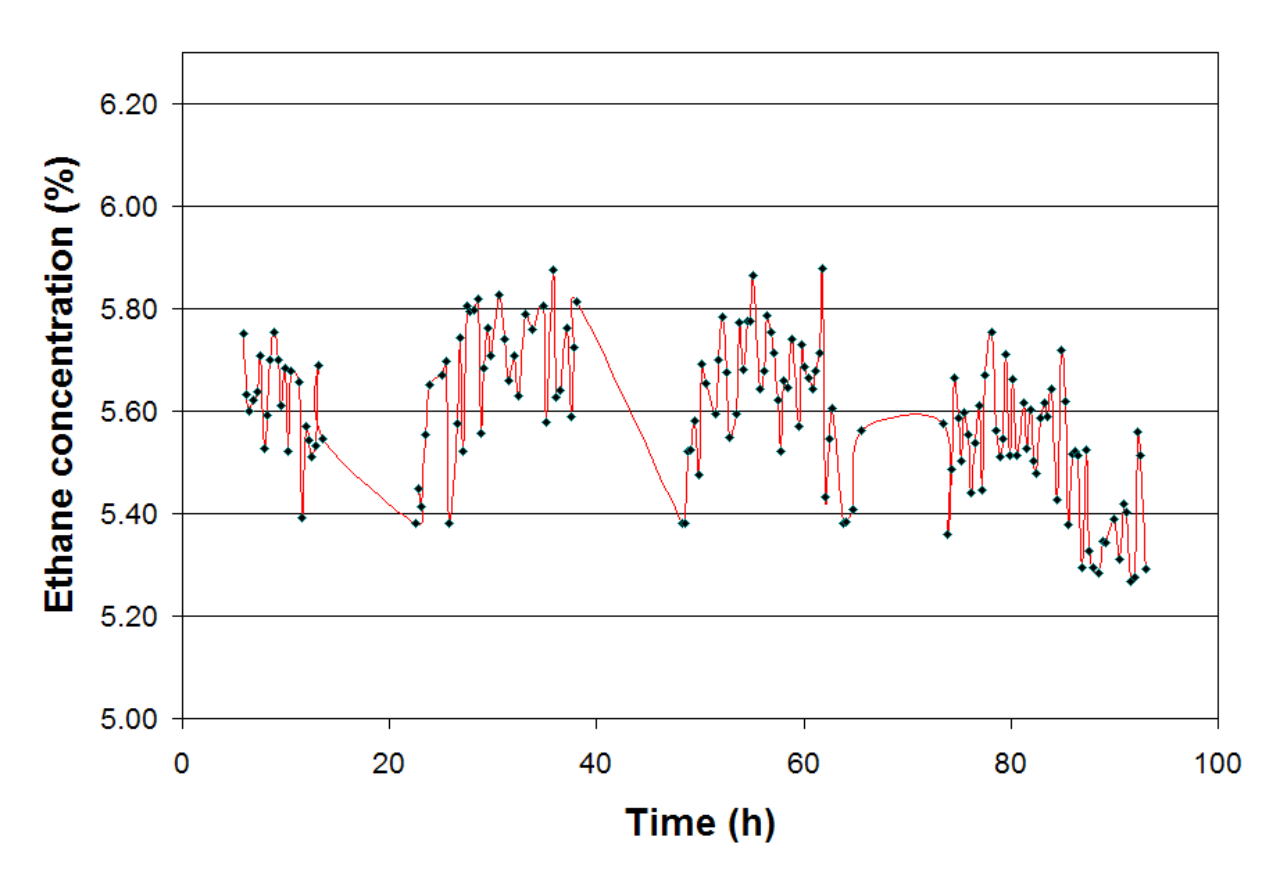


Figure 5 Variability in Concentration of Ethane in Hydrogen Fed to the Fuel Cell Over a 100-Hour Test Period (Target Concentration 5%)

These data demonstrate both the mixing and analysis requirements for very different ranges of concentration demanded by our test matrix.

Other impurities normally in a liquid phase require an alternate means of mixing and analysis. In this regard, we injected the liquid impurity into a heated line to force this constituent into the vapor phase. The vaporized impurity was then metered into the hydrogen stream that enters the fuel cell. A different arrangement for analysis using a gas chromatograph was required for evaluating acetaldehyde; an impurity that normally is in the liquid state. The critical parameters for operation of the gas chromatograph are shown in Table IV.

Table IV Gas Chromatography Parameters Utilized for the Analysis of Acetaldehyde

Feature	Description
Carrier gas flow rate	12 ml/min
Oven temperature program	100 °C isothermal
Injector and auxiliary temperature	150 °C
Detector temperature	250 °C
Mode of operation	Splitless mode
Sample loop volume	1 cc
Type of column	1/8 empty ss tube, 2 m length
Detector	FID (flame ionization detector)

In a similar manner to methane and ethane, the concentration of acetaldehyde was plotted during a 100 hour experiment (Figure 6). The target concentration for this test was 30 ppm.

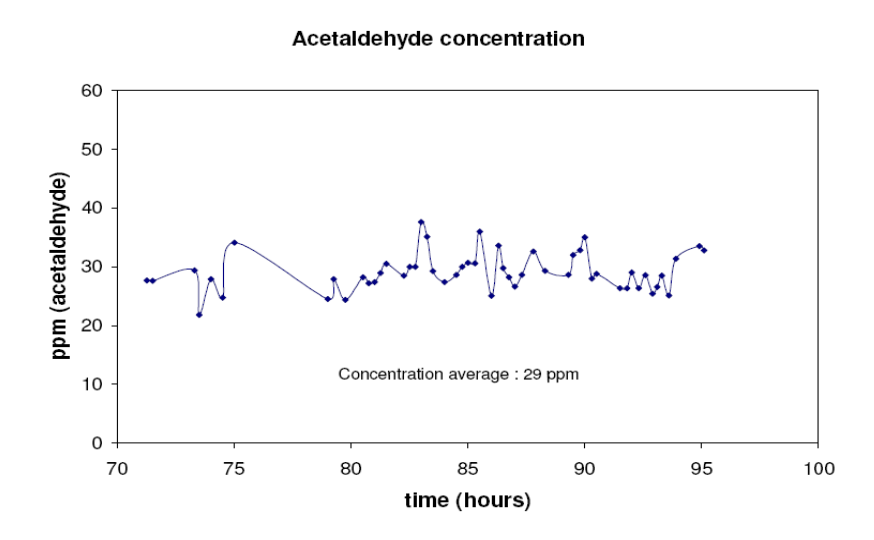


Figure 6 Variability in Concentration of Acetaldehyde in Hydrogen Fed to the Fuel Cell Over a 100-Hour Test Period (Target Concentration 30 ppm)

We injected the liquid impurity into a heated line to force this constituent into the vapor phase. The vaporized impurity is then metered into the hydrogen stream that enters the fuel cell. Figure 7 shows the saturator apparatus that we have developed to accomplish this task. A different arrangement for analysis using a gas chromatograph is required for evaluating acetaldehyde, formic acid and formaldehyde; impurities that normally are in the liquid state.

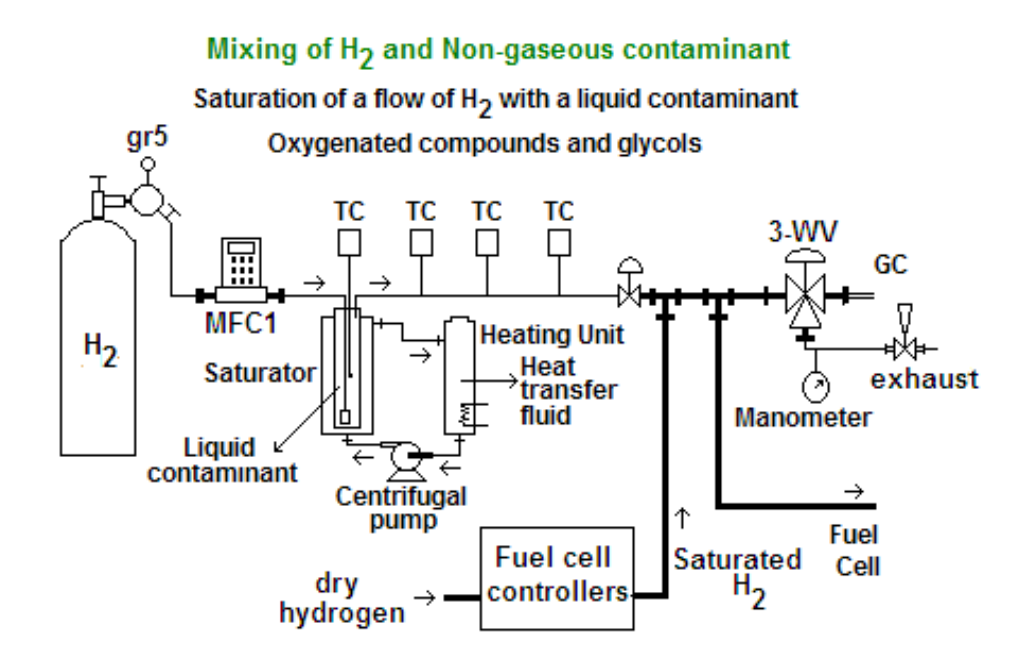


Figure 7 Gas Mixing Set-Up for Liquid Hydrocarbons

Because we utilized various organic impurities in our test equipment, and often switching between impurities, we realize that organics have the propensity to "stick" to the inner surfaces of process fittings, tubing, etc. and therefore needed to remove these impurities between runs.

A 5 sccm slip stream of sample was sent continuously through a sample loop located on the top of the gas chromatograph. The use of this sample loop assures that the same amount of sample will be always used for the analyses to minimize experimental errors. The volume of the sample loop is a critical variable for the analysis and its effect is measured indirectly using the peak geometry produced by the recorded signal. The calibration is achieved with certified standard mixtures in the case of gases, and with saturated hydrogen under controlled temperature and pressure for liquid impurities.

Nuclear Magnetic Resonance (NMR)

The spectroscopic identification of the condensate compounds in the anode and cathode sides of the fuel cell during impurity testing was evaluated through nuclear magnetic resonance (NMR). A schematic of the experimental set-up is presented in Figure 8. The condensate for evaluation was collected in both sides at different times

during the 100 h run contamination experiments. Collection of the sample for the analysis is done without any perturbation of the cell operation conditions. In each case the characteristic signals for the organic compound under evaluation was monitored.

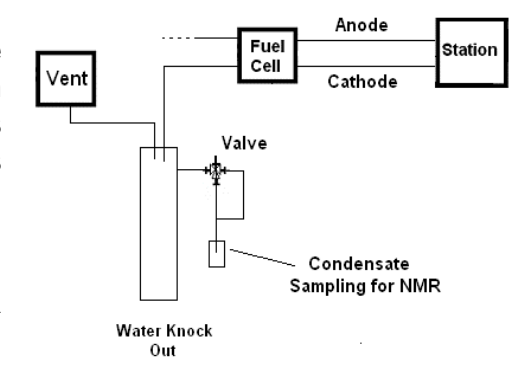


Figure 8 Experimental Set-up for NMR Evaluation of Condensates

The vapor pressure data as a function of temperature is calculated according to:

Vapor Pressure = $exp[C1 + (C2/T) + C3*In(T) + C4*T^{C5}]$

Table V presents the Ci constants for some of the organic liquids evaluated with this experimental setup.

	C1	C2	C3	C4	C5
Formic Acid	101.51	-4917.2	-13.765	2.2031E-02	1
Ethylene Glycol	79.276	-10105	-7.521	7.3408E-19	6
Propylene Glycol	212.8	-15420	-28.109	2.1564E-05	2

Table V Vapor Pressure of Organic Liquids

Specific testing involved the preparation and characterization of mixtures acetaldehyde-hydrogen and formic acid-hydrogen that were fed to the fuel cell. Both formic acid and acetaldehyde mixtures were prepared at two different concentrations: 30 and 100 ppm for acetaldehyde-hydrogen and 50 and 100 ppm for formic acid-hydrogen.

Due to the differences in vapor pressure for acetaldehyde and formic acid, two different setups were used to prepare the mixtures with hydrogen under the specified compositions to carry out the tests for each component. Acetaldehyde was prepared using a certified gas mixture with hydrogen. The concentration of acetaldehyde for this

mixture was 600 ppm and the setup was utilized to dilute this mixture by mixing with pure hydrogen. The dilutions for both required concentrations 30 and 100 ppm and were run in accordance with the material balances applied around the point of mixing. In the case of formic acid (lower vapor pressure than the acetaldehyde), a saturator was designed and built to conduct the mixing. In order to prepare the mixtures of formic acid-hydrogen, the material balances and saturation conditions were imposed using a specific temperature in the saturator. The minimum temperature used in the saturator is constrained by the melting point of formic acid, which is 15°C.

Figure 9 shows the diagram used to apply material balances for acetaldehyde and the results for concentrations 30 and 100 ppm. Figure 10 depicts the materials balances for formic acid and the schematic of the system used to complete the mixing. The saturator contains liquid formic acid in which pure hydrogen is bubbled so that it can be saturated under a specific temperature. Here the temperature in the saturator is used to control the vapor pressure of this chemical and to establish a specific concentration in flowstream 1. 20° C was the saturator temperature used to run both experiments for formic acid (50 and 100 ppm). The vapor pressure for formic acid at 20° C is 0.63 psi.

Characterization of the mixtures fed to the fuel cell was carried out using gas chromatography. The gas chromatograph was first calibrated and then used to analyze the composition for the two impurities of interest. Sampling was performed every fifteen minutes during the test period (100 hours). The data provided by this technique are shown in Figures 11 to 14 for each one of the conditions used during the testing. Figure 11 to 14 show some acceptable fluctuations of the concentrations around the required levels.

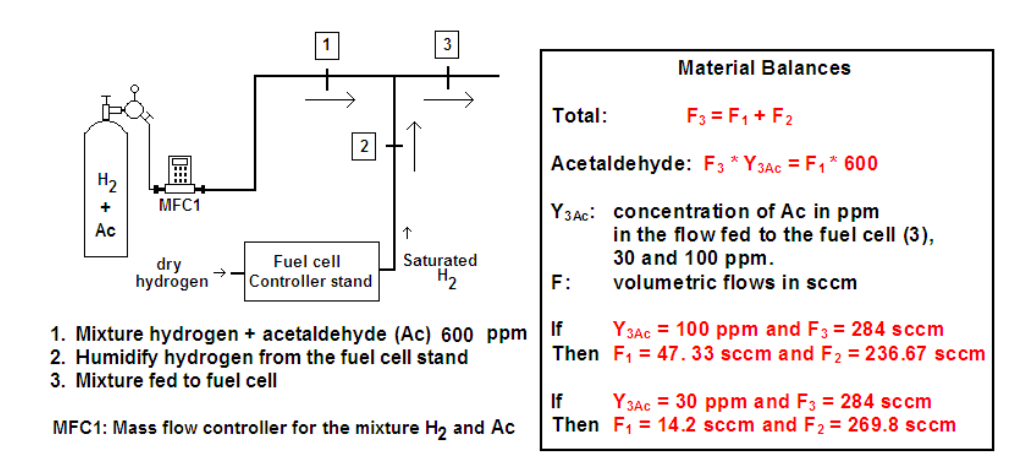


Figure 9 Material Balances for Acetaldehyde Having Concentrations of 30 and 100 ppm in the Flow Fed to the Fuel Cell

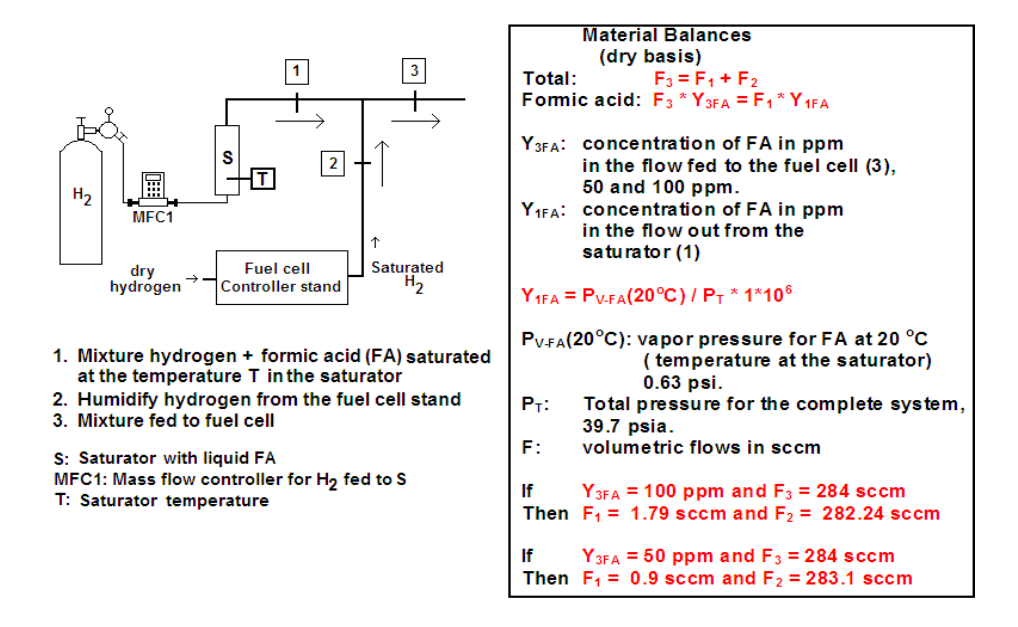


Figure 10 Material Balances for Formic Acid Having Concentrations of 50 and 100 ppm in the Flow Fed to the Fuel Cell. The Temperature in the Saturator for Both Concentrations was 20 ° C

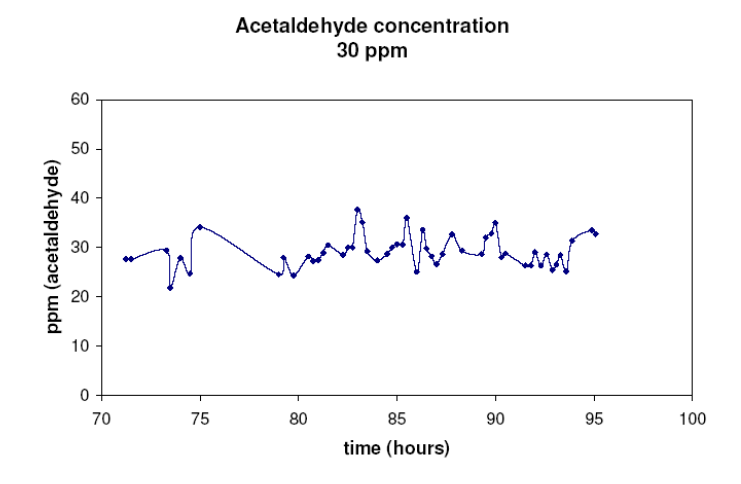


Figure 11 Concentration Data for Acetaldehyde During the Experiment at 30 ppm

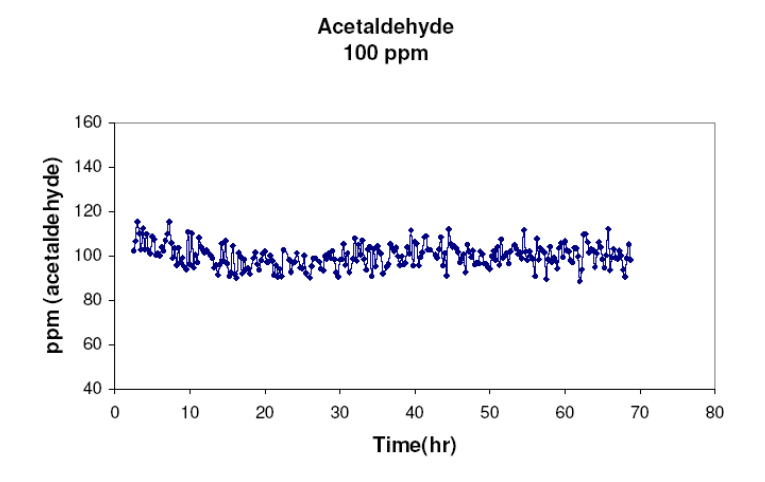


Figure 12 Concentration Data for Acetaldehyde During the Experiment at 100 ppm

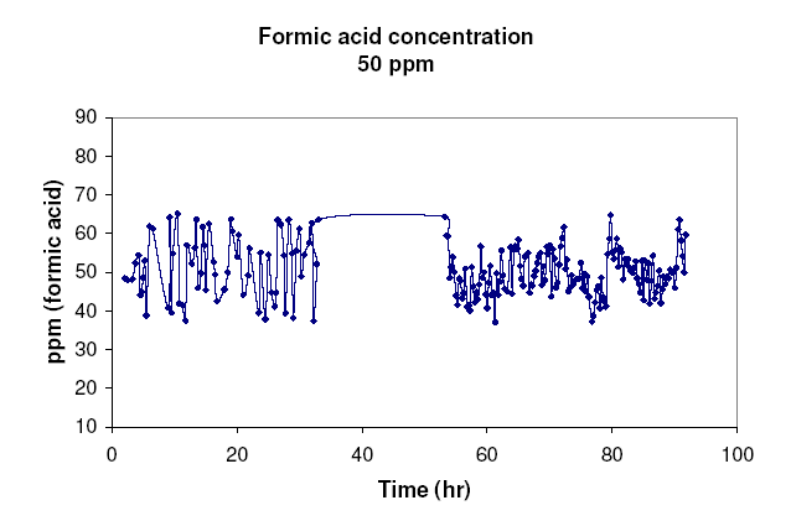


Figure 13 Concentration Data for Formic Acid During the Experiment at 50 ppm

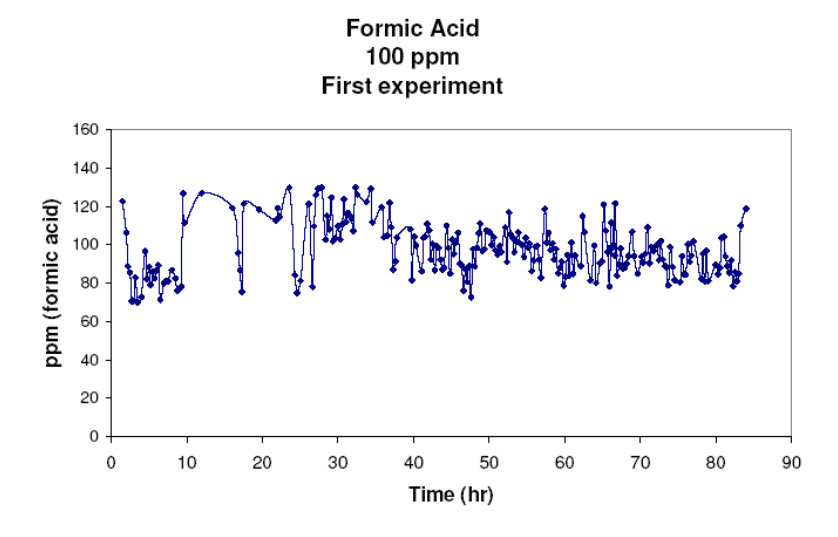


Figure 14 Concentration Data for Formic Acid During the Experiment at 100 ppm

<u>CO, CO2</u> Evaluation After Cell Contamination with Formic Acid - A gas chromatography/mass spectrometry analysis (GC/MS) is been implemented in order to determine traces of CO and CO₂ due to the oxidation of formic acid on platinum during operation of the cell. Dual pathways; dehydrogenation-dehydration, can drive the formation of these compounds as can be seen below:

Dehydrogenation: $HCOOH \rightarrow CO_2 + 2H^+ + 2e^-$

Dehydration: $HCOOH \rightarrow CO_{ads} + H_2O \rightarrow CO_2 + 2H^+ + 2e^-$

The experimental set-up for the evaluation of CO and CO2 is presented in Figure 15,

allowing continuous sampling of the gas. The gas is collected in a gas sample container without perturbation of the operating conditions of the fuel cell.

GC/MS, MS
Evaluation

Gas sampler container

Fuel Cathode

Valve

Condensate
Sampling for NMR

Water Knock

Figure 15 Experimental Set-up for CO, CO₂ Evaluation by GC/MS

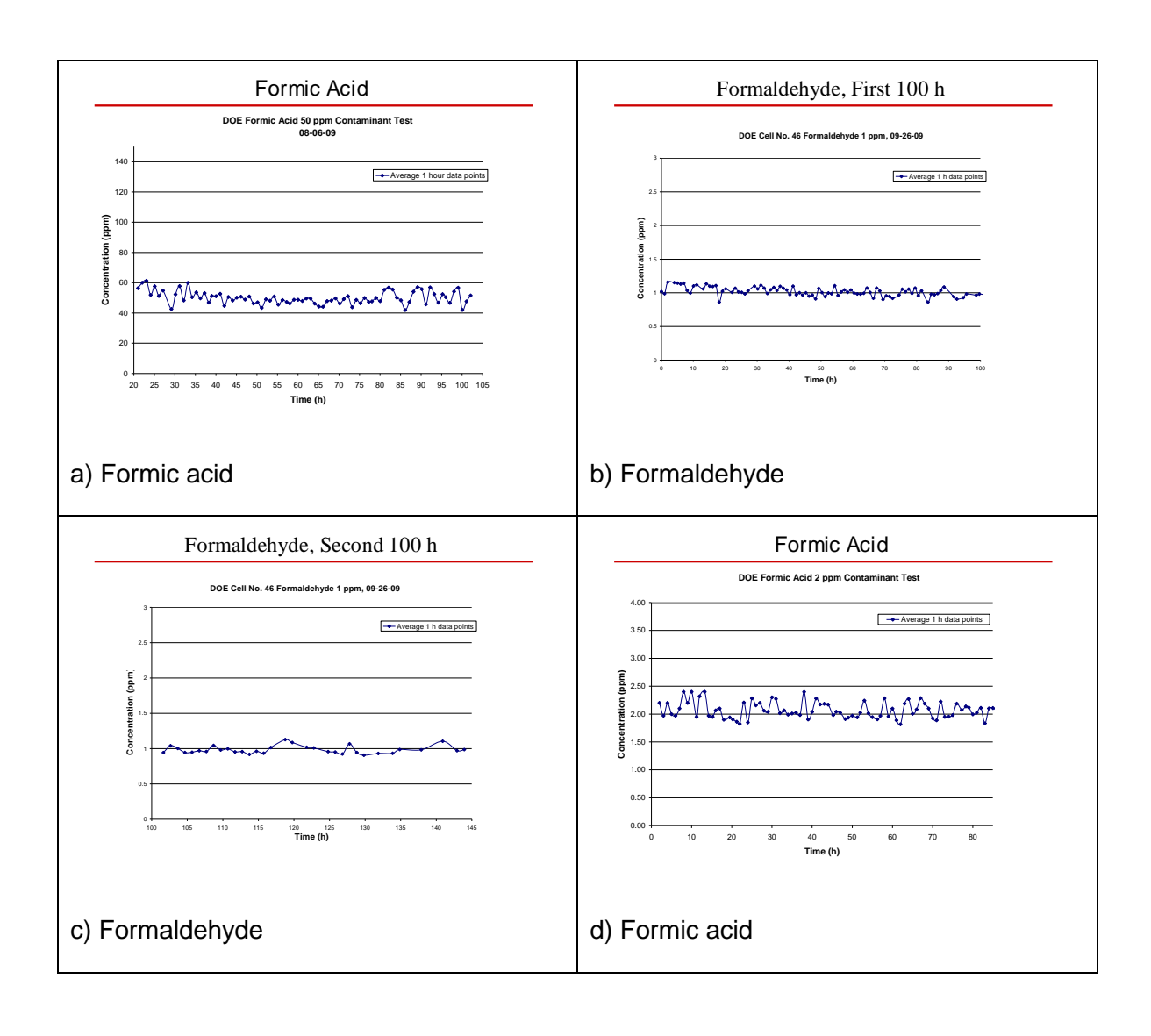
Cleaning Procedure After Impurity Evaluation - Impurities intentionally introduced to the anode of the fuel cell in the hydrogen stream have been evaluated by gas chromatography. Depending of the contaminant and concentration, a chromatography method was developed to quantify and control the feeding species. Methods were modified to feed both formaldehyde and formic acid at sub-ppm levels per the draft ISO standard. Impurities of interest are noted in Figure 16, and relevant research by ourselves and other international groups is also noted. I

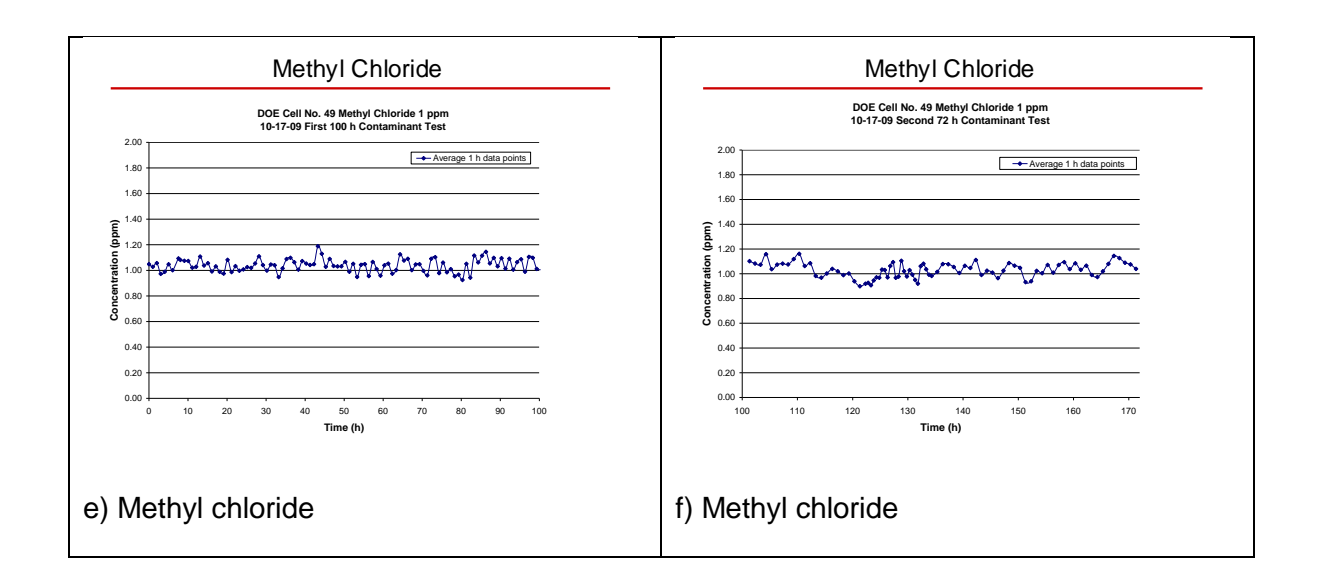
Impurity Class/Target	Tested	Concentration	Source	Result
NMHC/Total Hydrocarbons - 2 ppm	Methane	100 ppm	UCONN	
	Methane	1%	JARI	
	Methane	5%	UCONN/JARI	
	Ethane	100 ppm	JARI	
	Ethane	5%	UCONN/JARI	
	Ethylene	100 ppm	JARI	
	Ethylene	5%	UCONN/JARI	
	Acetaldehyde	30 ppm	UCONN	
	Benzene	500 ppm	JARI	
	Benzene	750 ppm	JARI	
	Benzene	1000 ppm	JARI	
	Toluene	20 ppm	HNEI	
	Methanol	500 ppm	JARI	
	Methanol	1500 ppm	JARI	
	Methanol	2000 ppm	JARI	
	Methanol	2500 ppm	JARI	
	Acetone	100 ppm	JARI	
	Acetone	250 ppm	JARI	
	Acetone	400 ppm	JARI	
	Acetone	500 ppm	JARI	
Formaldehyde - 10 ppb	Formaldehyde	1 ppm	UCONN	
	Formaldehyde	3 ppm	JARI	
	Formaldehyde	5 ppm	UCONN/JARI	*
	Formaldehyde	10 ppm	JARI	
	Formaldehyde	20 ppm	JARI	
Formic Acid - 0.2 ppm	Formic Acid	2 ppm	UCONN	
	Formic Acid	10 ppm	JARI	
	Formic Acid	20 ppm	JARI	
	Formic Acid	50 ppm	UCONN/JARI	
	Formic Acid	100 ppm	UCONN/JARI	*
	Formic Acid	500 ppm	JARI	
	Formic Acid	5%	UCONN	
Total Halogenates - 50 ppb	Methyl Chloride	1 ppm	UCONN	
	Methyl Chloride	19 ppm	UCONN	
	Perchloroethylene	0.05 ppm	SRNL	
	Perchloroethylene	1 ppm	SRNL	
	Perchloroethylene	30 ppm	SRNL	

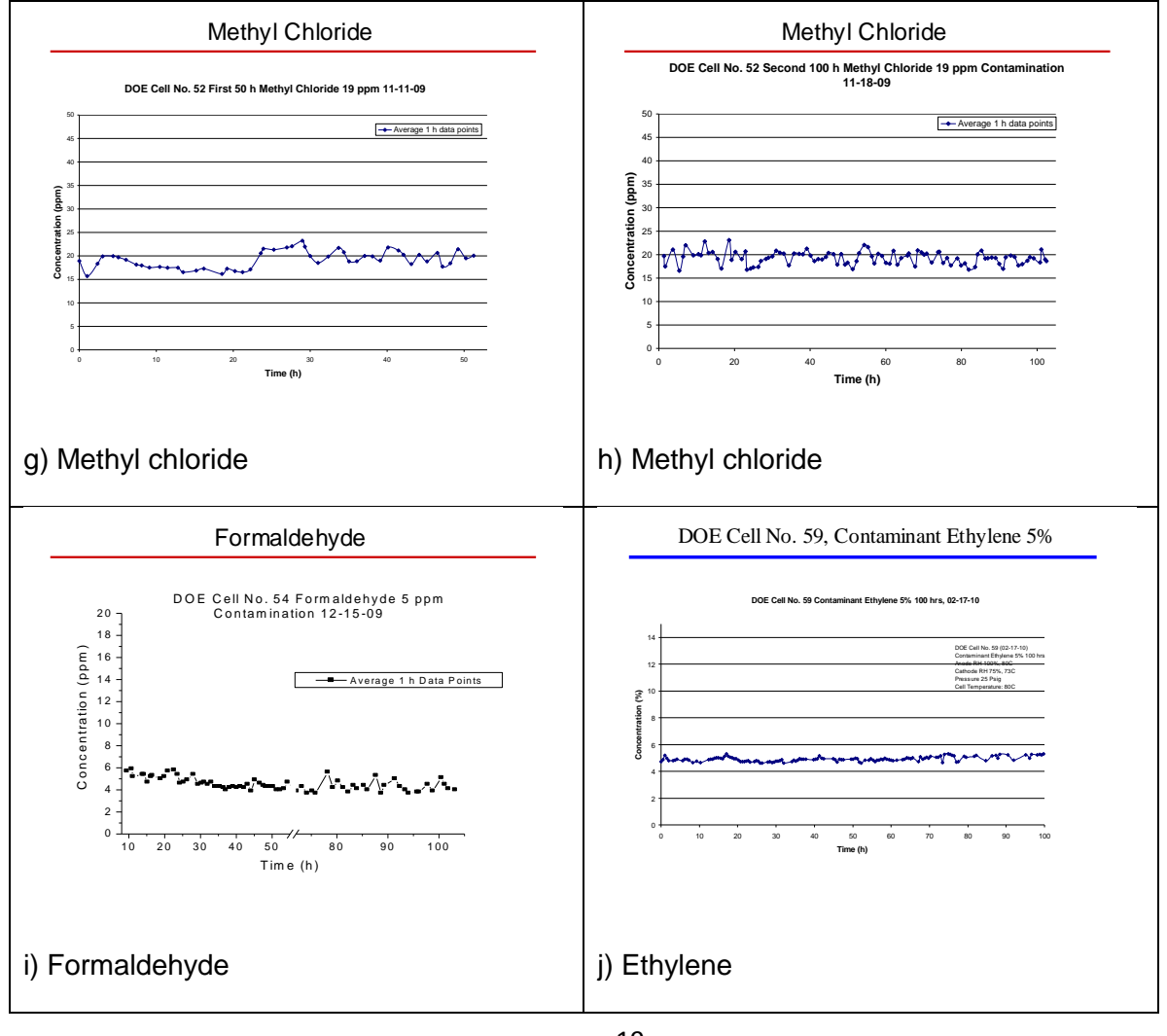
Figure 16 Draft ISO Standard and Corresponding Research

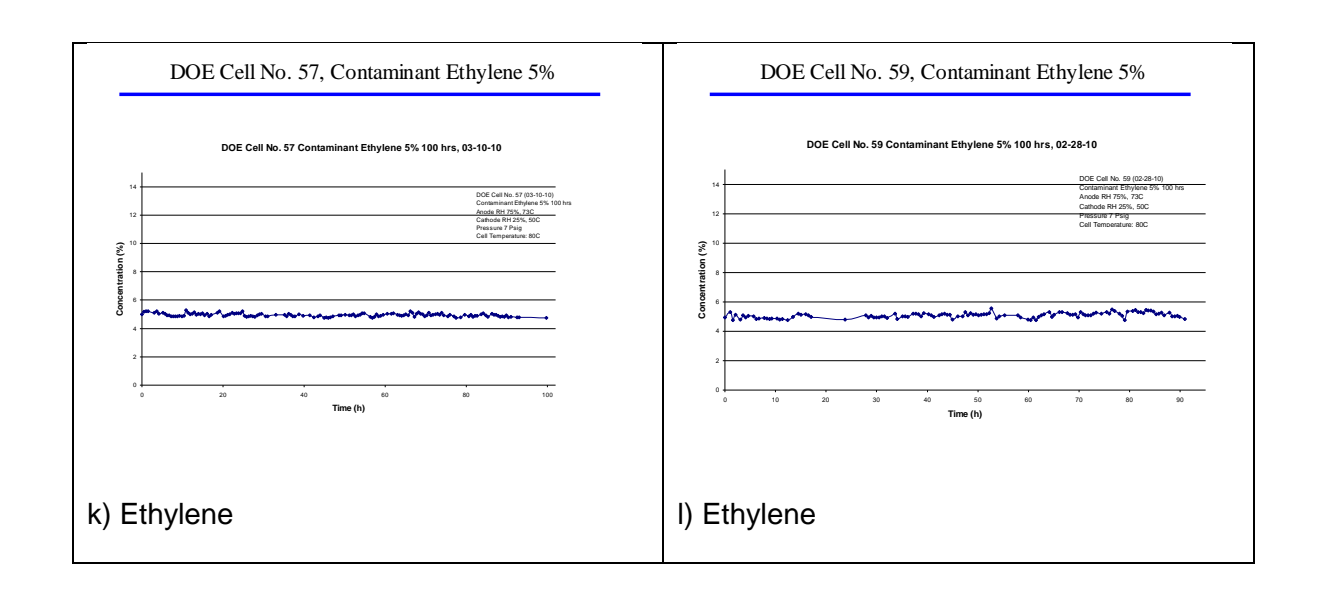
Control Results Using Gas Chromatography - This section presents the control results for analyses conducted by gas chromatography for the different contaminants introduced to the anode of the fuel cell during normal operating conditions, following previously established protocols. Also, it presents a new approach for the determination of the formic acid pathways during decomposition, using nuclear magnetic resonant (NMR), mass spectrometry, and related spectroscopic techniques.

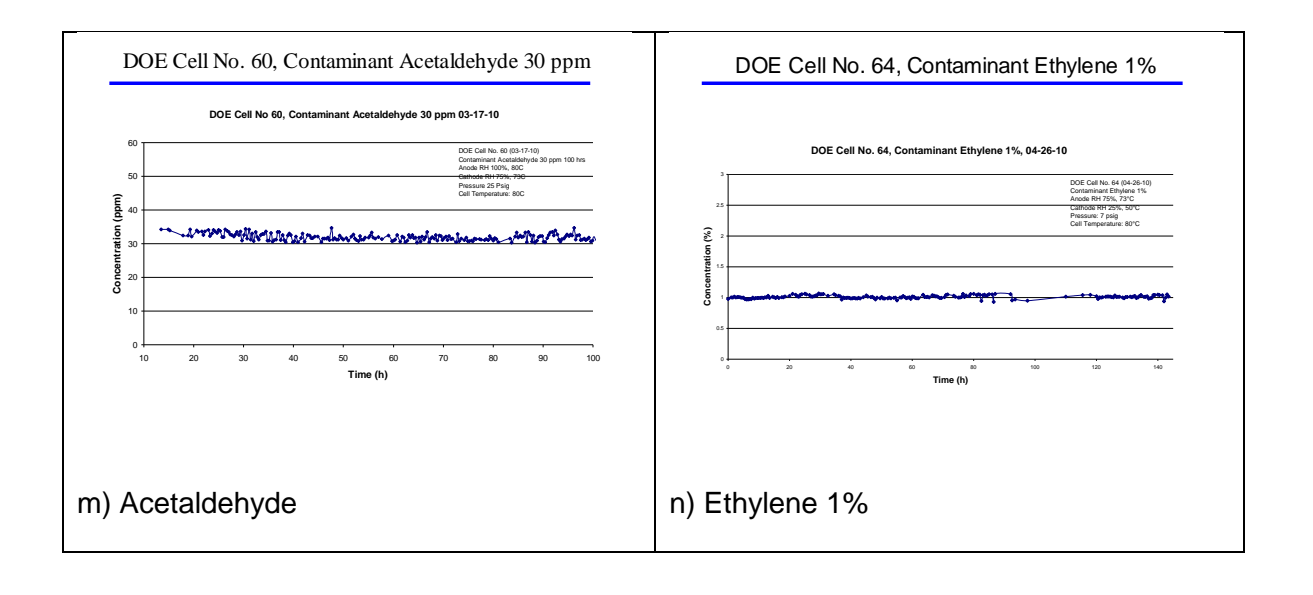
A gas chromatograph was first calibrated for the corresponding contaminant and the sampling was performed on-line in a continuous mode with sampling injection frequencies of about three to four times per hour during the period of the contamination test (100 hrs). In some cases, longer contamination tests were performed with components that did not produce significance degradation in cell performance. Additionally, increase in the level of contamination was performed to obtain an observable degradation in the performance of the fuel cell. The data provided for the gas chromatography analysis of different contaminants are presented in Figure 17.











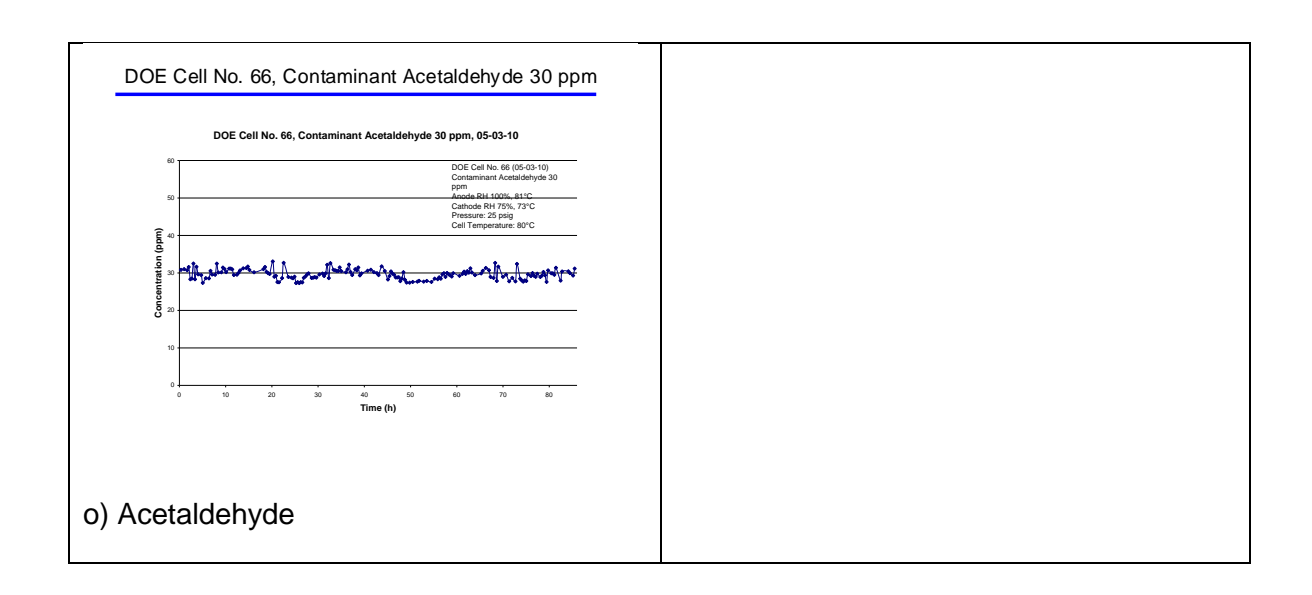


Figure 17 - Gas Chromatography Control Results for Formic Acid, Formaldehyde, Methyl Chloride, Ethylene and Acetaldehyde During Contamination Experiments at Different Concentration Levels and With Different Operating Conditions.

A portion of the research is focused in the contamination pathway for formic acid. A modified setup (Figure 17) was used to monitor in-situ the possible by-products for the decomposition of formic acid in anode and cathode side. Samples for the condensate in anode and cathode side was frequently monitored using NMR.

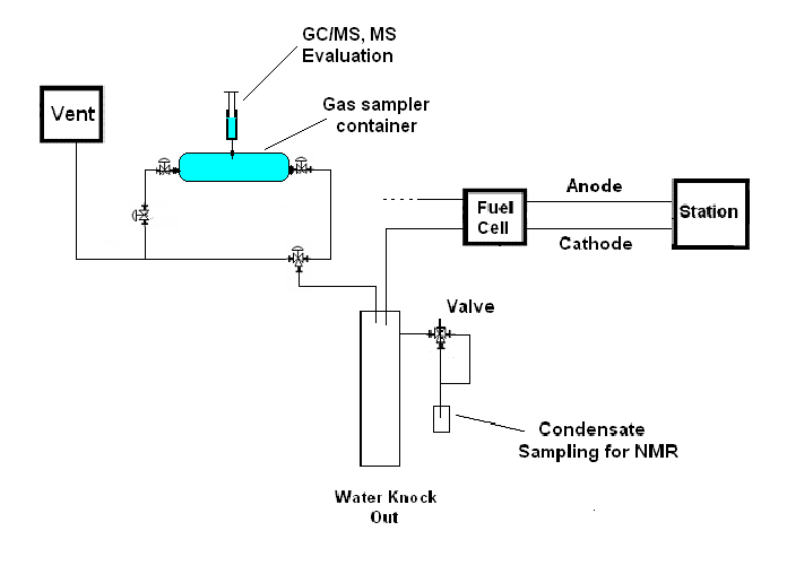


Figure 18 Schematic Setup for HCOOH, CO, and CO₂ Evaluation (Cathode and/or Anode Side)

Additional methods were developed to characterize mixtures with hydrogen and ethylene, formic acid, acetaldehyde, and formaldehyde. In this regard, a set up was designed and built to perform a real time analysis of the outlet gas streams of the anode and cathode side using a mass spectrometer. The preliminary analysis of the data provided by the real time analysis is reported in the Figures 19, 20 and 21.

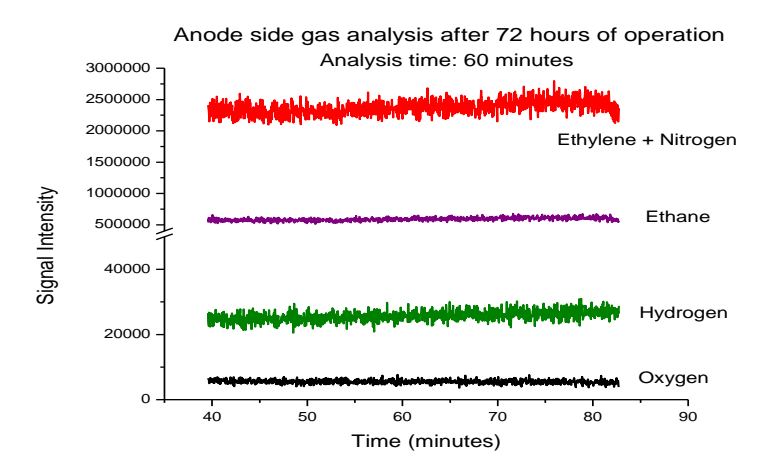


Figure 19 Outlet Gas Stream Analysis For The Anode Side. The Analysis Was Performed After 72 Hours Of Operation Of The Fuel Cell

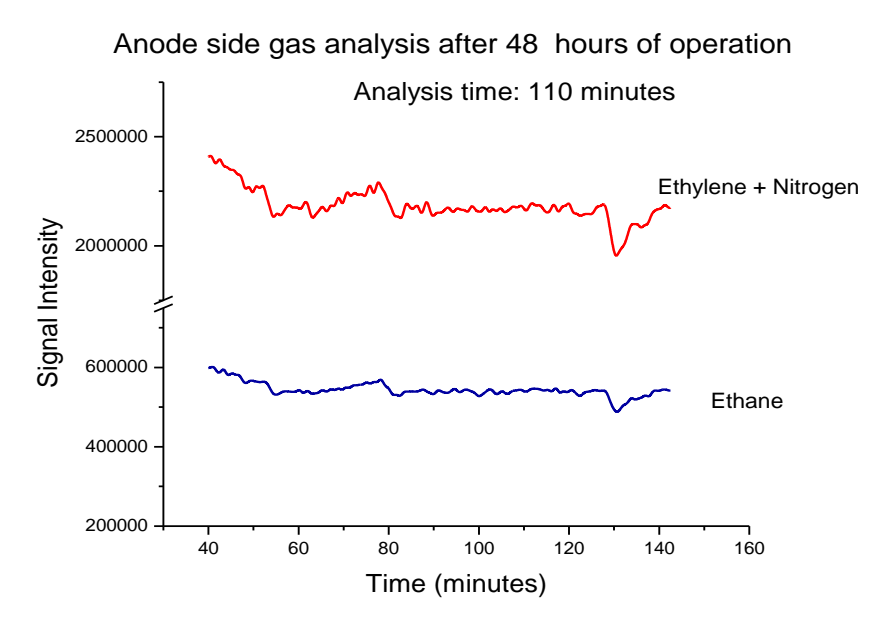


Figure 20 Outlet Gas Stream Analysis For The Anode Side. The Analysis Was Performed After 48 Hours Of Operation Of The Fuel Cell

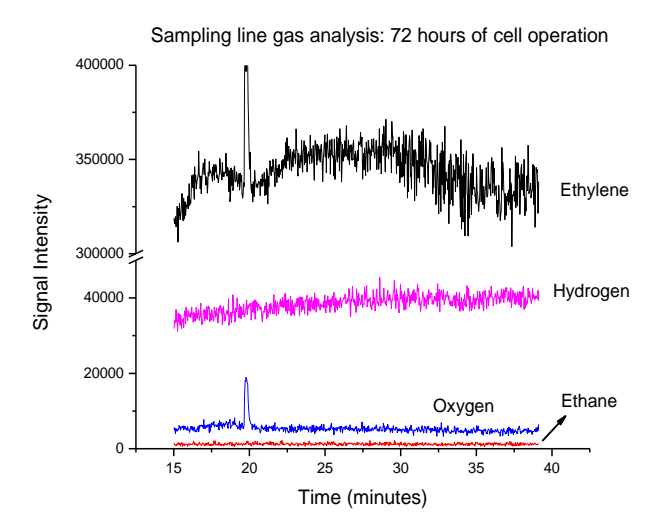


Figure 21 Sampling Line (Delivering Of The Mixture Hydrogen + Contaminant To The GC Analysis)

Task 3.0 Contaminant Studies

Organic Impurity Testing

Test and Hardware Definition

Extensive testing of organic impurities was conducted as part of this effort and to support fuel quality standard development. Hardware and test parameters are defined below in Table VI.

Parameter	Early	Intermediate	Latest
Membrane	Nafion 212	Nafion 212	PRIMEA
Loading (mg/cm ²) (A/C)	0.4 / 0.2	0.4 / 0.4	0.1 / 0.4
MEA OEM	Ion Power	Ion Power	Gore
GDL	SGL 10 BB	SGL 10 BB	SGL 25 BC
Active Area (cm ²)	25	25	25

Table VII defines the test conditions utilized in our program to evaluate the impurities of interest. Much of the work was conducted at a current density of 800 mA/cm² based on

this being a current density that effectively stresses the cell in a similar manner to that anticipated in an automotive application.

Table VII Definition of Major Test Parameters

Parameter	Early	Intermediate	Latest
Temperature (°C) (A/Cell/C)	80 / 80 / 80	80 / 80 / 73	80 / 73 / 49
Humidity (%) (A/C)	100 / 100	100 / 75	75 / 25
Stoich. (A/C)	1.3 / 2.0	2.0 / 2.0	1.2 / 2.0
Flow Rate (A/C)	Commensurate with current density		
Pressure (psig) (A/C)	25 / 25	25 / 25	7/7

Initial testing of oganic impurities began using methane as a fuel stream contaminant. Testing was set up as a series of 100-hour test runs using up to 5% methane in the fuel stream. MEA's for the cell were supplied by Ion Power and the test cell was supplied by Fuel Cell Technologies.

Testing was conducted at 200, 600 and 800 mA/cm² with standard test conditions. Using these conditions, we had difficulty in obtaining stable, long-term performance using the operating conditions "assigned" to our team by the Fuel Quality Working Group. Operation at 100% RH in our test systems has resulted in significant difficulty with the creation of flooding conditions within the cell. This has led to both inconsistent performance and premature failure by pinholing. We have found that by modifying the operating conditions to a lower RH, we have achieved more stable, long-term performance. These conditions are reflected in Table VII. Testing was conducted at 200, 600 and 800 mA/cm².

Results of specific impurity tests are noted in the sections below:

<u>Methane</u>

Figure 21 shows the results of fuel cell testing using 100 ppm methane at a current density of 200 mA/cm². Cell operating conditions were consistent with those identified in Table VI. Tests were conducted at 200, 600, and 800 mA/cm² with no evidence of effects of methane on cell performance. Some differences in overall cell performance were noted, however, with tests using 100 ppm methane showing slightly better

performance than tests using pure hydrogen. This has been shown to be due to a slight discrepancy in cell operating temperature between the two tests. Raw 600 mA/cm² data collected with better temperature control are shown in Figure 22, showing good agreement between cells operated with methane contamination and cells operated on pure hydrogen. Tests were repeated with a concentration of 5% methane. These tests demonstrated excellent agreement between data collected with pure hydrogen versus 95% hydrogen/5% methane, and 95% hydrogen/5% nitrogen for all current densities studied (Figure 23).

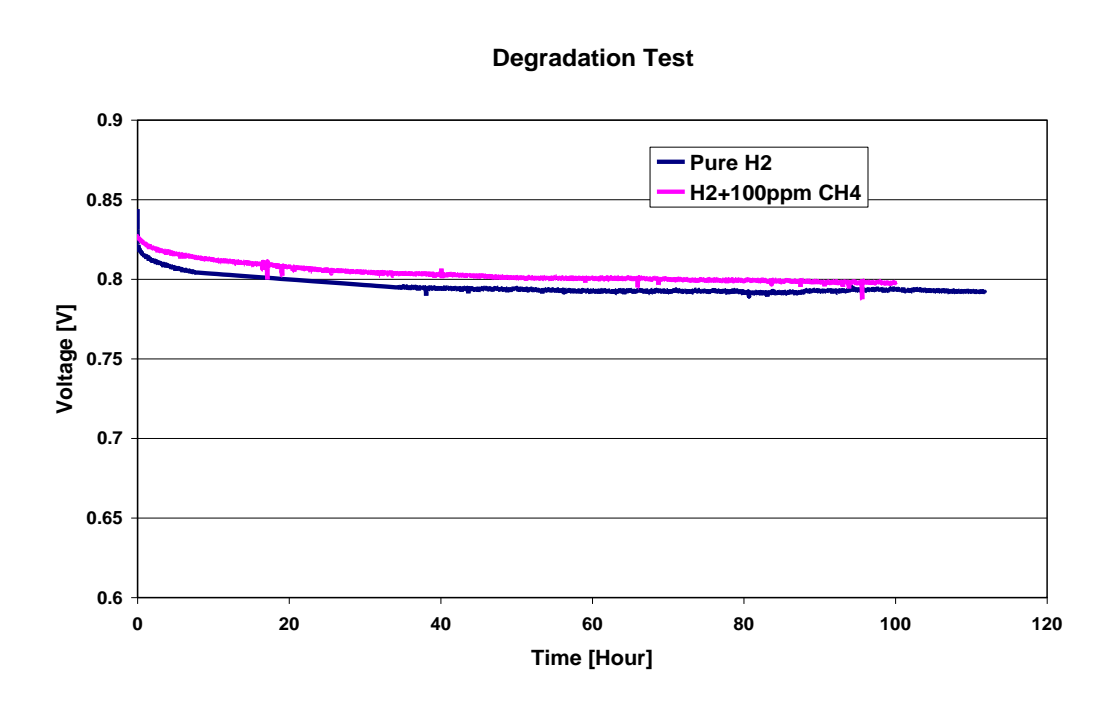


Figure 21 Test Results Using 100 ppm Methane at 200 mA/cm²





Durability Test (100 hours with/without CH4)

Anode / Cathode Pressure: 25 psig / 25 psig Control Current @ 600 mA/cm² Cell Temp: 80 °C Humudifier: 80 °C Anode / Cathode Flow Rate: 175 sccm / 642 sccm

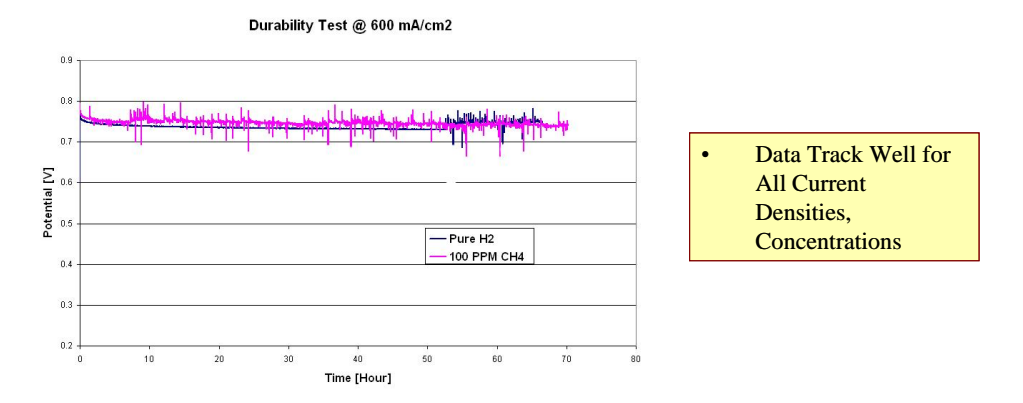


Figure 22 Test Results Using 100 ppm Methane at 600 mA/cm²

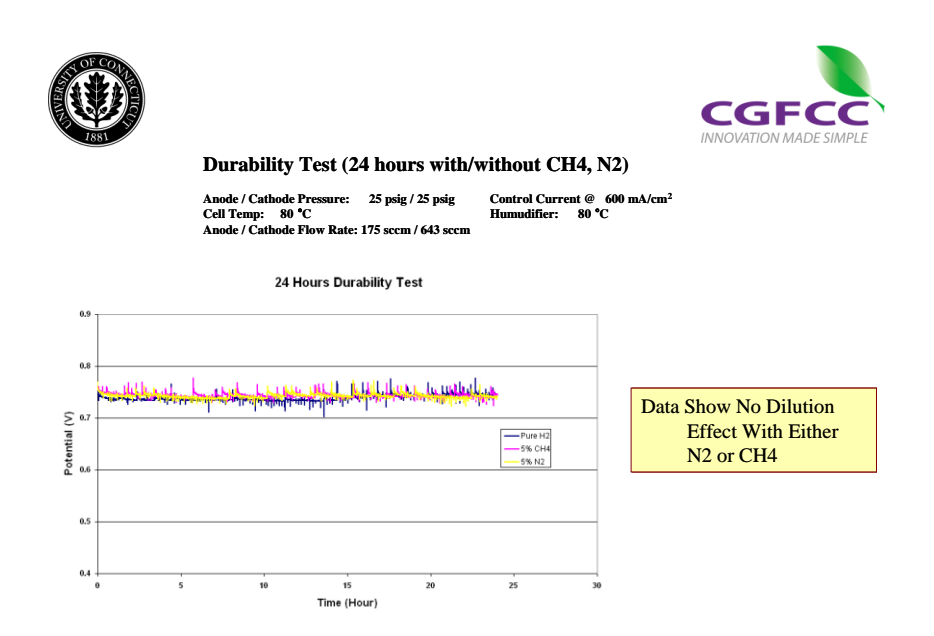


Figure 23 Test Results Using 5% Methane at 600 mA/cm² Showing No Effect of Either Methane or Nitrogen Contamination

Ethane

Tests were extended to evaluating the effects of ethane contamination on cell performance. Data collected in this program are shown in Figure 24.





Durability Test (100 hours with/without C2H6)

Anode / Cathode Pressure: 25 psig / 25 psig Cell Temp: 80 °C Anode / Cathode Flow Rate: 172 sccm / 643 sccm Control Current @ 600 mA/cm² Humudifier: 81 °C / 80 °C Mixing Flow Rate: 9 sccm

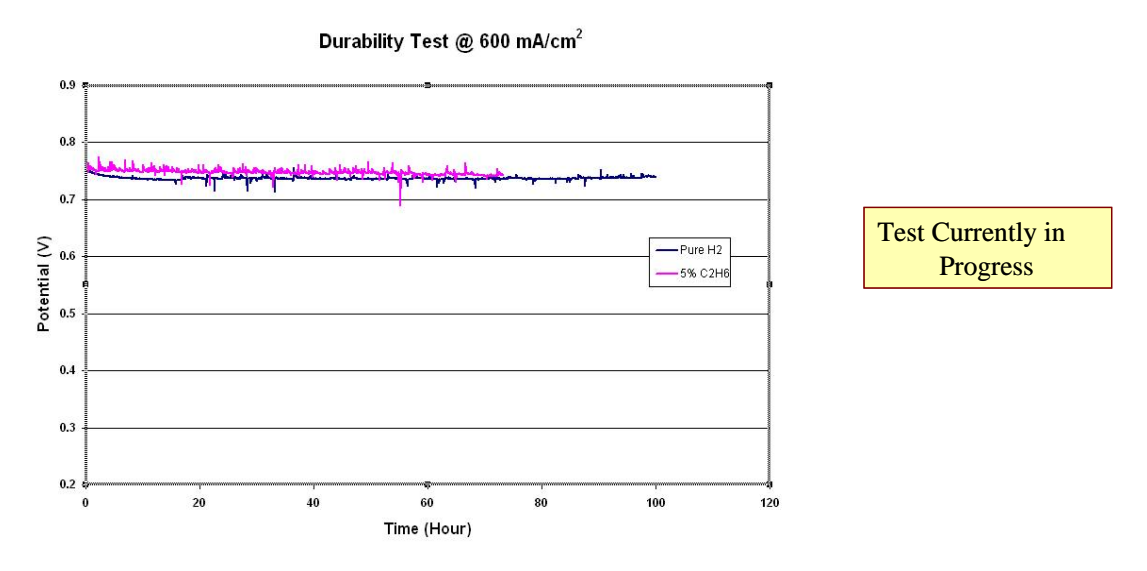


Figure 24 Test Results Using 5% Ethane at 600 mA/cm²

Formic Acid

The effect of formic acid (HCOOH) on fuel cell performance was investigated at two impurity concentrations, 100 ppm and 50 ppm. Testing showed some significant degradation of the cell performance during the 100 hour durability test period. Test results are as follows:

Cell operating conditions

Concentration	Current	RH (A/C)	Cell Temp	Flow	Stoich
ppm	Density		°C	Rates	(A/C)
	(mA/cm ²)			(A/C	
				sccm)	
50	800	100/75	80	181/664	2.0/2.0
100	800	100/75	80	181/664	2.0/2.0

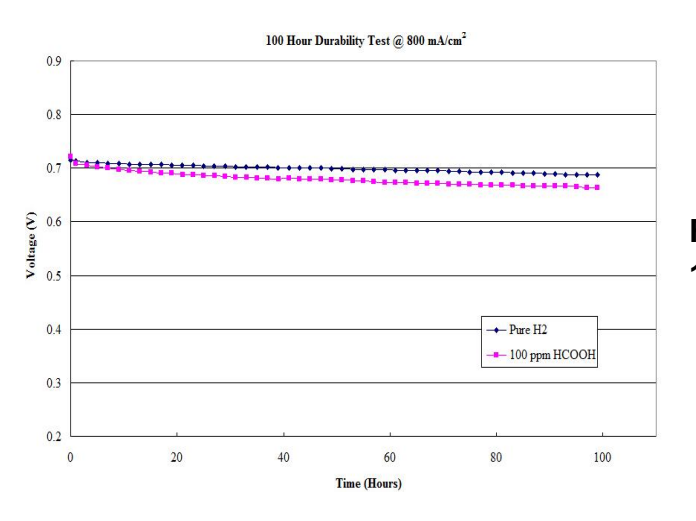


Figure 16 Durability Test Results Using 100 ppm Formic Acid

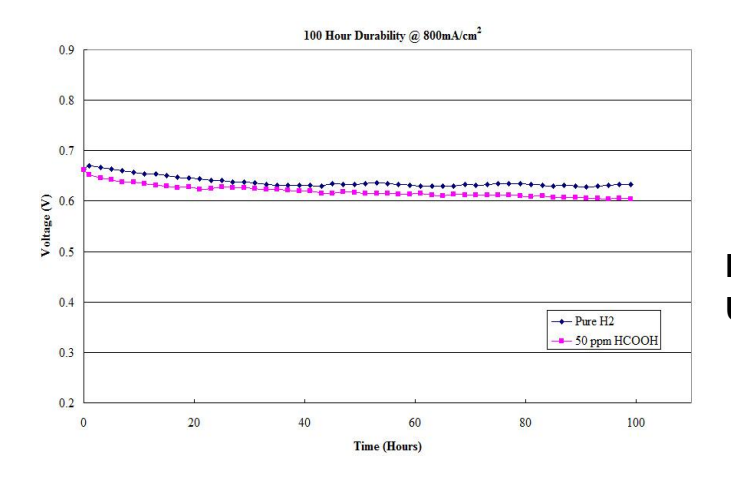
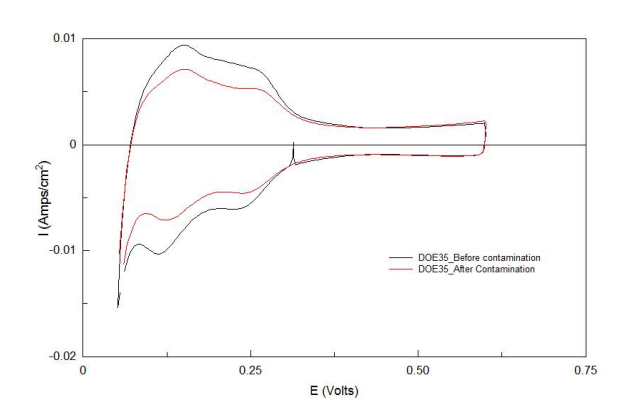


Figure 17 Durability Test Results Using 50 ppm Formic Acid

Cyclic voltammetry scans performed before and after contamination test show that ECA of the cathode decreased, signifying that HCOOH has a negative effect on the cathode catalyst layer.

Scan Range	Scan Rate	Cycles	Flow Rates (A/C)	Temperature	Pressure
0.05-0.6 V	20 mV/sec	4	250/250 sccm	Room	Ambient

Cyclic voltammetry scans were performed periodically (every 20 hours) during



contamination and recovery period to provide more details of the contamination on the cathode. During the CV scans, the cell temperature, the dew points, and the pressures remained unchanged. Pure nitrogen was fed to the cathode at 250 sccm, while HCOOH/H₂ was fed to the anode at 250 sccm.

Figure 18 CV Scans Before and After Contamination

Scan Range	Scan Rate	Cycles	Flow (A/C)	Rates	Cell Temp	Dew Points(A/C)	Pressure
0.05-0.6 V	20 mV/sec	4	250/250	sccm	80 °C	80/73 °C	25/25 psig

CVs were performed every 20 hours to characterize any poisoning of the cathode. The last cycle of each scan is shown above. The CV scans indicate a decrease in H₂ absorption peaks and an oxidation peak at 0.6 V which could be caused by the presence of absorbents on Pt surface.

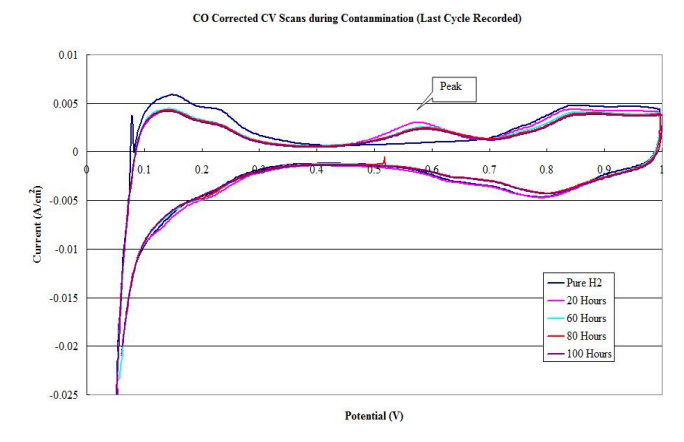
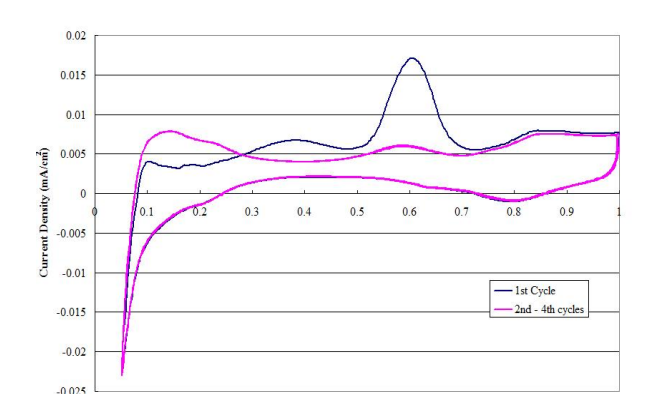


Figure 19 Progressive CV Scans on the Cell



The absorbents are oxidized around 0.4 V & 0.6 V (e.g. CO) in the 1st cycle. In the next

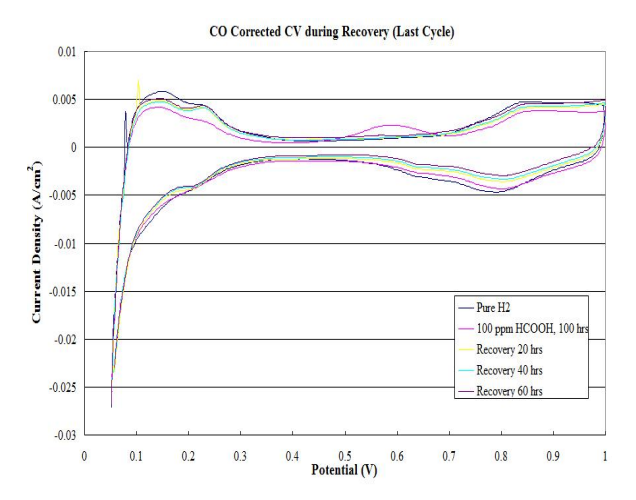


Figure 20 CV Scans Showing Changes in H₂ Absorption Peaks and Oxidation of Absorbents

An example of individual CV scan is shown above. Each scan consists of 4 cycles. In the 1st CV cycle, the hydrogen absorption peak nearly disappeared. The Pt surface seems to be covered by absorbents (peaks at 0.4V and 0.6 V).

3 cycles recovery of H_2 absorption peak is observed, but evidence of surface coverage still exists.

Figure 21 CV Scans Showing Recovery

After recovery with pure H_2 for 20 hours, hydrogen absorption peaks are partially recovered. Further running (up to 100 hrs) with pure H_2 does not result in further recovery. This suggests that formic acid can crossover the membrane

and contaminate the cathode. The contamination cannot be fully recovered just by purging pure H_2 through the anode.

<u>Acetaldehyde</u>

Testing was completed using 30 ppm acetaldehyde showing no significant impact on fuel cell performance during an 800 mA/cm² test (Figure 22). Both curves show the same degradation rate (slope) with the exception of a slight discontinuity in the pure hydrogen curve at ~45 hours due to a facility power outage.





Durability Test (100 hours with/without CH3CHO)

Anode / Cathode Pressure: 25 psig / 25 psig Cell Temp: 80 ° C
Anode / Cathode Flow Rate: 178 sccm / 664 sccm

Control Current @ 800 mA/cm² Humidifier: 81 ° C / 73 ° C

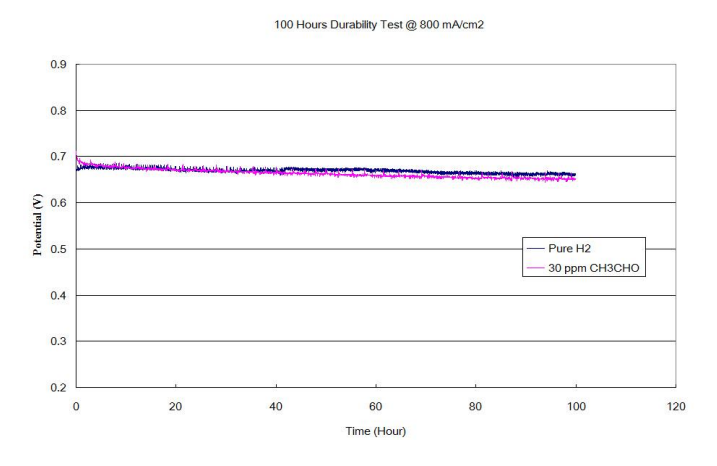






Figure 22 Effects of 30 ppm of Acetaldehyde on Fuel Cell Performance are Insignificant

Testing of the effect of acetaldehyde (CH₃CHO) on cell performance was also investigated at an impurity concentration of 100 ppm. No significant effect was found during these contamination tests. Test results are as follows:

Cell operating conditions

Concentration	Current	RH (A/C)	Cell Temp	Flow	Stoich
ppm	Density		°C	Rates	(A/C)
	(mA/cm ²)			(A/C	
				sccm)	
30	800	100/100	80	181/664	2.0/2.0
100	800	100/75	80	181/664	2.0/2.0

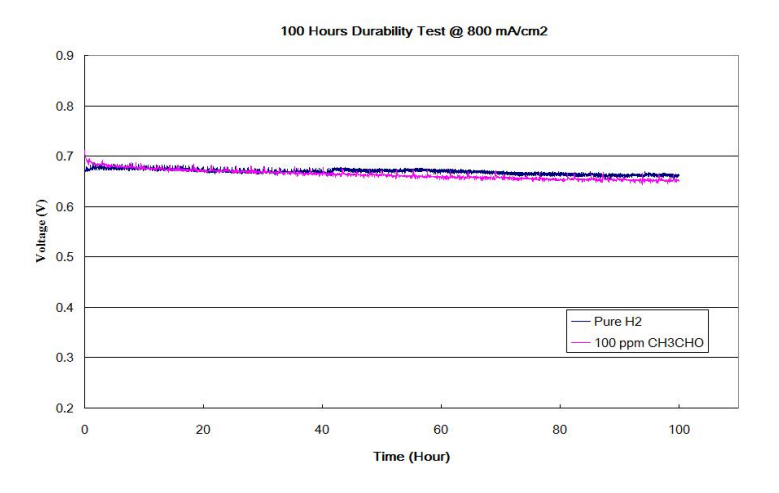


Figure 23 Durability Test With 100 PPM Acetaldehyde

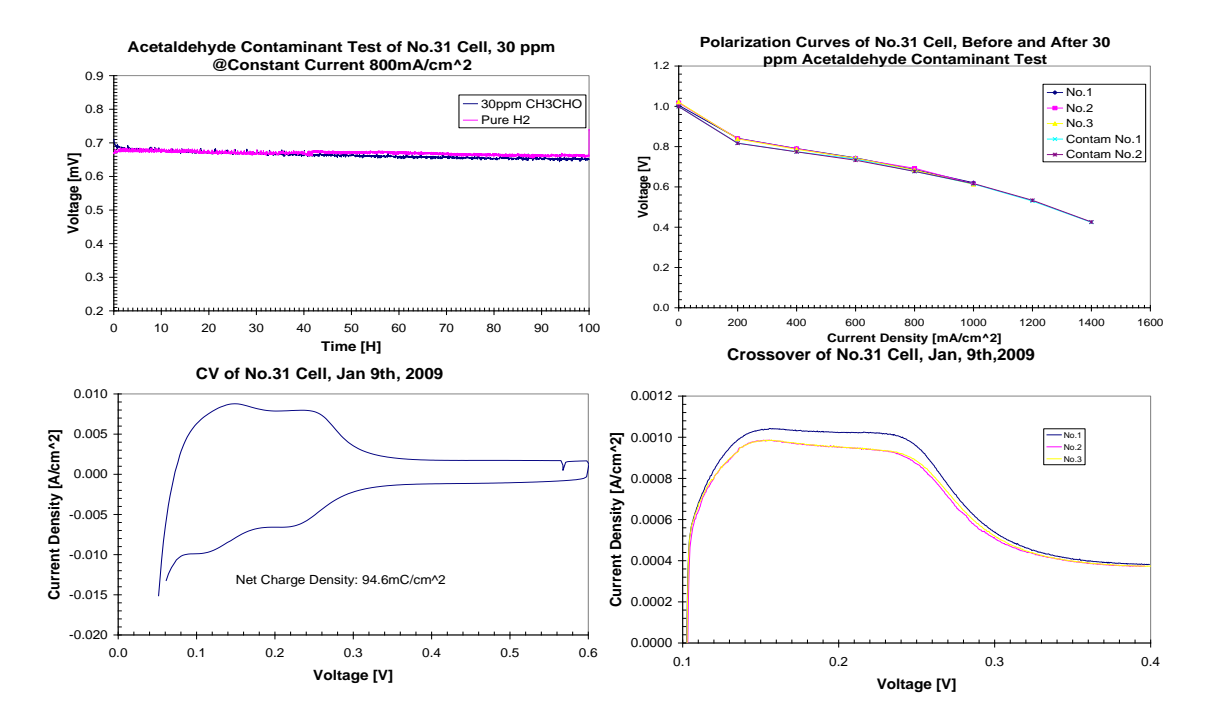


Figure 24 No.31 Cell Test Results for 30ppm Acetaldehyde

Ethylene

Tests using ethylene as an impurity showed some effect on cell performance as is evident in Figure 25.

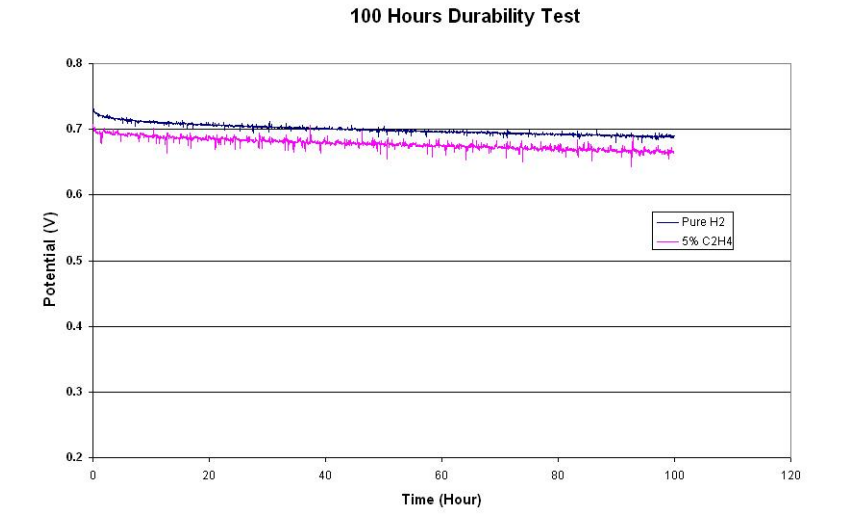
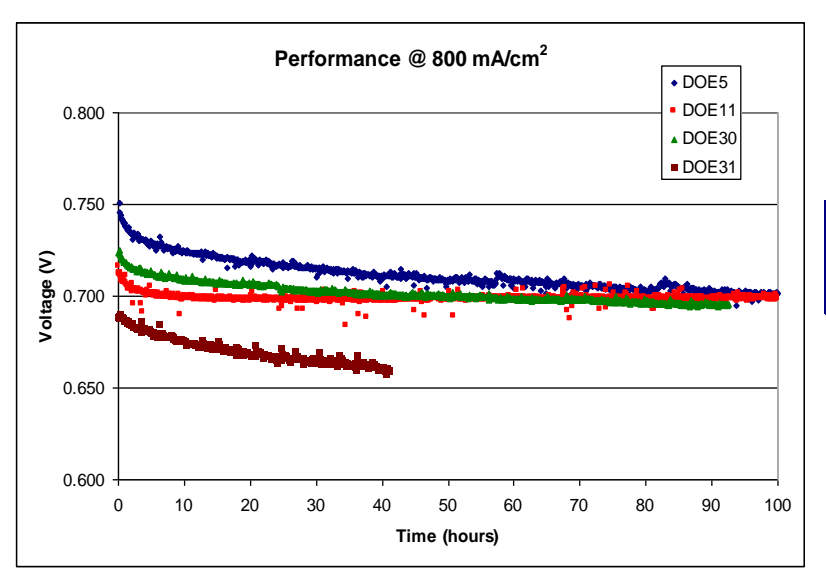


Figure 25 Test Results Using 5% Ethylene at 600 mA/cm²

MEA Quality Control and Performance Stability

While conducting this test program, we developed significant difficulty in obtaining stable performance using pure hydrogen as a fuel. As a result, we have recalibrated all of our test equipment, reviewed our test and cell assembly procedures and verified the materials that we had been using in our cell assemblies. Upon further investigation, we determined that there was significant variability between lots of MEA's obtained from our supplier. Some MEA lots performed well, and some showed significant inconsistency in performance from one MEA to the next. During the program we were in close communication with the manufacturer and have developed a test program in an effort to determine the source of this inconsistency. Figure 26 below shows the broad variability in voltage performance for different MEA lots.



Cell	Loading (A/C)			
	0.4/0.2			100%/100%
11	0.4/0.2	100	1.3/2.0	100%/100%
30	0.4/0.4	50	2.0/2.0	100%/75%
31	0.4/0.4	50	2.0/2.0	100%/75%

Figure 26 Variability of MEA Performance Under Standard Operating Conditions

In working with the manufacturer we found that certain lots of MEA's showed more consistent performance than others, though the manufacturer has not revealed what the differences are between the lots of material. The problem does, however, seem to have something to do with a specific lot of electrocatalyst material used in the manufacture of MEA's. It has been found through this testing that improved stability can be realized by extending the break-in period for the MEA. Figure 27 below further demonstrates the variability within these lots of material, and provides a sampling of the evaluation program.

Viability	Lot #	Cell#	Operator	Built by	Membr Type	GDL	Loading A/C	Gasket Thickness (mil)	Torque (in.lb)
Good	727	1	Xiaoyu	Xiaoyu	Nafion 212	SGL 10BB	0.4/0.2 mg/cm2	10	100
Good	727	2	Xiaovu	Xiaoyu	Nafion 212	SGL 10BB	0.4/0.2 mg/cm2	10	100
Good	727	4	Xiaoyu	Xiaoyu	Nafion 212	SGL 10BB	0.4/0.2 mg/cm2	10	100
Good	727	6	Xiaoyu	Xiaoyu	Nafion 212	SGL 10BB	0.4/0.2 mg/cm2	10	100
Only 2	894		Xiaoyu	Xiaoyu	Nafion 212	SGL 10BB	0.4/0.2 mg/cm2	10	100
are good	894	8	Xiaoyu	Xiaoyu	Nafion 212	SGL 10BB	0.4/0.2 mg/cm2	10	100
	894	9	Xiaoyu	Xiaoyu	Nafion 212	SGL 10BB	0.4/0.2 mg/cm2	10	100
	894	10	Xiaoyu	Xiaoyu	Nafion 212	SGL 10BB	0.4/0.2 mg/cm2	10	100
	894	11	Xiaoyu	Xiaoyu	Nafion 212	SGL 10BB	0.4/0.2 mg/cm2	10	100
	894	12	Xiaoyu	Xiaoyu	Nafion 212	SGL 10BB	0.4/0.2 mg/cm2	10	100
	894	13	Phil	Phil	Nafion 212	SGL 10BB	0.4/0.2 mg/cm2	10	50
	894	14	Xiaoyu	Xiaoyu	Nafion 212	SGL 10BB	0.4/0.2 mg/cm2	10	100
	894	15	Phil	Phil	Nafion 212	SGL 10BB	0.4/0.2 mg/cm2	10	50
Bad	1002	16	Xiaoyu	Xiaoyu	Nafion 212	SGL 10BB	0.4/0.2 mg/cm2	10	100
Bad	1002	17	Phil	Phil	Nafion 212	SGL 10BB	0.4/0.2 mg/cm2	10	50
Bad	1002	18	Xiaoyu	Xiaoyu	Nafion 212	SGL 10BB	0.4/0.2 mg/cm2	10	100
Bad	1038	19	Phil	Phil	Nafion 212	SGL 10BB	0.4/0.4 mg/cm2	10	50
Good	1004	20	Xiaoyu	Xiaoyu	Nafion 212	SGL 10BB	0.4/0.4 mg/cm2	10	50
Bad	1038	21	Xiaovu	Xiaovu	Nafion 212	SGL 10BB	0.4/0.4 mg/cm2	10	50
Bad	1038	22	Xiaofeng	Xiaofeng	Nafion 212	SGL 10BB	0.4/0.4 mg/cm2	10	50
Bad	1038	23	Xiaoyu	Xiaoyu	Nafion 212	SGL 10BB	0.4/0.4 mg/cm2	10	50
Bad	1038	24	Xiaoyu	Xiaoyu	Nafion 212	SGL 10BB	0.4/0.4 mg/cm2	10	50
Bad	1038	25	Xiaoyu	Phil	Nafion 212	SGL 10BB	0.4/0.4 mg/cm2	10	50
Bad	1038	26	Xiaofeng	Phil	Nafion 212	SGL 10BB	0.4/0.4 mg/cm2	10	50
Good	1080	27	Xiaofeng	Xiaofeng	Nafion 212	SGL 10BB	0.4/0.4 mg/cm2	12	50
Bad	1081	28	Xiaoyu	Xiaoyu	Nafion 212	SGL 10BB	0.4/0.4 mg/cm2	12	50
Good	1080	29	Phil	Phil	Nafion 212	SGL 10BB	0.4/0.4 mg/cm2	10	50
Good	1080	30	Xiaoyu	Phil	Nafion 212	SGL 10BB	0.4/0.4 mg/cm2	12	50
Good	1080	31	Xiaoyu	Phil	Nafion 212	SGL 10BB	0.4/0.4 mg/cm2	10	50
Good	1080	32	Xiaofeng	Phil	Nafion 212	SGL 10BB	0.4/0.4 mg/cm2	12	50
Good	1080	33	Xiaofeng	Phil	Nafion 212	SGL 10BB	0.4/0.4 mg/cm2	10	
Good	1080		Xiaofeng	Phil	Nafion 212	SGL 10BB	0.4/0.4 mg/cm2	10	50
Good	1080		Xiaofeng	Phil	Nafion 212	SGL 10BB	0.4/0.4 mg/cm2	10	50

Figure 27 Variability Within MEA Lot Number

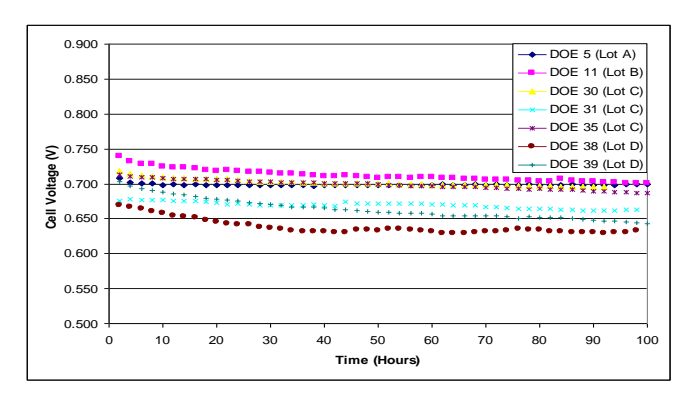
With stable operating conditions established, 11 cells were built to support continued impurity testing. Four of these cells DOE 31, 33, 34, and 35 were from the same batch as cells DOE 29 and DOE 30. DOE 31 and 35 were found to have stable performance and were used for acetaldehyde and formic acid testing respectively. On disassembly

DOE 31 was found to have a crystalline particulate on the anode GDL, as seen in Figure 28, and spotting on the cathode and anode flow fields. The crystalline substance on the GDL was not observable when using microscopy but appeared to be a polymeric substance formed during operation of the cell using a formic acid impurity – believed to be paraformaldehyde.



Figure 28 Crystalline Particles Found on Anode GDL on Cell Disassembly

DOE 35 on disassembly showed no abnormalities associated with the formic acid testing and showed no significant increase in crossover over cell life. The other two cells were not used for testing due to irregular performance in one case and development of significant crossover in another. DOE 36 and 37 were built from a new batch of CCM's in the case of DOE 36 no stable performance could be achieved during conditioning and DOE 37 developed a significant amount of crossover during the 100 hour durability testing. DOE 38, 39, 40, 41, and 42 were all built from the same CCM lot. DOE 38 was used for 50 ppm formic acid testing and DOE 39 for additional 100 ppm formic acid testing. These cells showed stable but reduced performance when compared to DOE35. Additionally the ECA of this lot of CCM's tend to be a factor of two lower than lot used for DOE 35. On disassembly these cells showed no



abnormalities, but had developed an increased amount of crossover over the 300 hours of testing. DOE 40, 41, and 42 are currently being conditioned for future contaminant testing. A summary of cell performance compared by CCM lots can be seen in Figure 39.

Figure 29 Summary of Cell Performance Compared by CCM Lots

Based on the significant lot sensitivity observed during testing, and working with input from the other test laboratories and members of the Hydrogen Fuel Quality Working Group, we baselined the utilization of Gore CCM's having significant commercial relevance.

Cationic Impurity Testing

Fully hydrated Nafion membrane samples were doped with concentrations of various metal cations, including Li, Na, K, Cs, Ca, Mg, Ni, Fe, Al, Cu, and Cr in an effort to study the effects of contaminant mass and valence on critical membrane properties. Studies focused on a balance between constituents that would normally be present in the materials of construction of the fuel cell, those that might be ingested in the fuel cell from either hydrogen or air, and those that would provide important information for contaminant modeling activities. To date, the effects of these cations on properties including gas/water transport, water content, and mechanical properties have been evaluated.

Several critical findings and relationships were gleaned from this work. Laboratory tests demonstrated that cations rapidly transport into the membrane and disperse readily throughout the membrane structure achieving high equilibrium concentrations. Studies showed that ion charge density governs membrane water content with small ions having a large water shell demonstrating the highest water content and larger ions having a small water shell demonstrating the lowest water content.

Gas and hydrodynamic permeability studies showed transport in accordance with a linear relationship in the following rank order: $H_2>O_2>N_2>H_2O$. Hydrogen permeability data are shown in Figure 30. Data showed that cation contaminants negatively affect gas and water transport, with charge density appearing to be a factor in transport rate determination. Unique diffusion coefficients were calculated for each contaminating species suggesting that the contaminant is an integral participant in the transport process.

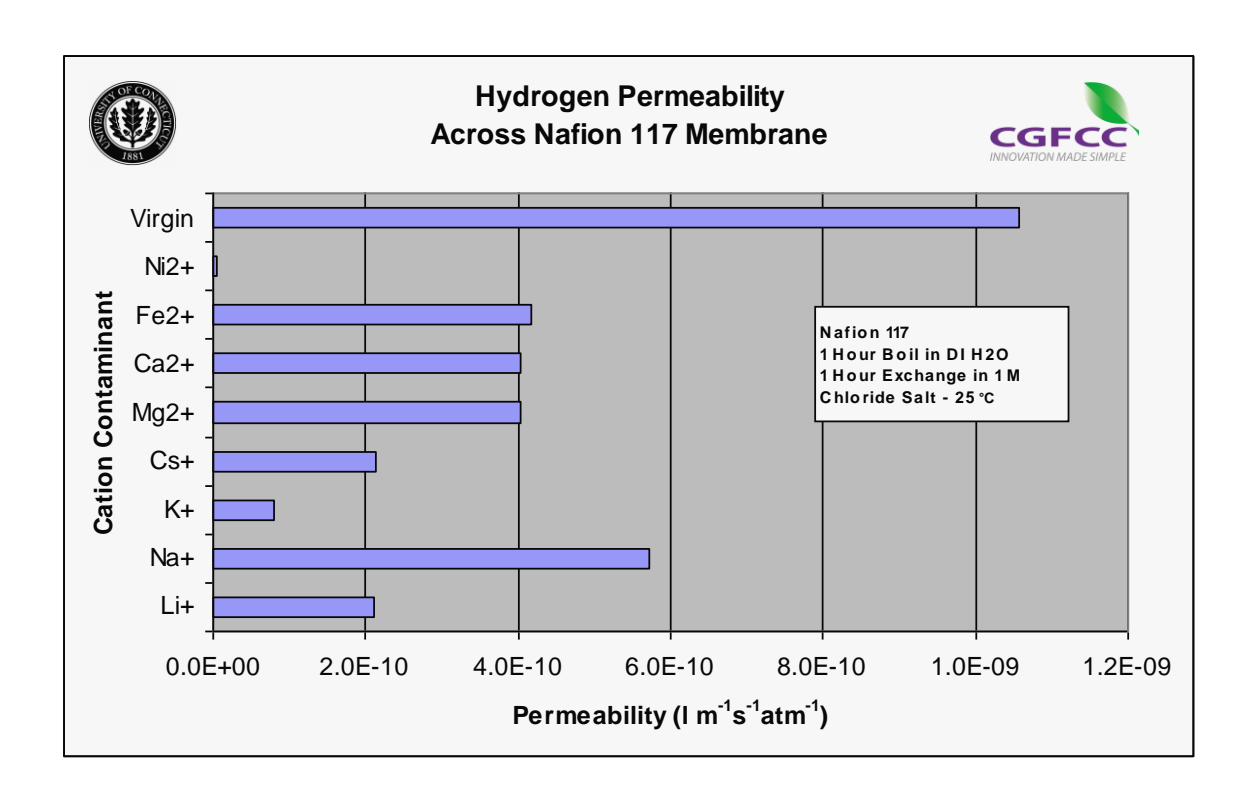


Figure 30 Effect of Ionic Contamination on Permeability of Hydrogen Across Nafion 117 Membrane

AC resistance measurements showed that size of the ion charge carrier itself and not the hydrated ion is an important factor in the conduction mechanism. Studies showed that membrane area specific resistance correlates well with water content (Figure 31).

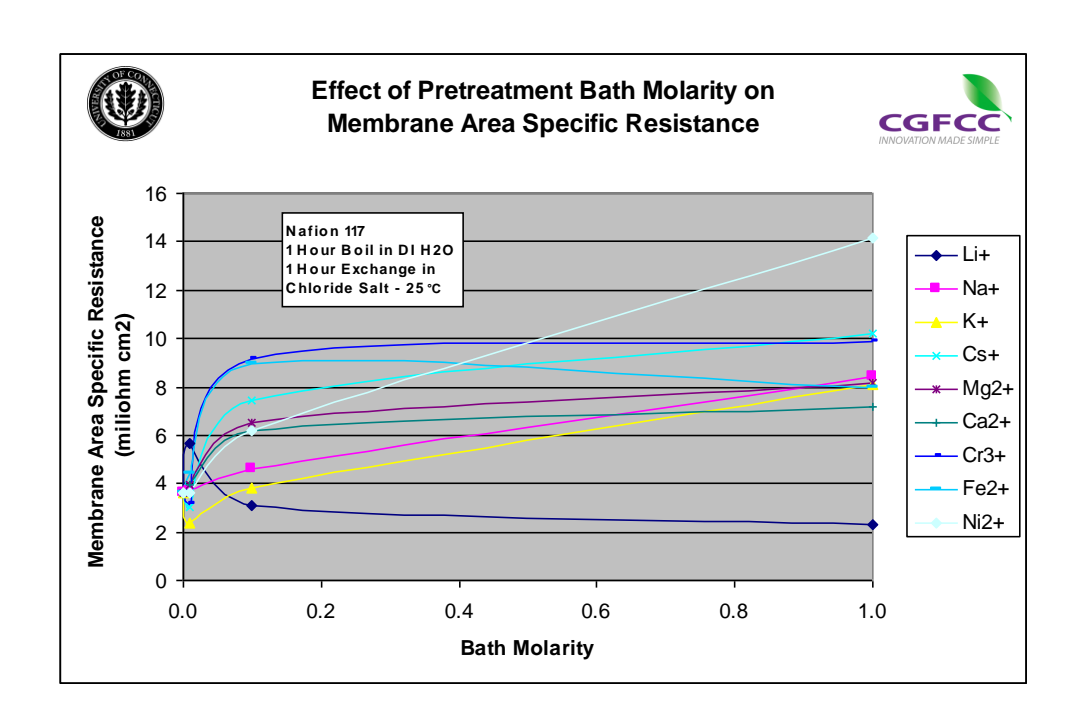


Figure 31 Effect of Contaminant Type and Molarity on Membrane Area Specific Resistance

Figure 32 shows the preliminary results of tests conducted using acetaldehyde as a contaminating species. Note, that in this test, the cell was challenged with acetaldehyde at a level of only 30 ppm. This choice is driven by the low vapor pressure of this constituent, which would also limit the opportunity for higher levels of contamination in practice.

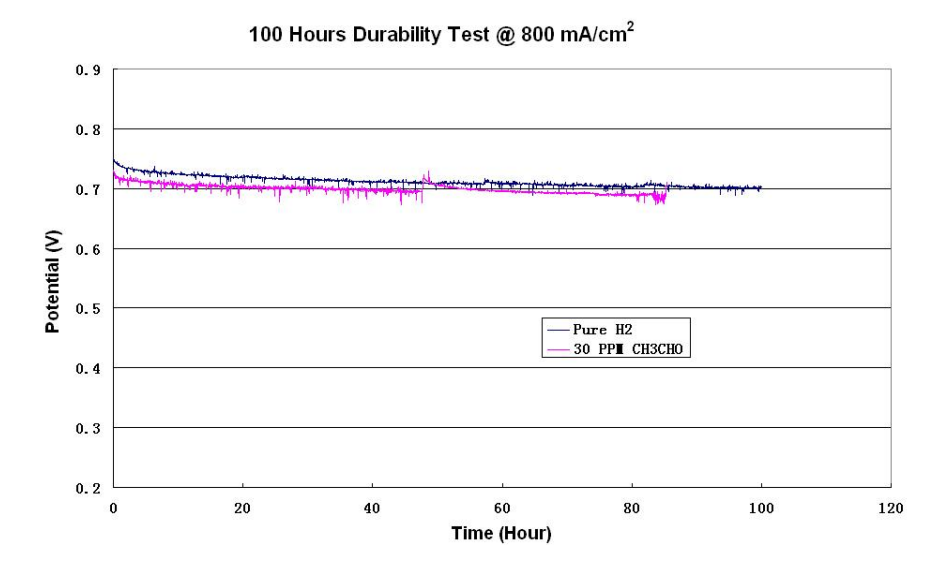


Figure 32 Test Results Using 30 PPM Acetaldehyde at 800 mA/cm²

Regarding the mechanical property tests, increases in membrane yield strength (Figure 33) and the modulus of elasticity were demonstrated with contamination. Studies showed that cation size plays an important role in determining the magnitude of this increase, indicating that larger ions interfere more with strain (elastic and plastic) than smaller ones. Cation contaminants were found to reduce strain to break (Figure 5) with smaller ions having the largest water shell showing the greatest effect. Ultimate tensile strength was found to increase slightly with all contaminants with the exception of lithium, which effected a reduction in this key property, again reflecting a relationship with contaminant size.

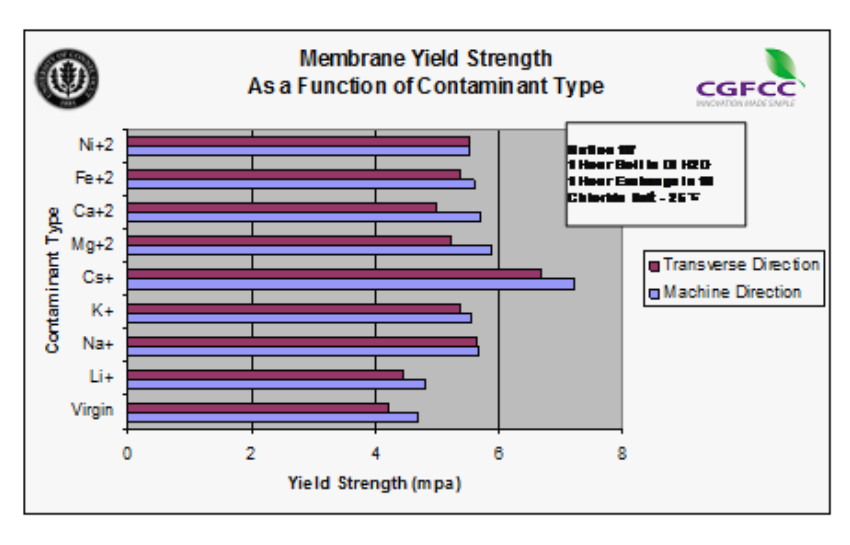


Figure 33 Influence of Contaminant Type on Membrane Yield Strength

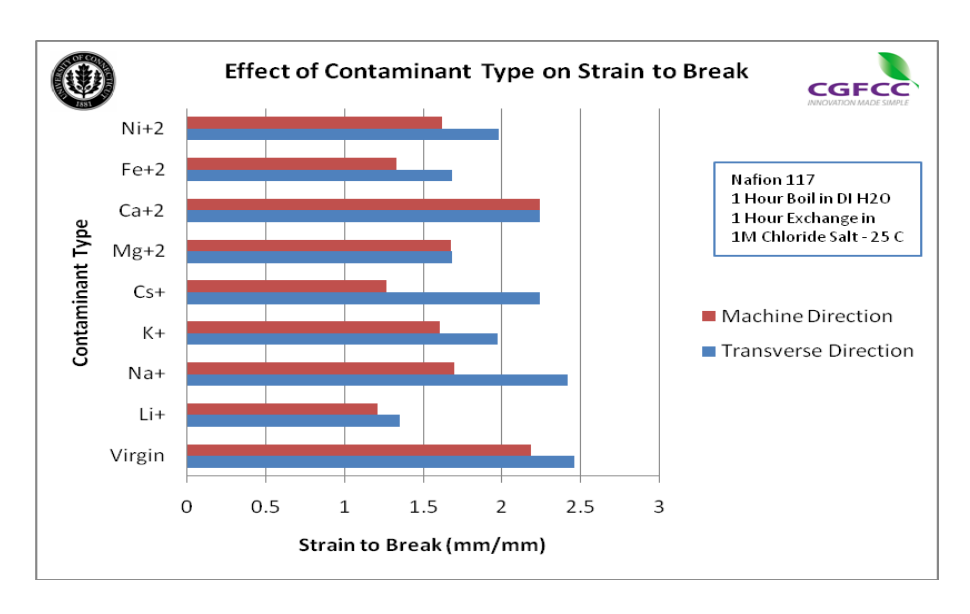


Figure 34 Influence of Contaminant Type on Membrane Strain to Break

In our studies, the AC resistance method was chosen to determine the ionic resistance of Nafion samples based on its ease of use and the ability to achieve repeatable, reliable results. This method further provides a more rapid way to evaluate membrane resistance than the other techniques.

In this test a Nafion membrane sample was clamped between two platinum coated titanium platens in a Carver "C" hydraulic press. The platens of the press were rectangular and measured 3.81 cm x 5.08 cm having a footprint of 19.35 cm². Membranes were clamped between the platens of this press and consistently loaded to 3 metric tons. Four electrical leads were attached to the press fixture with a current and voltage lead attached to each platen. The other end of each lead was attached to a Hewlett Packard model 4338 A milliohm meter. This instrument applies a fixed, 1 kHz high frequency sine wave to the membrane as translated through the platens of the press. A schematic of this apparatus is shown in Figure 35.

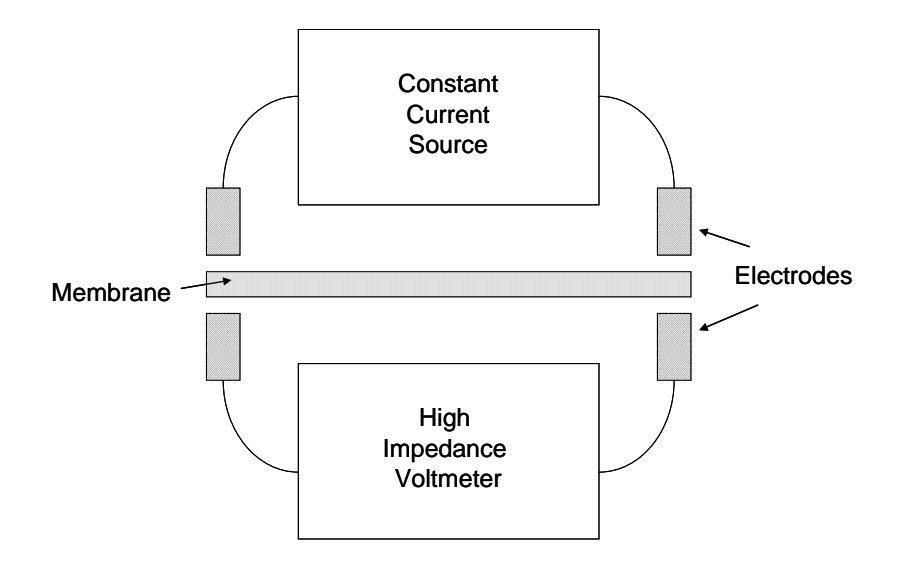


Figure 35 Ionic Resistance Test Schematic

Membrane samples were held in water until they were measured. Each membrane sample was handled with clean nitrile rubber gloves, placed between the platens, and the platens were compressed by pumping the manual hydraulic lever. A photograph of this apparatus is shown in Figure 36.



Figure 36 Membrane Resistance Test Apparatus

The resistance in milliohms was measured for each of the membrane samples of interest. Using these results, a quantity known as Area Specific Resistance (ASR) was calculated. ASR is a material quantity in that it depends on the dimensions of a sample and is often expressed in units of $m\Omega^*cm^2$. Figure 37 below shows the ASR calculated for each of the membrane samples as a function of the concentration of the treatment bath that these samples were exposed to.

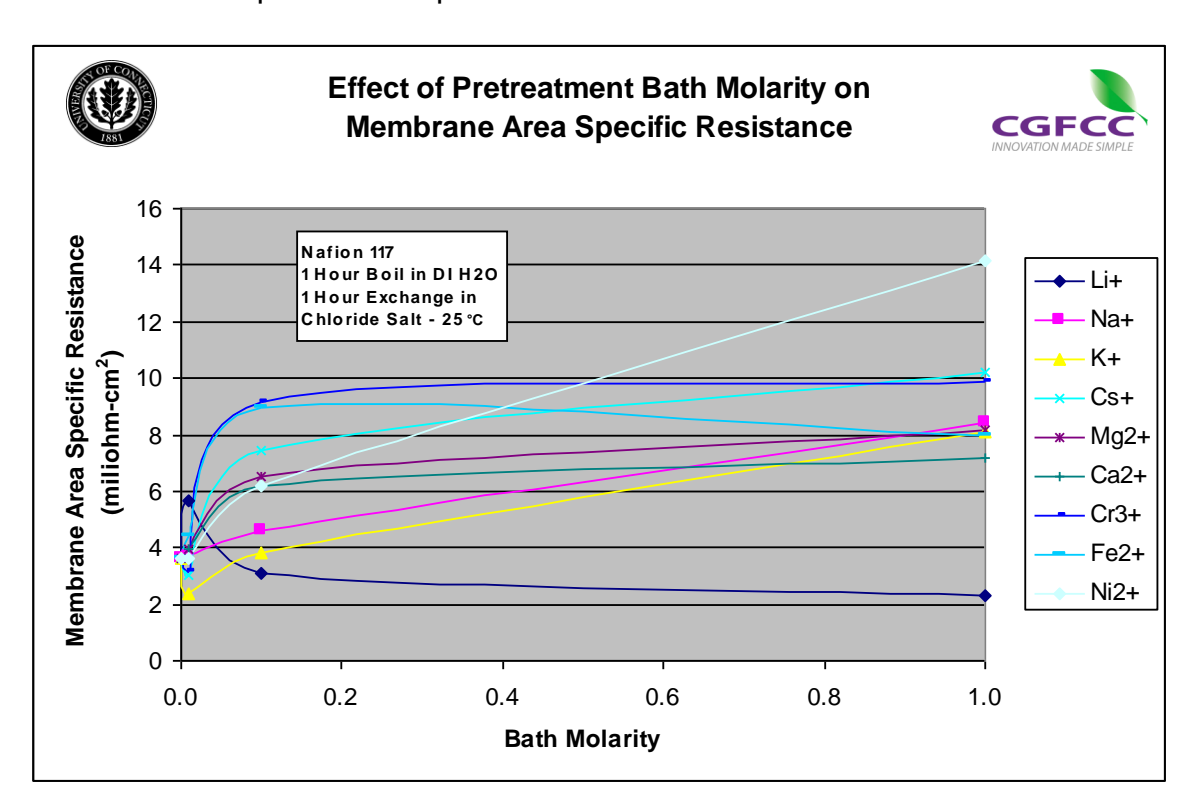


Figure 37 Effect of Cation Type and Molarity on Membrane Area Specific Resistance

The Area Specific Resistance can also be related to the conductivity σ as follows:

$$R \cdot A = L / \sigma$$

Where R is the measured resistance (m Ω), A is the area used in the resistance measurement (cm 2), L is the thickness of the membrane sample (cm), and σ is the conductivity (mS/cm).

The area specific resistance was also plotted versus ion exchange capacity for the various contaminants of interest that had been exchanged into Nafion 117 in a 1 M chloride salt bath for a period of 1 hour. At very low ion exchange capacities, the area specific resistance rises significantly, however, a more gradual dependence is noted at

higher ion exchange capacities. Membranes having ferrous ions exchanged into them show a relatively high area specific resistance even at fairly high ion exchange capacities. This shows that ferrous ion tend to negatively affect area specific resistance more significantly than the other contaminants (Figure 38).

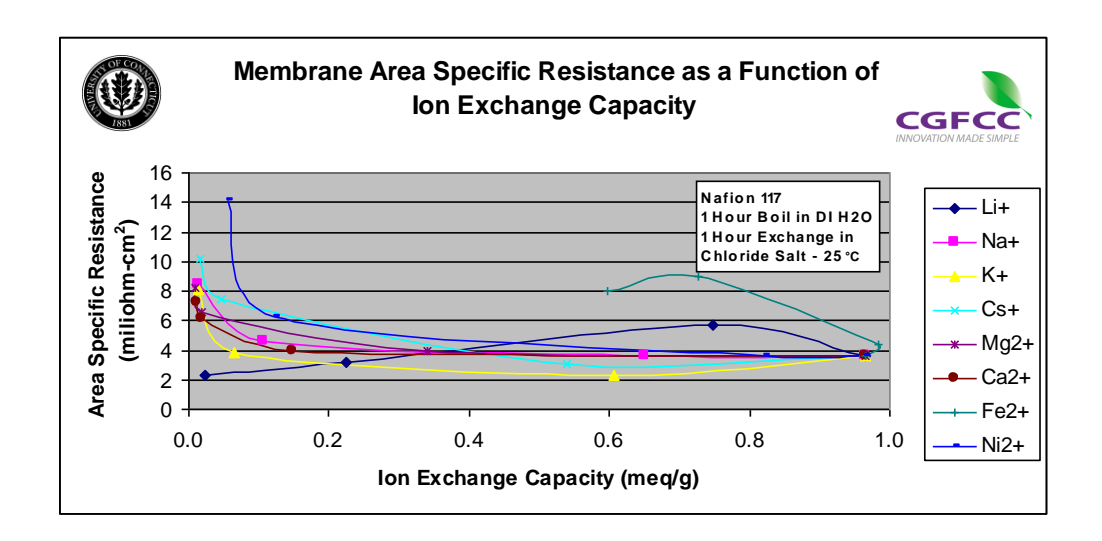


Figure 38 Membrane Area Specific Resistance as a Function of Ion Exchange Capacity and Ion Type

The area specific resistance of the membrane was also plotted versus membrane water content. Based on this plot (Figure 39) it appears that membrane area specific resistance is a strong function of membrane water content regardless of the ion exchanged into the membrane. Though each different contaminant shows a slightly separate relationship between area specific resistance and water content, the overall data, combined show a somewhat linear relationship, regardless of contaminating species.

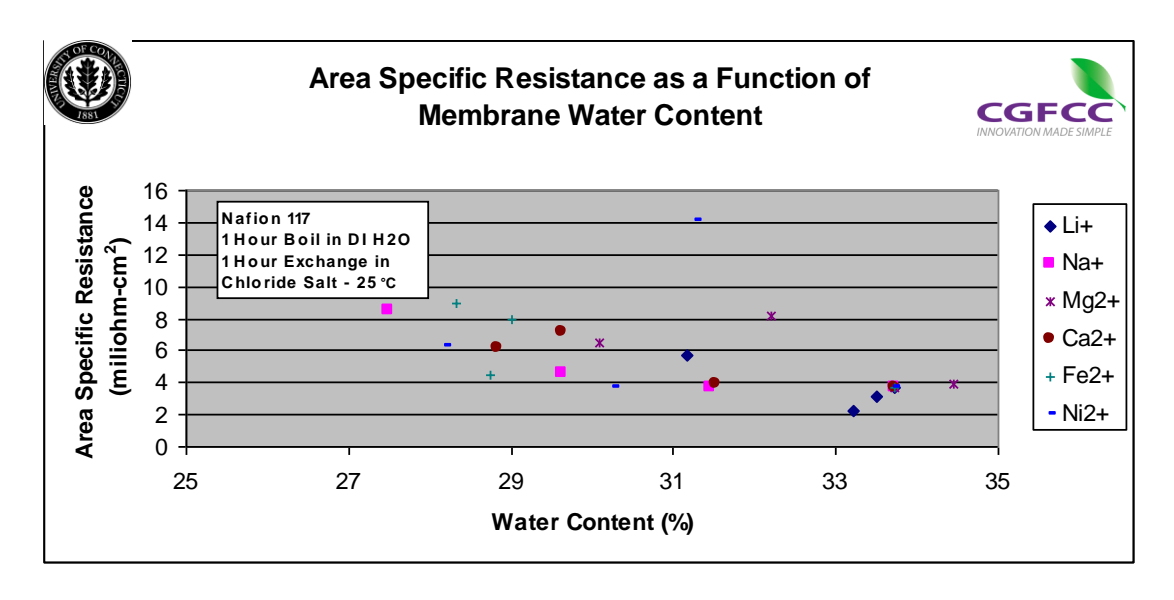


Figure 39 Membrane Area Specific Resistance as a Function of Membrane Water Content

Resistance effects were found to be significant even in membranes exchanged in dilute solutions. Exchange of ions into the membrane caused an increase in membrane resistance. This correlates well with both ion exchange capacity measurements and water content measurements wherein the membranes where shown to pick up appreciable amounts of ions (consuming 90% of available ion exchange sites) also resulting in a loss of water.

Membranes contaminated with lithium surprisingly showed a decrease in measured resistance. Some of this may have been due to the high mobility of the small lithium ions thereby contributing to some of the ion motion during application of the AC current. The literature reports that a lithium ion has a diameter of 94 pm versus the diameter of a hydronium ion of 115 pm (believed to be the charge carrier in a PEMFC and PEMEC) lending credence to this concept.

The data collected indicate that the area specific resistance is nearly linear with membrane water content, with the exception of the membranes contaminated with ferrous ions. The area specific resistance of membranes contaminated with ferrous ions $(8 \text{ m}\Omega.\text{cm}^2)$ is significantly higher than that of membranes having other contaminants $(4 \text{ m}\Omega.\text{cm}^2)$. These data do not correlate with the fact that membranes contaminated with ferrous ions show a higher equilibrium ion exchange capacity than those contaminated with other ions. In this regard only 40% of the membrane IEC was found to be consumed with the ferrous ions as compared to $90^+\%$ for the other ions considered in this study. Data also show that lightly contaminated membranes which show a high ion exchange capacity show a low area specific resistance while those

demonstrating a low ion exchange capacity have a comparable high area specific resistance.

Our prior work exposed membranes to relatively concentrated solutions of chloride salts of these ions. This may not be realistic for a transportation or stationary power application, as these impurities may enter the system entrained in either the hydrogen fuel or the air stream landing on the MEA and exchanging into the membrane. The real concentration within the membrane may therefore be much lower than our earlier investigations evaluated. During this period, new tests were initiated with membranes soaked for one hour in salt concentrations of 0.00001 molar and the membrane samples were tested for hydrogen, oxygen, and nitrogen permeability at room temperature.

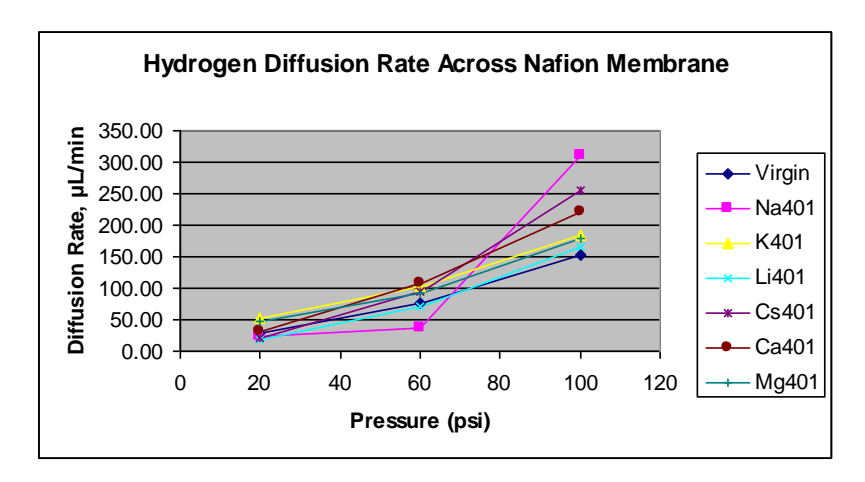


Figure 40 Hydrogen Permeation Rate Across Nafion 117 Membrane. Membranes

Treated for 1 Hour in 0.00001 Molar Chloride Salt of Associated Ion

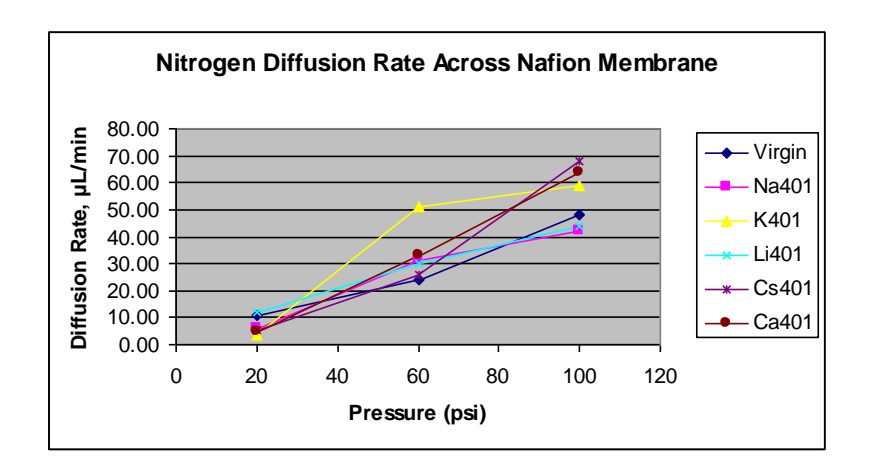


Figure 41 Nitrogen Permeation Rate Across Nafion 117 Membrane. Membranes

Treated for 1 Hour in 0.00001 Molar Chloride Salt of Associated Ion

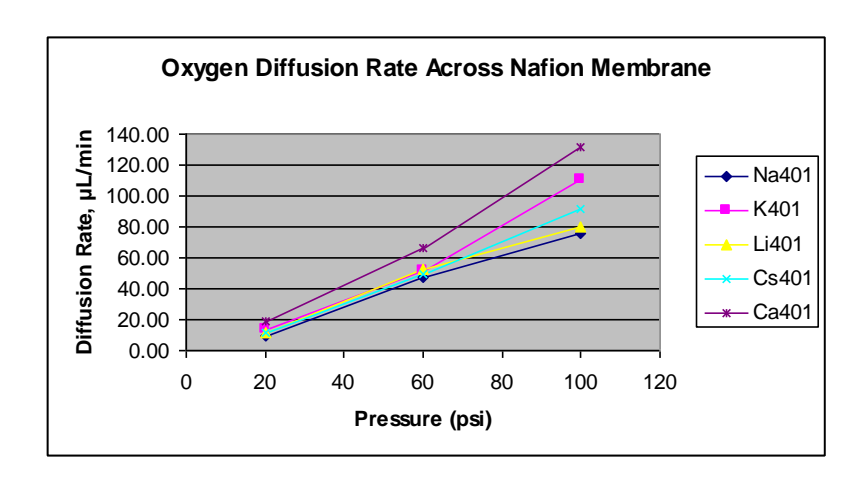
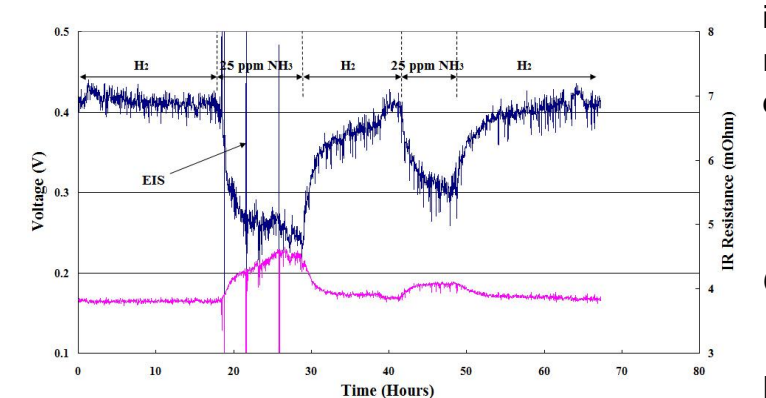


Figure 42 Oxygen Permeation Rate Across Nafion 117 Membrane. Membranes
Treated for 1 Hour in 0.00001 Molar Chloride Salt of Associated Ion

Ammonia Testing

Ammonia appears to be a significant potential source of contamination to operating cells. It is highly likely that ammonia entering the cell will be converted to the ammonium ion, and therefore that has been the focus of our research in this regard. In the cyclical contamination-recovery test of 25 cm² MEA 25 ppm NH₃ is introduced into the anode during contamination sections. During recovery sections, neat H₂ was fed



into the anode. The cell was running at 1.0 A/cm² at 52 °C with dew points at 50 °C.

Figure 43 Cyclical Contamination - Recovery Tests

Data show that the ammonium ion

has a significant effect on cell performance. These documented effects provided input to our modeling efforts.

Cleaning Procedure Development

With constant switching between organic impurities, it was determined that a cleansing procedure needed to be developed for cell and system components and implemented prior to beginning a new test. The cleaning procedure for the metallic and non-metallic parts involve a multi-step process that combine a cleaning, rinsing, draining and drying steps to ensure cleanness of the components in the experimental setup. The cleaning

is performed at or slightly above room temperature. Solvent-free water based aqueous solutions and/or petroleum-based cleaning and rinsing solutions are used during the cleaning. Water or solvent rinsing is needed after the final cleaning. Non-chlorofluorohydrocarbon (CFC) based cleaning agents, especially water-based detergents, exhibit a much slower evaporation rate leave a significant amount of residue after complete drying of the surfaces. These agents are flushed, rinsed or immersed as a final step during the cleaning process to extract the residues. Common organic solvents are also used.

The type of contaminants that are expected to be cleaned from the equipment include:

- Hydrocarbons oils and greases
- Fluorinated fluids and greases
- Carbon deposits
- Silicone oils and greases
- Waxes

ASTM cleaning methods were adopted for use in this program. These techniques include:

- **1.** ASTM A 380 Standard Practice for Cleaning, Descaling, and Passivation of Stainless Steel Parts, Equipment, and Systems.
- 2. ASTM G 127 Standard Guide for the Selection of Cleaning Agents for Oxygen Systems
- 3. ASTM G131 Standard Practice for Cleaning of Materials and Components by Ultrasonic Techniques.

The following summarizes cleaning processes used:

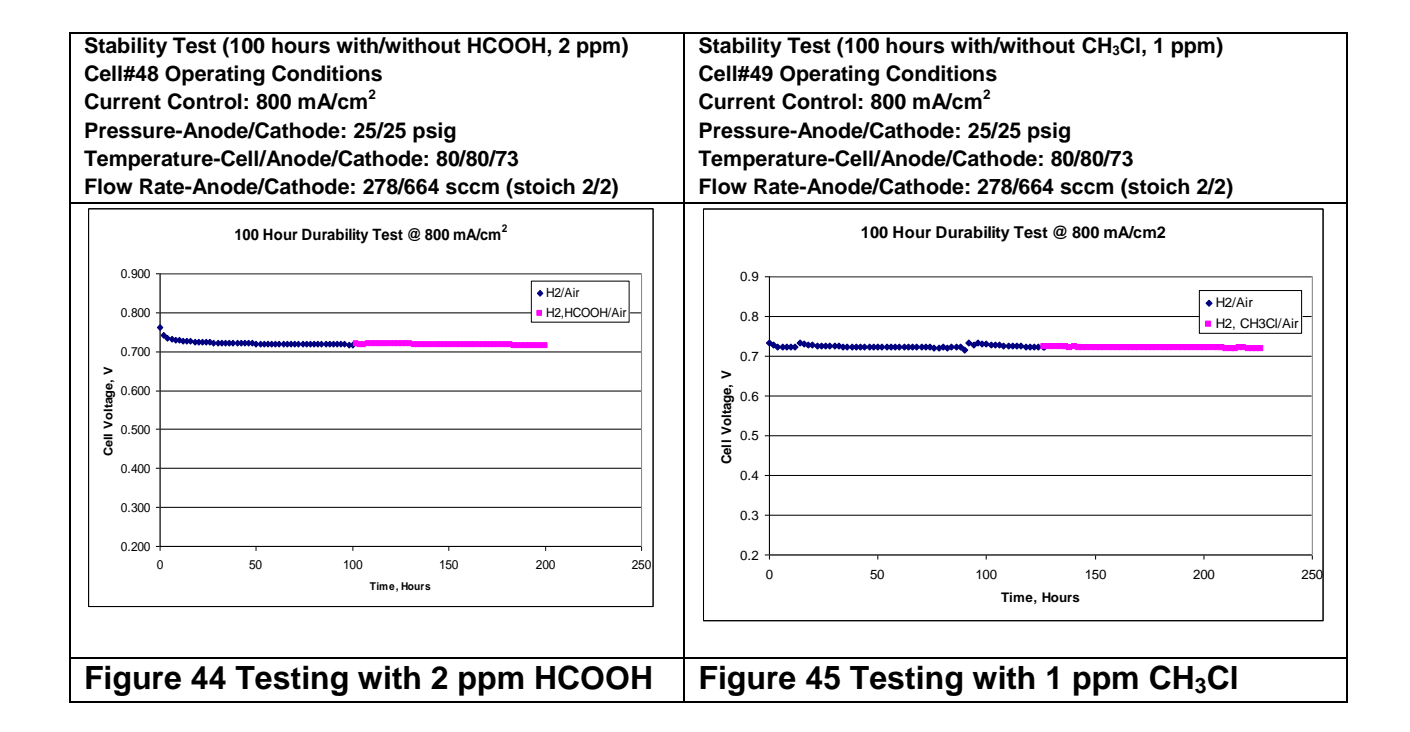
- 1. Heated: the metal components are heated with cleaning agents; solvents and/or water based detergents compatible with metallic materials. Two types of cleaning agents are used:
 - Solvent-free water based aqueous solutions: a general-purpose degreaser. It removes oil, light grease, and soil from metal, glass and plastic. It is also a phosphate-free, non-toxic, non-caustic, nonflammable, and nonabrasive compound.
 - Petroleum-based cleaning and rinsing solutions: an ammonia-free solution.
 Prevent rust, and it is used with a rinsing solution to remove residue and contaminants. The rinsing solution dissolves any residue that is left from

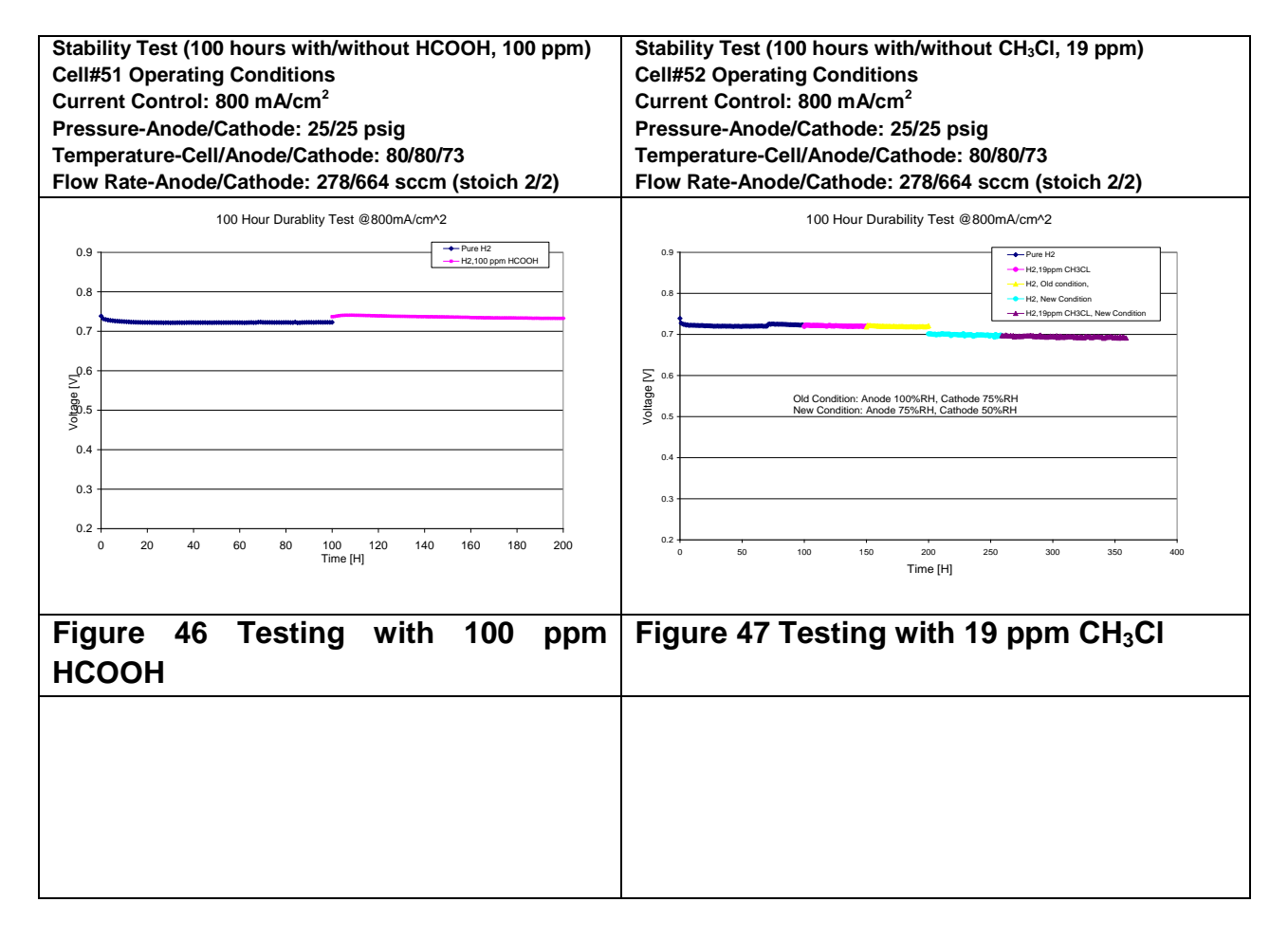
- cleaning solutions. It is a blend of petroleum-based materials and contains no chlorinated solvents. The cleaning agents are applied by immersion.
- 2. Ultrasonic agitation: used in conjunction with the solvent and/or detergent cleaners to loose and remove contaminants from difficult to reach areas, particularly in small work pieces. Cavitations in the liquid produced by the high frequency sound causes micro agitation of the solvent in even tiny recesses of the work piece. It produces high level of cleanliness and it is appropriate for cleaning small parts, components and tubing.

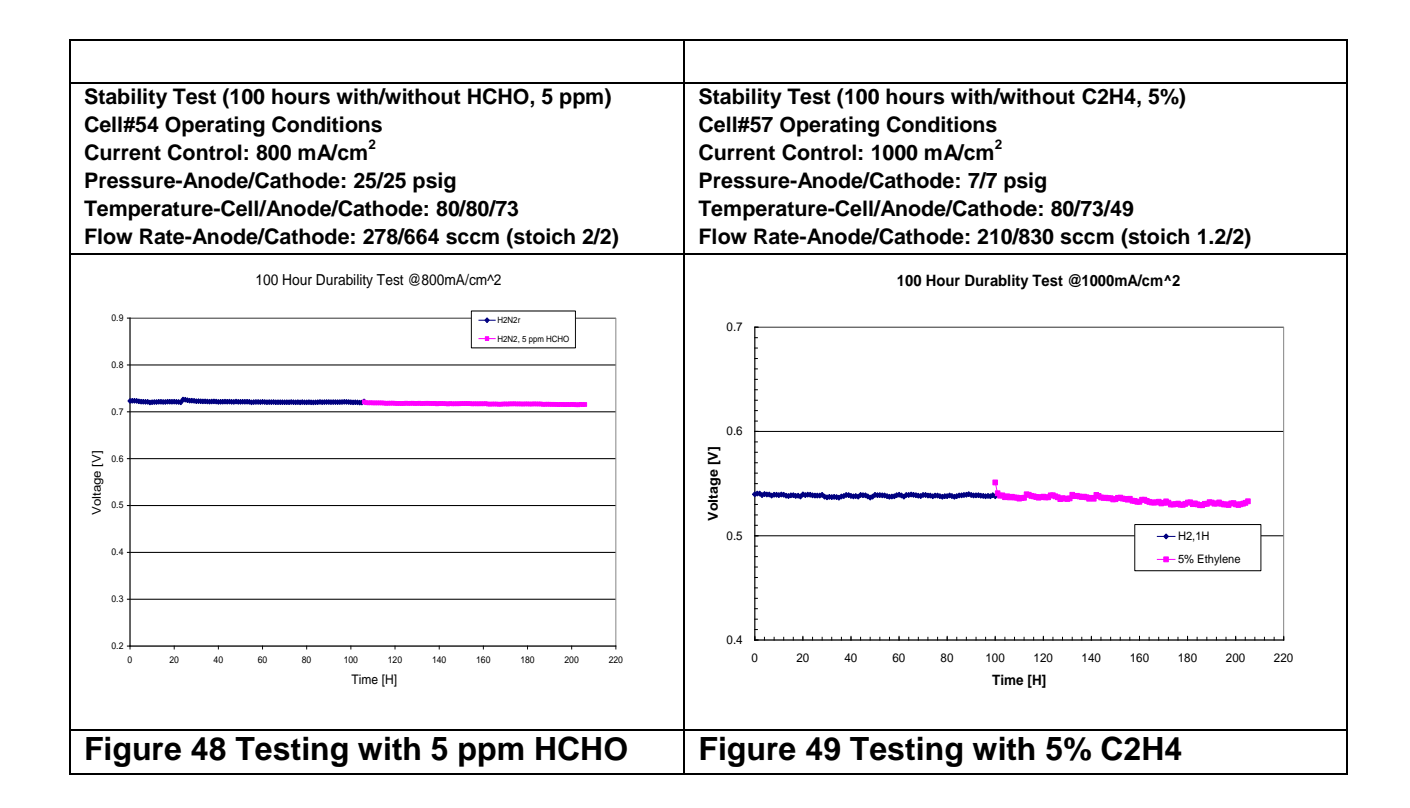
Gas Mixture Testing

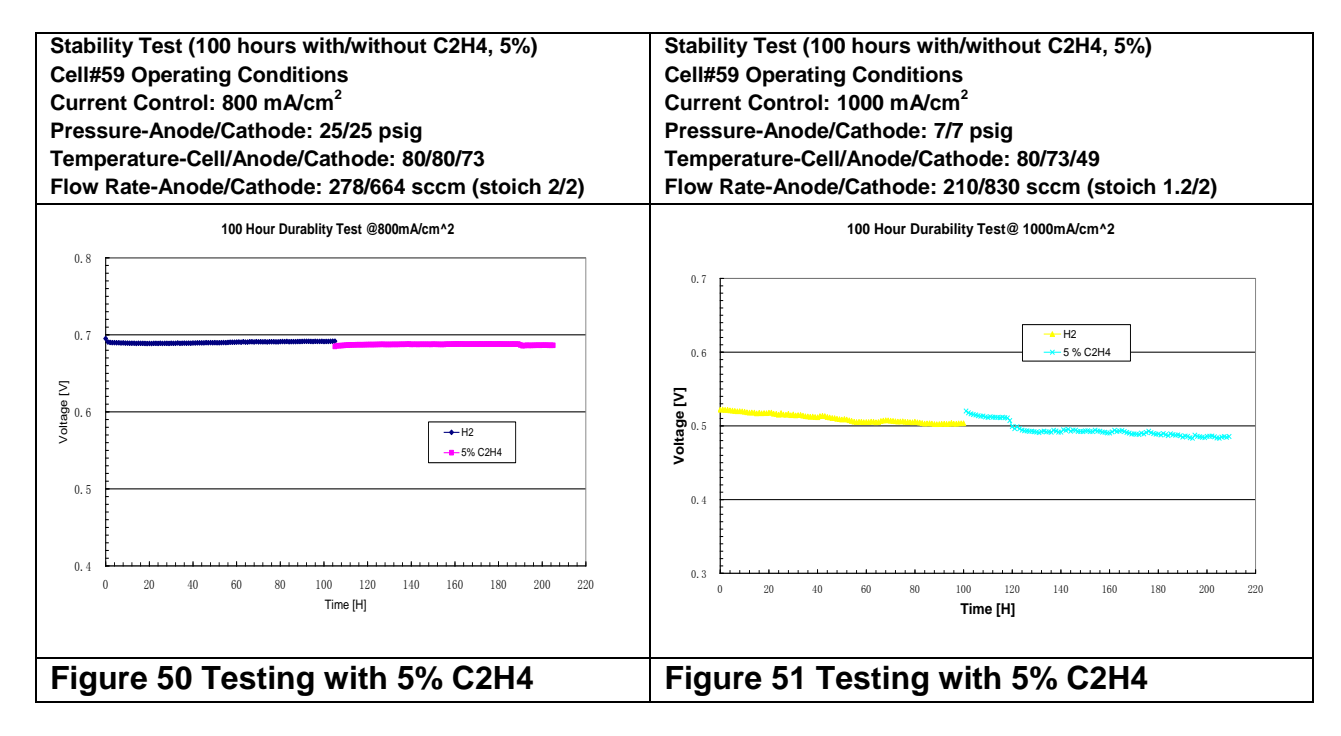
As the international hydrogen fuel quality specification became better defined, it became apparent that testing of impurity mixtures would become important – particularly with regard to competitive and/or additive effects of various contaminant species. Butfirst, single contaminant tests were repeated using the new Gore MEA's. These tests are summarized below.

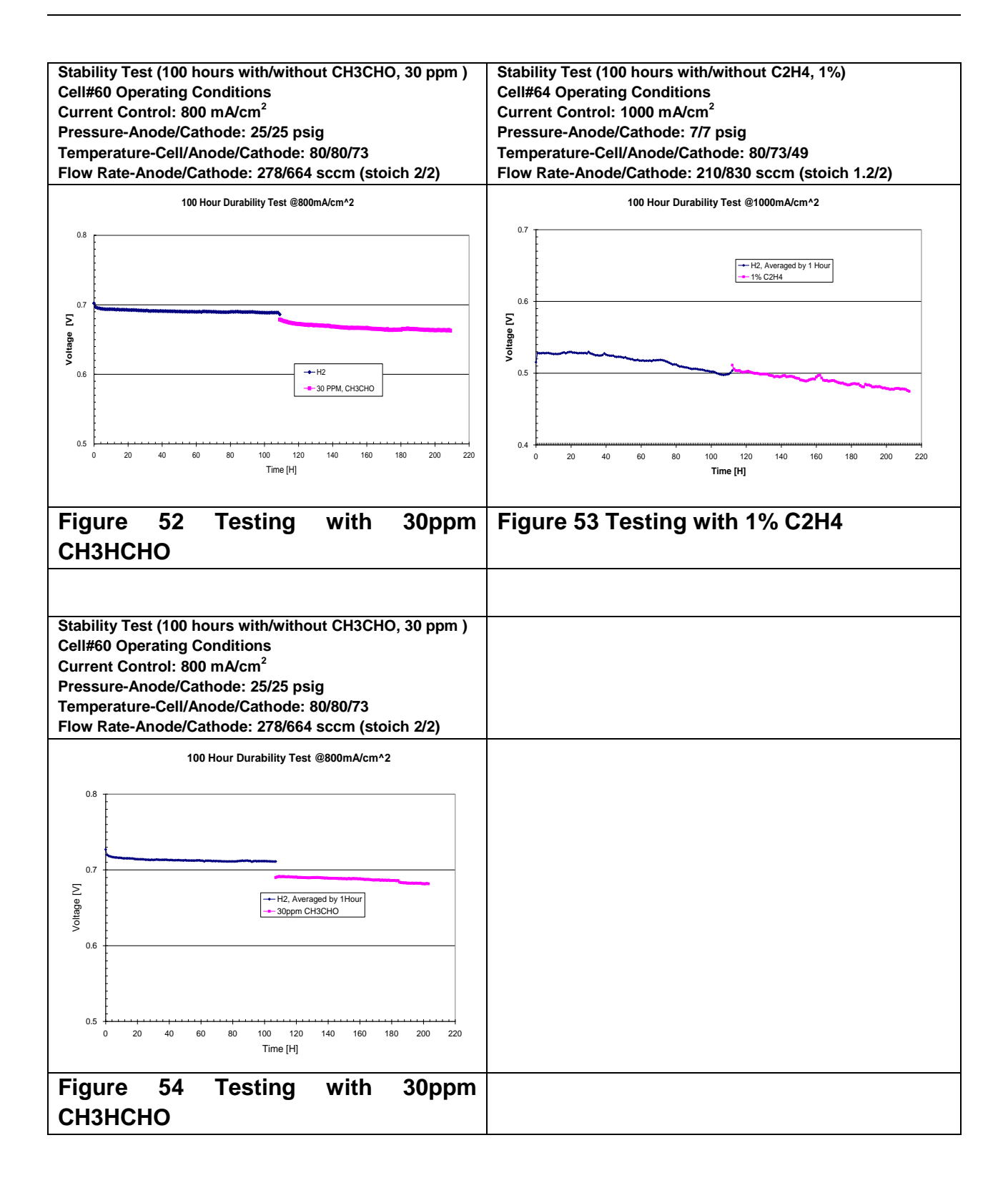
100 hour durability tests with hydrogen and 3% nitrogen; and 1 ppm formaldehyde in hydrogen and 3% nitrogen were performed with the PRIMEA® membrane. After operating for 100 hours on hydrogen at 800 mA/cm² formaldehyde was then added to the hydrogen stream and operated for an additional 100 hours on hydrogen and 1 ppm formaldehyde. No degradation was observed during testing with formaldehyde at 1 Testing with 5 ppm formaldehyde in hydrogen and 16.5% nitrogen was ppm. performed, but still no performance degradation was found (shown in Figure 48). Higher concentration formic acid was retested with the PRIMEA® membrane to compare results against earlier tests with Ion Power MEA's. 100 hour durability test with hydrogen and 100 ppm formic acid in hydrogen were tested at 800 mA/cm² (shown in Figure 46), and smaller degradation rate (10 mV drop over 100 hours) was found compared to the case using Ion-Power MEA's (30 mV drop over 100 hours). 100 hour durability test with hydrogen and 19 ppm chloromethane in hydrogen were tested at 800 mA/cm², and showed no degradation during testing as can be seen in Figure 47. Three cells were tested with 5% ethylene with hydrogen as seen in Figure 49 - 51. Test conditions were repeated for similar tests that were conducted with Ion Power MEA's to compare contaminant impact against the PRIMEA® MEA performance. No obvious degradation was observed for all test conditions. 100 hour durability test for 1% ethylene with hydrogen was conducted and showed signs of a higher then normal degradation rate with both pure hydrogen and 1% ethylene with hydrogen. Further testing is ongoing to discover the cause. Two 100 hour durability tests were conducted for 30 ppm acetaldehyde with hydrogen at 800 mA/cm² as seen in Figures 52 and 54 with no degradation observed.











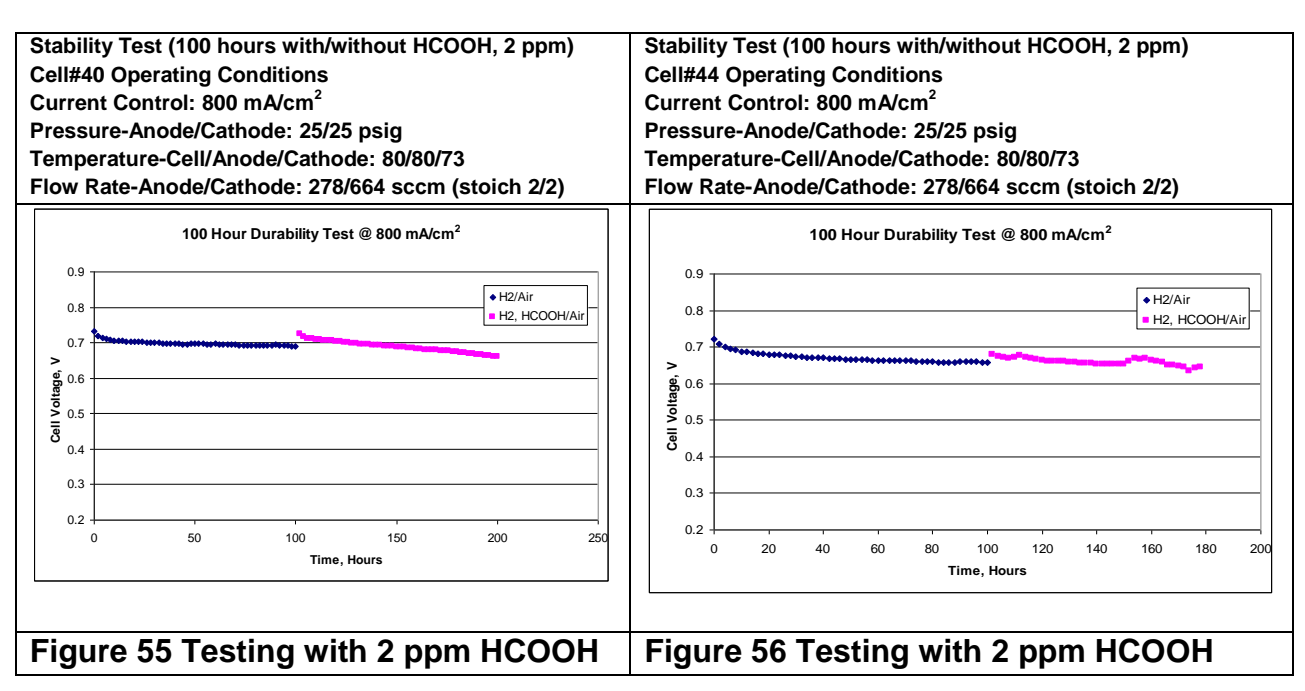
Hydrocarbon Testing Summary

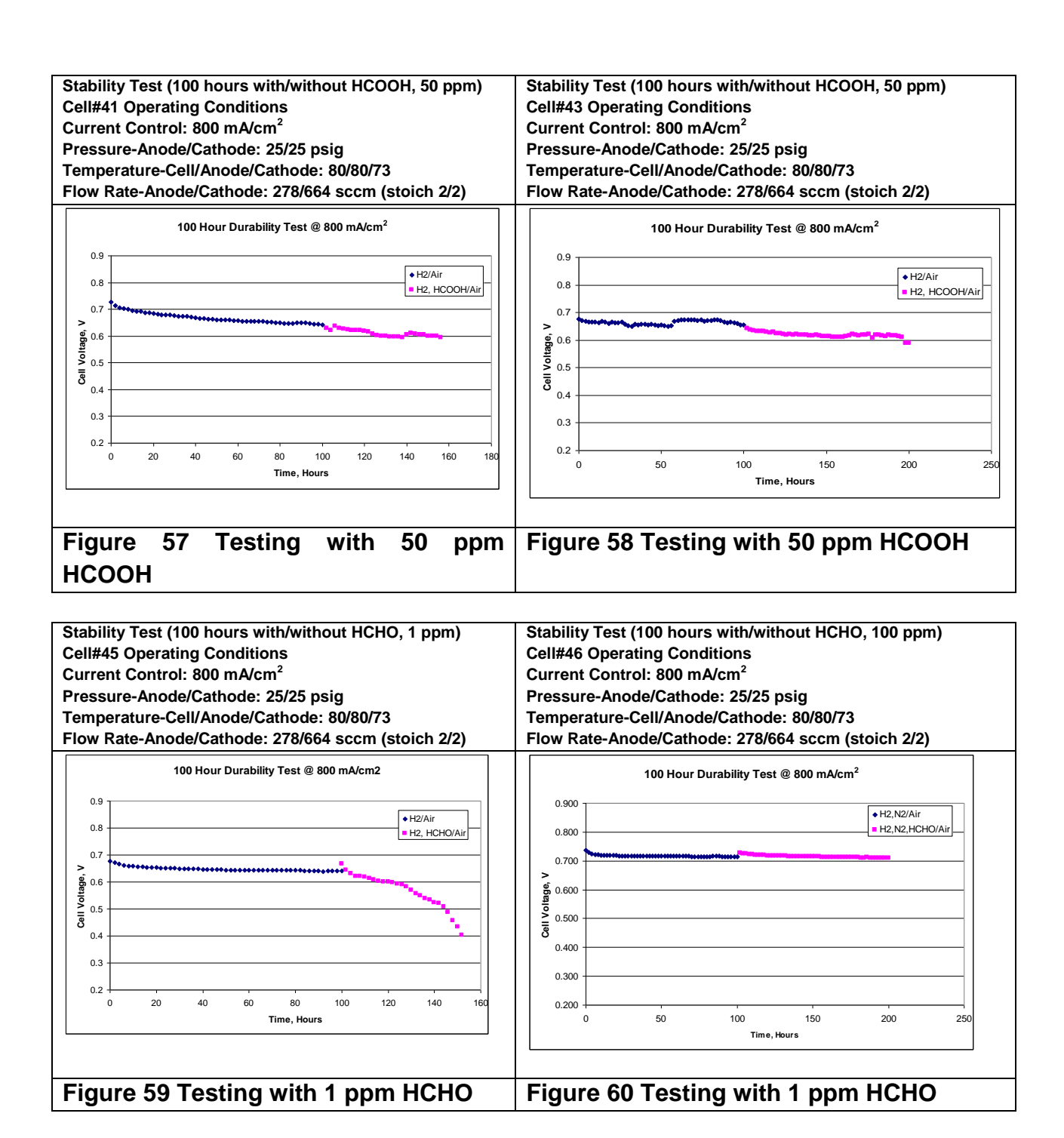
Testing to date of hydrocarbon impurities is summarized in the matrix shown in Table VIII.

Table VIII Summary of Fuel Cell Testing Using Organic Impurities

Cell	MEA	Current	RH (A/C)	Stoich	Contaminant	Results
		Density	(%)	(A/C)		
1	Ion Pwr	200 mA/cm ²	100 / 100	1.3 / 2.0	100 ppm CH ₄	No significant degradation
2	Ion Pwr	600 mA/cm ²	100 / 100	1.3 / 2.0	100 ppm CH ₄	No significant degradation
3	Ion Pwr	600 mA/cm ²	100 / 100	1.3 / 2.0	5% CH ₄ or 5% N ₂	No significant degradation
4	Ion Pwr	800 mA/cm ²	100 / 100	1.3 / 2.0	100 ppm CH ₄	No significant degradation
6	Ion Pwr	600 mA/cm ²	100 / 100	1.3 / 2.0	5% C₂H ₆	No significant degradation
7	Ion Pwr	800 mA/cm ²	100 / 100	1.3 / 2.0	5% C₂H₄	No significant degradation
11	Ion Pwr	800 mA/cm ²	100 / 100	1.3 / 2.0	30 ppm CH₃CHO	No significant degradation
31	Ion Pwr	800 mA/cm ²	100 / 75	2.0 / 2.0	100 ppm CH₃CHO	No significant degradation
35	Ion Pwr	800 mA/cm ²	100 / 75	2.0 / 2.0	100 ppm HCOOH	Significant degradation
38	Ion Pwr	800 mA/cm ²	100 / 75	2.0 / 2.0	50 ppm HCOOH	Some degradation
40	Ion Pwr	800 mA/cm ²	100 / 75	2.0 / 2.0	2 ppm HCOOH	No significant degradation
41	Ion Pwr	800 mA/cm ²	100 / 75	2.0 / 2.0	50 ppm HCOOH	Some degradation
43	Ion Pwr	800 mA/cm ²	100 / 75	2.0 / 2.0	50 ppm HCOOH	Some degradation
44	Ion Pwr	800 mA/cm ²	100 / 75	2.0 / 2.0	2 ppm HCOOH	No significant degradation
45	Ion Pwr	800 mA/cm ²	100 / 75	2.0 / 2.0	1 ppm HCHO	No significant degradation
46	Gore	800 mA/cm ²	100 / 75	2.0 / 2.0	1 ppm HCHO	No significant degradation
48	Gore	800 mA/cm ²	100 / 75	2.0 / 2.0	2 ppm HCOOH	No significant degradation
49	Gore	800 mA/cm ²	100 / 75	2.0 / 2.0	1 ppm CH₃Cl	No significant degradation
51	Gore	800 mA/cm ²	100 / 75	2.0 / 2.0	100 ppm HCOOH	Some degradation
52	Gore	800 mA/cm ²	100 / 75	2.0 / 2.0	19 ppm CH₃Cl	No significant degradation
54	Gore	800 mA/cm ²	100 / 75	2.0 / 2.0	5 ppm HCHO	No significant degradation
57	Gore	1000 mA/cm ²	75/ 25	1.2 / 2.0	5% C2H4	No significant degradation
59	Gore	800 mA/cm ²	100 / 75	2.0 / 2.0	5% C2H4	No significant degradation
59	Gore	1000 mA/cm ²	75 / 25	1.2 / 2.0	5% C2H4	N/A
60	Gore	800 mA/cm ²	100 / 75	2.0 / 2.0	30 ppm CH3CHO	No significant degradation
64	Gore	1000 mA/cm ²	75 / 25	1.2 / 2.0	1% C2H4	No significant degradation
66	Gore	800 mA/cm ²	100 / 75	2.0 / 2.0	30 ppm CH3CHO	No significant degradation
69	Gore	1000mA/cm ²	75/25	1.2/2.0	20 ppm C7H8	No significant degradation
71	Gore	1000 mA/cm ²	75/25	1.2/2.0	30 ppm CH3CHO	No significant degradation
74	Gore	1000 mA/cm ²	75/25	1.2/2.0	10 ppm C7H8	No significant degradation
					1 ppm CO	
					10 ppm C6H6	
75	Gore	1000 mA/cm ²	75/25	1.2/2.0	10 PPM C6H6	No significant degradation
76	Gore	1000 mA/cm ²	75/25	1.2/2.0	10PPM C6H6	No significant degradation
					1PPM CO	
		_			10PPM C7H8	
77	Gore	1000 mA/cm ²	75/25	1.2/2.0	20ppb H2S, 1ppm CO,	Degradation
					10ppm C6H6, 1ppm	
					HCOOH, 500ppb NH3	
78	Gore	1000 mA/cm ²	75/25	1.2/2.0	20ppb H2S, 1ppm CO,	N/A
					10ppm C6H6, 1ppm	
]	HCOOH, 500ppb NH3	

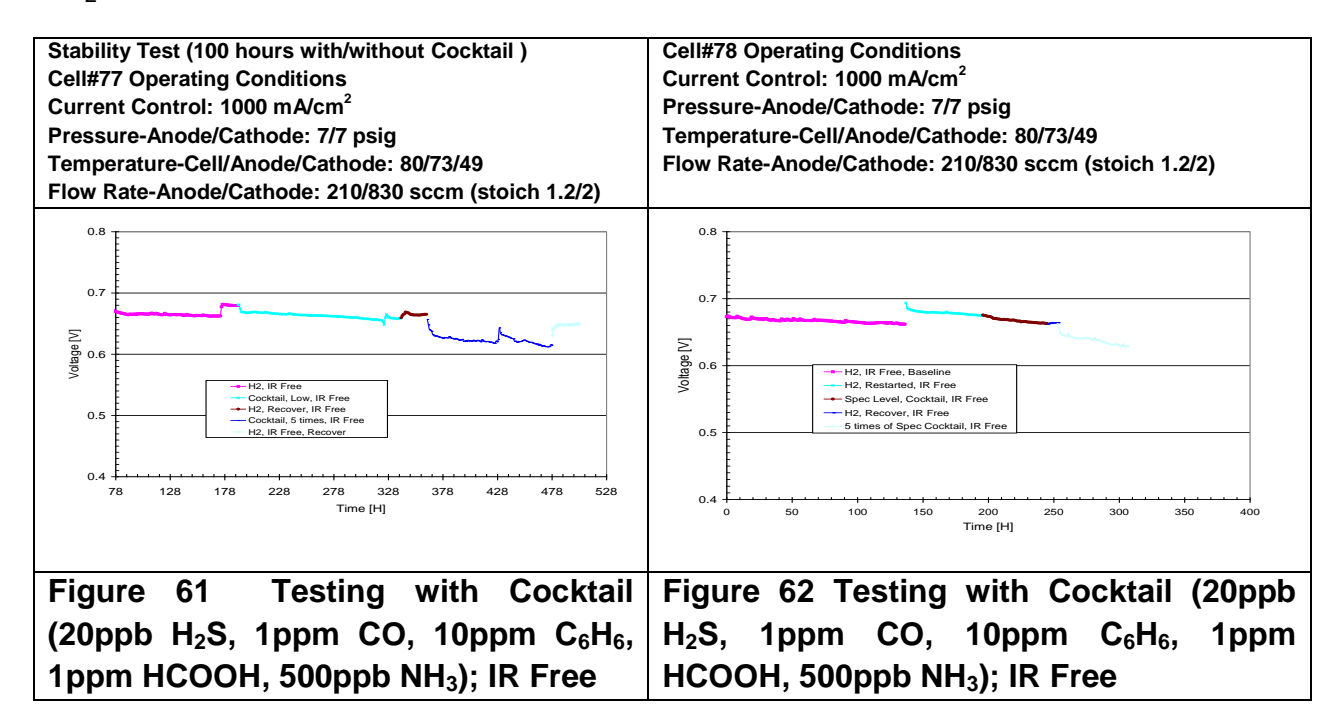
Laboratory testing has shown that simple alkanes, such as methane and ethane, simple alkenes such as ethylene, and simple aldehydes such as acetaldehyde do not significantly affect fuel cell performance under controlled tests, even in relatively high concentrations (up to 5%). When the fuel cell is challenged with quantities of formic acid, some performance degradation is evident. However, low concentrations of formic acid at 2 ppm did not show signs of performance degradation. Formaldehyde was tested at 1 ppm and 5 ppm, and also did not show signs of performance degradation. Continued membrane stability problems with Ion Power membranes and requests from technical and industrial partners for a more relevant commercial product led to testing with the Gore PRIMEA® membranes. Figures 55-60 show the various degrees of problems encountered while testing with Ion Power membranes including shorter lifetimes and performance oscillation.





Figures 61 and 62 show the cocktail contaminant test results. The concentration level of the cocktail is 4ppb H_2S , 200ppb CO, 2ppm C_6H_6 , 200ppb CO and 100ppb CO and 100ppb CO and five times the concentration level is 20ppb CO, 1ppm CO, 1ppm CO, 1ppm CO and 500ppb CO are tested. The test sequence is around 100 hours' pure CO

test for baseline; then anode gas switched to the cocktail specification level for 50 to 100 hours; then 50 to 100 hours recovery test with pure H_2 ; the five times concentration of the specification level was then run for 100 hours; followed by pure H_2 recovery test. From the test results, it can be seen that specification level of cocktail contaminant showed no obvious effects on cell performance. With 5 times of specification level cocktail contaminant, the cell showed a higher degradation rate than testing with pure H_2 .



Task 4.0 Contaminant Model Development

A two dimensional model for a PEFC was developed as part of this task. The model represents the thermal-fluid phenomena, as well as the cation transfer inside the polymer electrolyte membrane. The cation transfer model represents is used to investigate the effects contaminations in the air and fuel streams. The model is developed taking into account the multicomponent cationic species transfer.

There have been substantial efforts in characterizing the effects of cationic contaminants in PEFCs operation¹⁻⁴ as well as characterizing the properties of the cations in the membrane⁵⁻¹⁰. However, there is a little work presented in the open literature to describe the degradation mechanisms of the cationic contaminants. The first attempts are by Okada who developed a simple model to outline the effects of contaminants on the water transport in the membrane for both anode side¹¹ and cathode side¹² impurities. These studies neglect the transport of the cations and

assume an infected zone in the membrane where a prescribed profile (either linear or constant) for cations is considered. Sodaye et al. 13 used Maxwell-Stefan approach to model the cationic exchange in a polymer electrolyte membrane in the presence of two different foreign cations. They are solely interested in the competitive transport of different cations in the membrane and do not consider fuel cell operation. Kienitz et al. 14 developed a one dimensional model for a fuel cell cathode and predicted the cation concentration profiles in the fuel cell cathode. Their model assumes constant current density and does not provide an expression to describe the cathode reaction kinetics; hence it does not relate the effects of cations on the performance loss substantially. Greszler et al. 15 developed a model for a hydrogen pump to investigate the effects of local proton concentration on the reversible potential of the reaction. Their study is significant as they put forward the thermodynamic aspects of the effects of contamination the first time. The most rigorous study up to now is provided by Weber et al.¹⁶ who used concentrated solution theory to model the interactions between each cation and the water while they neglect the interactions between two cation pairs in a polymer electrolyte membrane. Their model is utilized to represent a hydrogen pump.

Albeit their individual strengths in explaining the cation transport in the polymer electrolyte membrane, all of the models cited above have some simplifications and none of them considers a complete fuel cell with both anode and cathode reactions. Also none of these models incorporate the coupled transport phenomena related to oxygen and hydrogen mass transfers as well as water transfer in the electrodes. Since the transport properties of the contaminants depend on fuel cell operational variables such as water content, the model needs to have a very good representation of the transport phenomena in the full cell operation. Moreover, all of the above studies are one dimensional. In order to have a model representing the fuel cell operation accurately two dimensional effects need to be taken into account because a lower level model is not capable of modeling the water transport in the membrane. Due to the water accumulation under the bipolar plate rib area, there is expected to have a significant water concentration gradient in the transverse direction, i.e. from channel to the current collector landing, as well is in the through plane direction, i.e. from anode to cathode. Three dimensional effects along the flow direction can however be neglected if the fuel flow rates are high enough so that the deviations in species concentrations in the flow direction are small.

In this study a modeling framework is presented to elucidate the cation transport in the polymer electrolyte membrane as well as to determine the mechanisms leading to performance degradation of a fuel cell. The equations are derived to describe the cation transport and validated them with the available experimental data. Then these equations are incorporated into the fuel cell model which is capable of solving for the

transport phenomena pertaining to the fuel cell operation which are believed to have a significant impact on the cation transport. With the fuel cell model we tend to explain how the nonprotonic cations have an effect on the performance degradation of an operating fuel cell.

Thermal Fluids Model Description

The PEFC model can be outlined in three main sections: thermal fluids model, cation transport and electrochemical model, and the solid mechanics model. Thermal fluids model incorporates coupled mass, species, momentum and heat balances. Cation transport and electrochemical model incorporates the transport of the cationic species and the ionic charge transfers coupled with the electronic charge transfer, as well as electrochemical kinetics. Solid mechanics model, which will be presented in the next chapter, represents the deformation characteristics of the PEFC under stresses due to swelling of the membrane and the temperature field.

For the contamination studies an isothermal model is considered whereas for the investigation of mechanical stresses model takes into account non-isothermal effects. Figure 63 shows the two dimensional model geometry with the details of the subdomains along with the three dimensional fuel cell geometry to show how the model domain is constructed. In the, anode and cathode GDLs, and anode and cathode CLs where fluid is assumed in gaseous form, continuity, momentum and species equations are solved. For water in the membrane a separate species balance is considered. Electronic charge balance is solved in the GDLs and the CLs whereas ionic charge balance is coupled with the species balance to model the cation transfer in the CLs and the membrane. Heat equation is solved in the entire model domain.

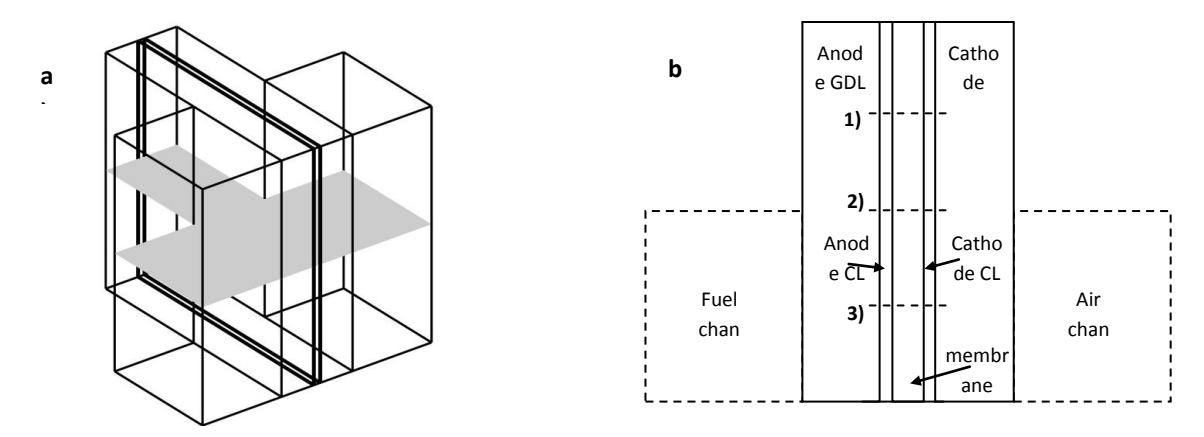


Figure 63 a) 3D Fuel Cell Geometry. 2D Model Geometry is Constructed on the Shaded Cross-Section. b) Model Subdomains are Shown on the Cross-Sectional View

Solid mechanics model incorporates the constitutive relations for the isotropic membrane and the CL and the orthotropic GDL. Force equilibrium equations in the conservative form are solved in these subdomains to calculate the stresses from the deformation field.

Governing Equations

Mass and Momentum Balance

Continuity equation is solved to account for mass balance,

$$\nabla \cdot (\rho \mathbf{u}) = 0 \tag{1}$$

where the density of the mixture is calculated as,

$$\rho = \frac{p}{RT} \sum_{j} x_{j} M_{j} \tag{2}$$

where x_j is the mole fraction of the species determined from the species balance and M_j is the molecular weight of the species. Velocity in Eq. 1 is calculated through Darcy's Law which is the homogenization of the porous medium after neglecting the boundary layer effects at the pore walls.

$$\mathbf{u} = -\frac{K}{\mu} \nabla p \tag{3}$$

where μ is the dynamic viscosity of the mixture and K is the permeability of the medium.

In the anode and cathode catalyst layers, Eq. 1 is modified to take into account of homogenous reactions and electro-osmotic drag. In the anode catalyst layer, hydrogen is depleted and transformed into H^+ , which is absorbed into the ionomer phase. Also water is adsorbed into the ionomer phase from the fluids (gas or liquid) phase and transferred through the membrane via electro-osmotic drag. In the cathode, H^+ transferred through the membrane reacts with the oxygen to form water in the fluid domain. Also H_2O back-diffused to anode from cathode is transferred into the fluid phase from the ionomer phase. Hence, continuity equation, which is defined for only fluid domain is modified such that in the anode stream, mass of hydrogen and water is consumed whereas in the cathode stream water mass is generated. Then appropriate source terms are set in the continuity equation accordingly as $\sum R_j = R_{H_2} + R_{H_2O}$ at the anode and $\sum R_j = R_{O_2} + R_{H_2O}$ at the cathode where,

$$R_{H_2} = -i_a / (2F) M_{H_2} \tag{4}$$

$$R_{H_2O} = \begin{cases} -\nabla \cdot \left(\sum_{j=1}^{n} n_{d,j} \mathbf{N_j}\right) M_{H_2O} & \text{at the anode CL} \\ i_c / (2F) M_{H_2O} + \nabla \cdot \left(\sum_{j=1}^{n} n_{d,j} \mathbf{N_j}\right) M_{H_2O} & \text{at the cathode CL} \end{cases}$$
(5)

$$R_{O_2} = -i_c / (4F) M_{O_2} \tag{6}$$

Electro-osmotic drag appearing in $R_{\rm H_2O}$ as mass termination at the anode and generation at the cathode accounts for the total transference of water by all the cations in the system. The same source terms are used in the Maxwell-Stefan equations with the exception that $R_{\rm H_2O}$ is defined only at the cathode as water is treated as the background species at the anode. Solving the Maxwell-Stefan equations with the continuity equation takes care of the conservation of mass for water at the anode.

Species balance for anode and cathode gas mixtures

Multi-component species transport is modeled with Maxwell-Stefan equation in the form developed by Curtis and Bird⁶⁹ which can be written for ideal gas mixtures as

$$\nabla \cdot \left[\rho w_j \mathbf{u} - \rho w_j \sum_{k=1}^n \widetilde{D}_{jk} \left(\nabla x_k + (x_k - w_k) \frac{\nabla p}{p} \right) \right] = R_j$$
 (7)

which is solved for hydrogen at the anode and oxygen and water at the cathode. Mass fractions of the background species which are water at the anode and nitrogen at the cathode are determined via.

$$\sum_{j=1}^{n} w_{j} = 1 \tag{8}$$

In Eq. 7, R_j is the source terms for each species which are calculated from Eq. (4-6). \tilde{D}_{jk} are the Maxwell-Stefan diffusivities and calculated from binary diffusion coefficients. Binary diffusivities are defined as a function of temperature and pressure and then corrected via Bruggemann correlation to account for porosity of the medium 17

$$D_{jk} = D_{jk}^{0}(T_0, p_0) \left(\frac{T}{T_0}\right)^{1.5} \frac{p_o}{p} \varphi^{1.5}$$
(9)

 D_{jk}^0 is the bulk diffusivity measured at T_0 and p_0 . φ is the void fraction of the porous medium. Bruggemann correlation assumes that tortuosity of the medium is equal to 1.5 and it appears as the power of φ

Energy Balance

Steady state heat equation including the effects of species diffusion is solved to account for energy balance.

$$\nabla \cdot (-k\nabla T + \rho C_p T \mathbf{u} + \sum_{\mathbf{j}} h_j \mathbf{N}_{\mathbf{D}, \mathbf{j}}) = Q$$
(10)

In the porous regions heat equation is formulated by volume averaging. Assuming thermal equilibrium between the gas phase and the solid phase, the volume averaging results in the same form of Eq. 10, with the following modifications: In the porous domains second and third terms are calculated only for the fluid mixture. Porosity corrections are accounted automatically in ${\bf u}$ and ${\bf N}_{{\bf D},{\bf j}}$, which are the velocity of the mixture and the diffusive flux of each species respectively. Further, an effective thermal conductivity is defined such that and $k_{\it eff} = \varphi k_f + (1-\varphi)k_s$ where indices f and g stand for fluid and solid respectively.

Thermal conductivity of the multi-component fluid mixture is estimated via Wassiljewa's expression

$$k_f = \sum_{j=1}^{n} \frac{x_j k_j}{\sum_{k=1}^{n} x_j A_{jk}}$$
 (11)

with the Mason and Saxena modification:

$$A_{jk} = \frac{\left[1 + \xi^{1/2} \left(M_j / M_k\right)^{1/4}\right]^2}{\left[8 \left(1 + M_j / M_k\right)\right]^{1/2}}, \qquad \xi = \frac{\mu_j}{\mu_k} \frac{M_k}{M_j}$$
 (12)

where μ_j is the dynamic viscosity and M_j is the molecular weight of species j. On the other hand a similar expression is used for calculating the gas mixture viscosity¹⁸

$$\mu_f = \sum_{j=1}^n \frac{x_j \mu_j}{\sum_{k=1}^n x_j A_{jk}}$$
 (13)

Heat generation during the fuel cell operation is given distributed over the MEA to consider reversible and irreversible losses separately in each domain:

$$Q = i_{a/c} \left(\eta + T \frac{dU_{0,a/c}}{dT} \right) + \kappa_i \left(\nabla \phi_i \cdot \nabla \phi_i \right) \qquad \text{in the CLs}$$

$$Q = \kappa_i \left(\nabla \phi_i \cdot \nabla \phi_i \right) \qquad \text{in the membrane}$$
(14)

where η : activation overpotential, U_0 : the equilibrium voltage, σ : ionic conductivity of the membrane, ϕ : ionic phase potential which will be described in the next section. Here it is assumed that ohmic loss due to electron transfer is negligible compared to the other contributions to the heat source.

Water Transport

Water transfer in the membrane is accounted separately with the following equation

$$\nabla \cdot \left(D_{w} \nabla \lambda + \sum_{j=1}^{n} n_{d,j} \mathbf{N}_{j} \right) = 0$$
 (15)

where the first term represents the water transport due to diffusion and the second term represents the water transport due to the total electro-osmotic drag. It is assumed that in the membrane water molecules are attached to the cations and dragged due to the movement of the cation in the membrane. $n_{d,j}$ is called the electro-osmotic drag coefficient and defined as the number of water molecules carried by each cation. n_d for membrane in pure proton form is taken as 1 for water vapor. The value for membranes in pure NaM form is taken from Okada et al.⁷.

 $D_{\rm w}$ is the diffusion coefficient of water and it depends on the cation content of the membrane which can be expressed as a linear combination of water diffusion coefficients for the membrane in the single cation form weighted by the relative cation concentration in the mixed form.,

$$D_{w} = \sum_{j=1}^{n} y_{j} D_{w}^{j}$$
 (16)

where y_j is the ratio of each cation in the membrane and calculated in cation transport model. When there is no contamination in the system y_j for Hydrogen is constant and equal to 1.

Water diffusion coefficient for the membrane in proton form is given by Motupally et al. as

$$D_{w} = \begin{cases} 3.1 \times 10^{-7} \lambda (\exp(0.28\lambda) - 1) \exp(-20.252 \times 10^{3} / RT) & \text{for } 0 < \lambda \le 3 \\ 4.17 \times 10^{-8} \lambda (1 + 161 \exp(-\lambda)) \exp(-20.252 \times 10^{3} / RT) & \text{for } 3 < \lambda \end{cases}$$
(17)

For the membrane in Na form water diffusion coefficient is calculated via the following expression¹⁹.

$$D_{j,M}\Big|_{T_0} = D_{H_2O}^0 f(V_p) \tag{18}$$

where $f(V_p)$ represents the tortuosity of the diffusion path and is related to the membrane polymer fraction²⁰ as

$$f(V_p) = \exp(-bV_p/1 - V_p) \tag{19}$$

where b is 0.21 for monovalent cations. V_p can be related to membrane water content as,

$$\frac{V_p}{1 - V_p} \approx \frac{1.\frac{EW_m}{\rho_m}}{\lambda \frac{M_{H_2O}}{\rho_{H_2O}}} = \frac{1100/1.98}{\lambda.18/1} = \frac{1}{0.0324\lambda}$$
(20)

For the membrane in monovalent cation forms $D_{H_2O}^0 = 5.1 \times 10^{-10} \text{ m}^2 \text{ s}^{-1}$. To account for the changes in temperature the same activation energy is used as that given for the membrane in pure proton form.

$$D_w^j = D_{wT_o}^j \exp\left(-20.252 \times 10^3 \left(\frac{1}{R.303} - \frac{1}{RT}\right)\right)$$
 (21)

Boundary Conditions

Maxwell-Stefan Equations

Species mass fractions are fixed at the fuel channel inlet and the outer cathode boundaries,

$$W_j = W_{j,in} \tag{22}$$

At the fuel channel outlet, convective flux boundary condition is imposed to indicate there is no diffusion related mass transfer through this boundary.

$$\mathbf{n} \cdot \left[-\rho w_j \sum_{k=1}^n \widetilde{D}_{jk} \left(\nabla x_k + \left(x_k - w_k \right) \frac{\nabla p}{p} \right) \right] = 0$$
 (23)

It should be noted that in the anode, H_2O is the background species of the Maxwell-Stefan equations. Therefore, boundary conditions are only prescribed for H_2 . If Dirichlet type boundary conditions are specified for H_2 the boundary conditions for H_2O are determined via Eq. 8. On the other hand if Neumann type boundary conditions are specified for H_2 then the ones for H_2O are determined through the continuity using the boundary conditions specified for the momentum equation.

Momentum Equation

Pressure boundary conditions are prescribed for Darcy's Law at the GDL-channel interfaces. The other boundaries are treated with symmetry conditions. At the CL membrane interfaces special attention is required to model the water transport. At the CL-membrane interface water transferred through the membrane either enters or leaves the fluid domain with a velocity which can be calculated from the mass balance.

$$\rho U = -\mathbf{n} \cdot (-D_{w} \nabla c_{w}) M_{H,O} \tag{24}$$

where right hand side is the mass flux calculated by water transport equation at the normal direction of the interface. The negative sign in front of the normal vector \mathbf{n} implies that the calculated mass flux is through the membrane. Therefore for the momentum equation U is specified as the outlet velocity at the CL – membrane boundaries.

Heat Equation

At the flow inlets fixed temperature is assumed as well as the interfaces between the channels and the bipolar plates. The latter is a safe assumption as the bipolar plates have much higher thermal conductivities and the coolant inside the grooves of the BPP flows at a controlled temperature.

At the outlet of the fuel channel boundary conditions are set as convective flux which means any heat transport through that boundary is convection dominated and there is no heat flux due to conduction. The rest of the boundaries are treated as insulation/symmetry planes.

Water Transport

In the catalyst layer membrane interfaces local equilibrium between the gas phase and the ionomer phase is assumed and boundary conditions are given as

$$c_{w} = c_{w}^{eq} \tag{25}$$

where equilibrium value is determined from the water sorption isotherms which is given as a relation between the membrane water content and the local water activity $a=p_w/p_{sat}$

$$\lambda = 0.3 + 6a[1 - \tanh(a - 0.5)] + 3.9\sqrt{a} \left[1 + \tanh\left(\frac{a - 0.89}{0.23}\right) \right]$$
 (26)

Above relation is given by Kulikovsky as a curve fit to Hinatsu's²¹ experiments to characterize water uptake of Nafion at 80°C. For membranes in NaM form the isotherms are given by Jalani and Datta²². Curve fit to their experimental data results in the following relation at 30°C,

$$\lambda_{Na^{+}} = 10.3 \times a^{3} - 4.73 \times a^{2} + 1.78 \times a + 0.0149$$
 (27)

Cation Transport and Electrochemical Model

Governing Equations

Cationic Species Conservation

Cation transport in the CLs and the membrane is modeled by considering species and ionic charge balances simultaneously. Nernst-Planck equations are modified with a Maxwell-Stefan approach to represent the coupled phenomena as

$$-\frac{x_j}{RT}\nabla\mu_j - x_j z_j \frac{F}{RT}\nabla\phi = \sum_{k=1,k\neq i}^n \frac{x_k \mathbf{N_j} - x_j \mathbf{N_k}}{c_{tot}D_{jk}}$$
(28)

Left hand side of the equation represents the diffusion driving force due to the chemical potential of each cation, μ and the electric field, ϕ whereas the right hand side accounts for the friction against the diffusion due to the interactions between each species. For the ideal description of the diffusion in an ion exchange process all the ionic species, ion exchanger matrix and the solvent which is usually water need to be considered in the model⁷⁶. However, in this study it is assumed that the friction transmitted by the water on the cations are negligible compared to the interaction of each cation with the other species as well as the membrane. This assumption can be justified by considering that the self diffusivities of the cations are much smaller in the membrane than those in the aqueous solutions⁵. Thus, diffusion of the water is decoupled from the cation transport. On the other hand, the forces transmitted by the cations on the water molecules are still accounted for, i.e. electro-osmotic drag, as they have a significant contribution on the water transport when compared to the self diffusion of the water.

In Eq. 28 the binary diffusion coefficients are calculated via

$$D_{jk} = D_{j,M}^{x_j/(x_j + x_k)} D_{k,M}^{x_k/(x_j + x_k)}$$
(29)

where $D_{j,M}$ is the self-diffusivity of the cation in the membrane which is a function of temperature and the water content. Self-diffusivities of the cationic species are listed in Table IX. Expressions are determined based on the reference conditions at a certain temperature and water content. In this study the transport of Na⁺ and Cs⁺ in the membrane is considered. The diffusivity for each cation is found in the literature for the membrane in pure homoionic form⁷. However, Yaeger et al.¹⁰ reported that in the membrane when both cations coexist the diffusion characteristics of the cations are different than those for the membrane in pure form. Hence the data of Yaeger et al. are used in this study.

Table IX: Cationic Species Properties

	H ⁺	Na⁺	Cs⁺
Molecular weight (g mol ⁻¹)	1	23	133
Self-diffusivities in aqueous solution (m ² s ⁻¹) ⁵	а	1.33×10 ⁻⁹	2.05×10 ⁻⁹
Activation energies for diffusivities (kJ mol ⁻¹) ¹⁰	а	27.3	35.4
Membrane water (liquid) content, λ , in the pure cationic form 7	22	20	9.7
Electro-osmotic drag coefficient of water for the pure cationic forms, n _d ⁷	2.6	9.2	5.2
^a see text			

For the correction of the self-diffusivities for temperature an Arrhenius type relation is used.

$$D_{j,M} = D_{j,M} \Big|_{T_0} \exp\left(\frac{EA}{RT_0} - \frac{EA}{RT}\right)$$
(30)

where *EA* is the activation energy which is listed in Table 1 for the cations considered in this study. On the other hand for H+ self diffusivity is calculated from the conductivity as

$$\kappa_{H^{+}} = c_{H^{+}} u_{m,H^{+}} z_{H^{+}}^{2} F^{2}$$
(31)

where $u_{\scriptscriptstyle m,H^+}$ is the mobility determined via Nernst-Einstein relation

$$u_{m,j} = \frac{D_{j,M}}{RT} \tag{32}$$

The conductivity of the membrane in pure proton form is determined by Springer et al. ²³

$$\kappa_{H^{+}} = (0.5139\lambda - 0.326) \exp\left(\frac{10.691 \times 10^{3}}{R.303} - \frac{10.691 \times 10^{3}}{RT}\right)$$
(33)

In the multicomponent solution of n species, only n-1 of Eq. 28 are independent due to Gibbs-Duhem restriction. So it is solved for H+, Na+ and Cs+. Eq. 28 is written in terms of species molar fractions in the solution which is written, i.e. for H+, as

$$x_{H^{+}} = \frac{c_{H^{+}}}{c_{H^{+}} + c_{Na^{+}} + c_{K^{+}} + c_{SO_{3}^{-}}}$$
(34)

where $c_{so_3^-}$ is the concentration of the sulfonic acid chains determined as the ratio of the membrane density to the equivalent weight of the membrane. In the catalyst layers sulfonic acid chains concentration is multiplied with ε_m which is the ionomer fraction in the CLs. Assuming local electroneutrality, we have

$$\sum_{i=1}^{n} z_{j} c_{j} = 0 {35}$$

where sulfonic acid chains are considered as negative charged stationary species with a fixed concentration. With the constant $c_{so_3^-}$ assumption, the changes in the density and the equivalent weight of the membrane related to swelling and cation content are neglected.

Here we introduce a new variable called *species relative occupancy* for the mobile ions which is defined as.

$$y_j = \frac{c_j}{c_{SO_3^-}} \tag{36}$$

which can also be interpreted as the fractional coverage of the active sites in the membrane by each cation. Dividing both sides of Eq. 35 by c_{so} we derive the following:

$$\sum_{i=1}^{n-1} z_j y_j = 1 \tag{37}$$

Comparing Eq. 34 and 37 it is seen that $x_j = y_j/2$ for the cations. Using this identity we can rewrite Eq. 28 in terms of species relative occupancy as

$$-\frac{y_j}{RT}\nabla\mu_j - y_j z_j \frac{F}{RT}\nabla\phi = \sum_{k=1,k\neq i}^n \frac{y_k \mathbf{N_j} - y_j \mathbf{N_k}}{2c_{SO}}$$
(38)

where $y_{so_3^-}$ is used instead of $x_{so_3^-}$ for the sake of consistency in the notation and it is equal to 1. Note that total concentration of the mixture is equal to $2c_{so_3^-}$. Equation 38 constitutes a set of equations in which the total fluxes N_i are to be solved. This equation system can be cast into the matrix form such as

$$-\frac{2c_{SO_3^-}}{RT}\{y\nabla\mu\} - \frac{2Fc_{SO_3^-}}{RT}\{y.z\}\nabla\phi = [\mathbf{B}]\{\mathbf{N}\}$$
(39)

where the braces are 3x1 matrices and the [B] is a 3x3 matrix including binary diffusivities and relative occupancies. The elements of [B] can be found in Krishna and Wesselingh.

The chemical potential is

$$\mu_j = \mu_j^0 + RT \ln \left(\frac{a_j}{a_j^0} \right) \tag{40}$$

where μ_j^0 is the chemical potential at the standard state, a_j is the activity of the species and a_j^0 is the activity corresponding to the standard state. Activity can be related to the site occupancy as $a_j = f.y_j$ where f is the activity coefficient accounting for the non-ideality of the solution. f being 1 for the standard state when the membrane is in pure form of the considered cation Eq. 40 can be written as

$$\mu_i = \mu_i^0 + RT \ln(f_i, y_i) \tag{41}$$

In the cation exchange in the polymer electrolyte membrane non-idealities can arise both from the solution related to the nature of the mixture and the adsorption processes related to the physical phenomenon. To distinguish between these two we use superscripts sol and ads to define activity coefficient related to the non-idealities of the solution and the adsorption process respectively. Then chemical potential gradients can be expressed as

$$\nabla \mu_i = RT \Big(\nabla \ln \Big(f_i^{sol}. y_i \Big) + \nabla \ln \Big(f_i^{ads}. y_i \Big) \Big)$$
(42)

For multicomponent mixtures this can be written with the use of total derivative as

$$\nabla \mu_{j} = RT \sum_{k=1}^{n} \frac{1}{f_{j}^{sol}.y_{j}} \frac{\partial \left(f_{j}^{sol}.y_{j}\right)}{\partial y_{k}} \nabla y_{k} + RT \sum_{k=1}^{n} \frac{1}{f_{j}^{ads}.y_{j}} \frac{\partial \left(f_{j}^{ads}.y_{j}\right)}{\partial y_{k}} \nabla y_{k}$$
(43)

where the term in front of the divergence on the right hand side is the thermodynamic correction factor discriminating the real solution from the ideal solution. Carrying on with the differentiation Eq. 43 can be written as

$$\frac{y_{j}}{RT}\nabla\mu_{j} = \nabla y_{j} + y_{j} \sum_{\substack{k=1\\k\neq j}}^{n} \frac{\partial \ln f_{j}^{sol}}{\partial y_{k}} \nabla y_{k} + y_{j} \sum_{\substack{k=1\\k\neq j}}^{n} \frac{\partial \ln f_{j}^{ads}}{\partial y_{k}} \nabla y_{k}$$

$$\tag{44}$$

Forland et al.²⁴ express the activity coefficients related to the non-idealities of the solution for the ion exchange membranes behaving as regular mixtures of two cation4ic forms AM and BM as

$$\ln f_A^{sol} = by_B^2 / RT \qquad \text{and} \qquad \ln f_B^{sol} = by_A^2 / RT \tag{45}$$

where *b* is a constant depending on the cationic exchange system and determined experimentally by Okada et al.⁷. Eq. 45 is written for binary membrane mixture. For ternary membrane mixture of HM/NaM/CsM *b* value for H/Na and H/Cs systems are reported by Okada et al.⁷ and listed in Table X. However, value for the Na/Cs system is assumed based on the following discussion:

Physical meaning of the *b* parameter can be explained as the interactions between the ionic species A⁺ and B⁺ in the membrane. A larger *b* implies more repulsive forces between A⁺-B⁺ than those between A⁺-A⁺ and B⁺-B⁺ pairs. These interactions are related to the water content in the membrane as well as the ratio of the sizes of the cations. As the water content decreases, membrane shrinks and the repulsive forces between the cations of same species would be more than that between different cations⁷. In this context, Rb⁺ and Cs⁺ are expected to show similarity in behavior when they are separately used in an ion exchange system with Na⁺ because the weight ratio of these to that of Na⁺ is comparable as well as the water content of the membrane in the each cationic form. Forland et al.²⁴ has investigated Na/Rb system and reported the value for *b*. A smaller value for Na/Cs system is expected because of smaller membrane water content in the Cs form⁷ but still the value for Na/Rb system is used in our study. This assumption may also be justified by comparing the b values for H/Rb and H/Cs systems which are -873 J mol⁻¹ and -954 J mol⁻¹ respectively⁷.

For the ternary mixture of HM/NaM/CsM the activity coefficients can be calculated based on the superposition of the contributions from different exchange reactions as,

$$\ln f_{H} = b_{H/Na} y_{Na}^{2} / RT + b_{H/Cs} y_{Cs}^{2} / RT$$

$$\ln f_{Na} = b_{H/Na} y_{H}^{2} / RT + b_{Na/Cs} y_{Cs}^{2} / RT$$

$$\ln f_{Cs} = b_{H/Cs} y_{H}^{2} / RT + b_{Na/Cs} y_{Na}^{2} / RT$$
(46)

Table X Species Pairs Interaction Parameters, *b* (J mol⁻¹)

Values
values
235
-873
-954
-1000
-1000

^a assumed values

For the non-idealities related to the adsorption process multicomponent Langmuir isotherms are utilized for the following expression

$$y_{j} \sum_{\substack{k=1\\k\neq j}}^{n} \frac{\partial \ln f_{j}^{ads}}{\partial y_{k}} \nabla y_{k} = \frac{y_{j}}{1 - \sum_{k=1}^{n} y_{k}}$$

$$(47)$$

It is assumed that multicomponent surface adsorption is valid for the foreign cations while H^+ generation and depletion is a phenomenon related to the bulk volume. A problem may arise with Eq. 47 such that when all the sites are occupied by foreign cations denominator goes to infinity. To avoid non-physical values Eq. 47 is corrected as following 25

$$y_{j} \sum_{\substack{k=1\\k\neq j}}^{n} \frac{\partial \ln f_{j}^{ads}}{\partial y_{k}} \nabla y_{k} = \frac{y_{j}}{1 - \sum_{k=1}^{n} y_{k} + c_{f}.y_{j}}$$

$$(48)$$

where c_f is chosen to be 0.1.

After defining the activity coefficients in terms of relative occupancies differentiations in Eq. 44 can be carried out. Replacing chemical potential gradients with the relative occupancy gradients Eq. 39 can be written as

$$-2c_{SO_3^{-}}[\Gamma]{\nabla y} - \frac{2Fc_{SO_3^{-}}}{RT} \{y.z\} \nabla \phi = [\mathbf{B}]{\mathbf{N}}$$
 (49)

where $[\Gamma]$ is the matrix for thermodynamic correction factors calculated from the species activities. Multiplying both sides of this equation with the inverse of [B] we get

$$-2c_{SO_{3}^{-}}[\mathbf{B}]^{-1}[\Gamma]\{\nabla y\} - \frac{2Fc_{SO_{3}^{-}}}{RT}[\mathbf{B}]^{-1}\{y.z\}\nabla \phi = \{\mathbf{N}\}$$
 (50)

where N_j represents the total flux of the cation due to the concentration gradient and electric field. Conservation of mass implies,

$$\nabla \cdot \mathbf{N_j} = R_j \tag{51}$$

For the cations that contaminate the PEM, it is assumed that species uptake to the ionomer takes place on the entire catalyst layer. Source terms are defined assuming non-equilibrium between the gas phase and the ionomer phase such as

$$R_i = H_i \left(y_i^{eq} - y_i \right) \tag{52}$$

which represent the inequality between the adsorption and desorption processes for Na⁺.

Here we define H_j as the *cationic uptake coefficient* which represents the uptake of the cation in the ionomer of the fuel cell during operation. The sorption mechanism in an operating fuel cell is expected to be different than that in a cation exchange process in a membrane. The main difference between these two processes is that in the former, protons are generated and consumed in the catalyst sites and they can somehow resist the displacement exerted from the foreign cations because of the driving force due to the reaction. However, in the ion exchange process in a membrane, protons are *passive* and the uptake of the foreign cations in the membrane results in the displacement of the protons off of the exchange sites.

Small H_j means a slow sorption process. If the sorption process is too slow, little performance degradation is experienced during the fuel cell operation as the available sites will be mostly occupied by the protons. In this study, H_j is choosen such that similar performance degradation in the fuel cell operation reported by Mikkola et al 2 is achieved. However, to model the cationic uptake in an operating fuel cell precisely additional experiments need to be conducted and the exact determination of the cationic uptake coefficient remains as an open question.

In this study it is assumed that Na⁺ is found in the air mixtures as salt aerosols in sufficiently high amounts to completely occupy the charge carrying sites of the ionomer. On the other hand, it is assumed that there is no Na⁺ in the fuel mixture as the desorbed cations are instantly carried away from the vicinity of the ionomer due to strong convective flow. So the equilibrium values are determined as

$$y_{Na^{+}}^{eq} = \begin{cases} 0 & \text{at the anode} \\ 1 & \text{at the cathode} \end{cases}$$
 (53)

On the other hand when Na⁺ is to be found in the fuel stream, equilibrium values are chosen as 1 and 0 at the anode and cathode respectively.

Conservation of Ionic Charge

Linear combination of n-1 of Eq. 51 while each mass balance weighted by $F.z_i$ is

$$\nabla \cdot \left(F \sum_{j=1}^{\mathbf{n}-1} z_j \mathbf{N}_j \right) = F \sum_{j=1}^{\mathbf{n}-1} z_j R_j$$
 (54)

where the expression under the divergence operator is identified as the total ionic current density vector $\bf J$ and the right hand side is the source term defined as the volumetric current generation.

$$\nabla \cdot \mathbf{J} = Q_i \tag{55}$$

This equation replaces one of the mass balance equations, the one for H⁺ in our case.

Source terms for the H^+ are the rate of charge transfer. $j=i_a$ at the anode and $j=i_c$ at the cathode. Electrochemical kinetics of the anode is described as linear kinetics.

$$i_a = i_{0,a} \left(\frac{x_{H_2}}{x_{H_2}^{ref}} \right)^{1/2} \left(\frac{\alpha_a + \alpha_c}{RT} F \eta_a \right)$$
 (56)

 $i_{0,a/c}$ are the exchange current densities and $\Box_{a/c}$ are the reaction transfer coefficients for the anode and the cathode. Their values are listed in Table 3. Butler Volmer equation in the cathode is modified in order to account for the losses due to pH (proton concentration) gradient in the membrane ¹⁵.

$$i_c = i_{0,c} \left(\frac{x_{H^+}}{x_{H^+}^{ref}} \right) \left(\frac{x_{O_2}}{x_{O_2}^{ref}} \right) \exp \left(-\frac{\alpha_c}{RT} F \eta_c \right)$$
(57)

The modification accounts for the deviation from the standard state and the operating conditions. In the standard state there is a fixed proton concentration whereas in case of contamination there are gradients in the proton contentration. Activation overpotentials, η , are defined for the anode and the cathode as

$$\eta_{a/c} = \phi_e + \phi_i - U_{0,a/c} \tag{58}$$

where equilibrium voltage $U_{0,a/c}$ is defined as

$$U_{0,a} = \begin{cases} 0 & \text{at the anode} \\ 1.23 - 9 \times 10^{-4} (T - 298.15) & \text{at the cathode} \end{cases}$$
 (59)

Conservation of Electronic Charge

Electronic charge conservations is included in the model in the form of Ohm's Law,

$$-\nabla \cdot (\kappa_e \nabla \phi_e) = Q_e \tag{60}$$

Source terms are the same for electronic charge equation except the signs which distinguish between the charges of the protons and the electrons. Eq. 60 is solved in the GDLs and the CLs.

Boundary Conditions

Since the cationic uptake is assumed to be occurring in the entire catalyst region, it is modeled with source terms. Thus, insulation boundary conditions are used at all boundaries.

Also for the ionic charge transfer all boundary conditions are set to insulation,

$$\mathbf{n} \cdot (\kappa_i \nabla \phi_i) = 0 \tag{61}$$

On the other hand for the electronic charge conservation voltage boundary condition at the cathode GDL – bipolar plate interface and ground condition at the anode GDL – bipolar plate interface are prescribed to sort out current collection. The rest of the boundaries are treated as insulation.

Table XI Material Properties

Gas Diffusion Layers		
Porosity	0.78	26
Through-plane Electronic conductivity (S m ⁻¹)	12.5	26
In-plane Electronic conductivity (S m ⁻¹)	172.4	26
Through-plane thermal conductivity (W m ⁻¹ K ⁻¹)	1.7	26
In-plane thermal conductivity (W m ⁻¹ K ⁻¹)	23	26
Hydraulic permeability (m²)	2e-12	27
Density (kg m ⁻³)	440	26
Catalyst Layers		
Porosity	0.2	а
Ionomer volume fraction	0.26	27
Thermal conductivity (W m ⁻¹ K ⁻¹)	0.87	28
Hydraulic permeability (m²)	1e-12	a
Density (kg m ⁻³)	2100	28
Anode exchange current density (A m ⁻³)	3×10 ⁹	a
Cathode exchange current density (A m ⁻³)	3×10 ⁴	а
Anodic and cathodic transfer coefficients at the anode	$\Box_a = \Box_c = 1$	27
Cathodic transfer coefficients at the anode	□ <i>_c</i> =1	27
Membrane		
Thermal conductivity (W m ⁻¹ K ⁻¹)	0.259	29
Density (kg m ⁻³)	1980	29
Equivalent weight (EW)	1100	29

Effect of Cationic Contamination on the Electrochemical Performance of a PEFC

Cationic contamination of polymer electrolyte fuel cells (PEFCs) may cause serious degradation in cell performance which can sometimes be recoverable depending on the operating conditions and the exposure time but many times the process is irreversible. The source of the nonprotonic cations in the ionomer of the PEFC can be either fuel side or air side impurities. A broad range of impurities can be found in the fuel cell gas

streams such as residuals of the fuel reforming process, metal particles due to the corrosion of the hardware or salt particles suspended in the air.

In this section first a cation exchange process in a polymer electrolyte membrane (Nafion 117) will be investigated and the model equations will be validated with the experimental data acquired from open literature. Then the cation transport in an operating PEFC and its effects on the performance are going to be investigated.

Cation Exchange Process in a Polymer Electrolyte Membrane

To validate the contamination model, the predictions are compared with the experimental data of Sodaye et al.²³ who studied multicomponent adsorption of Na⁺ and Cs⁺ in a Nafion 117 membrane. They use radiotracers to track the temporal concentration changes of two cations in the membrane. Using equilibrating solutions of NaCl and CsCl with different molarities, they investigate the ion exchange process of the initially protonated (H⁺ form) Nafion membrane. With the solution containing NaCl/CsCl ratio of 1:1, they observe that at equilibrium only 17% of the available sites are occupied by Na⁺ while the rest is occupied by Cs⁺. This is explained by the high selectivity of the Cs⁺ compared to Na⁺ in a Nafion membrane. When the NaCl/CsCl ratio in the solution is 5:1 the Na⁺/Cs⁺ ratio in the membrane is 40% to 60% after a sufficient time period to reach the equilibrium.

To compare the model results with these experimental data, the cation transport model described previously is solved in same conditions to predict the Na⁺ and Cs⁺ uptake of the PEM. Equilibrium values are used as boundary conditions to Nernst Planck equations. Initial conditions are chosen such that the relative occupancy of H⁺ is unity while for the other cations it is zero since the membrane is initially in pure protonic form. The diffusivities of the cations in the membrane are taken from Yaeger et al.¹⁰ who reported that for the membrane in heteroionic form of Cs and Na, the diffusivities show great discrepencies from the values for the membrane in homoionic forms. This is attributed to the fact that aqueous self diffusivities and molecular weights of Na⁺ and Cs⁺ ions are not comparable.

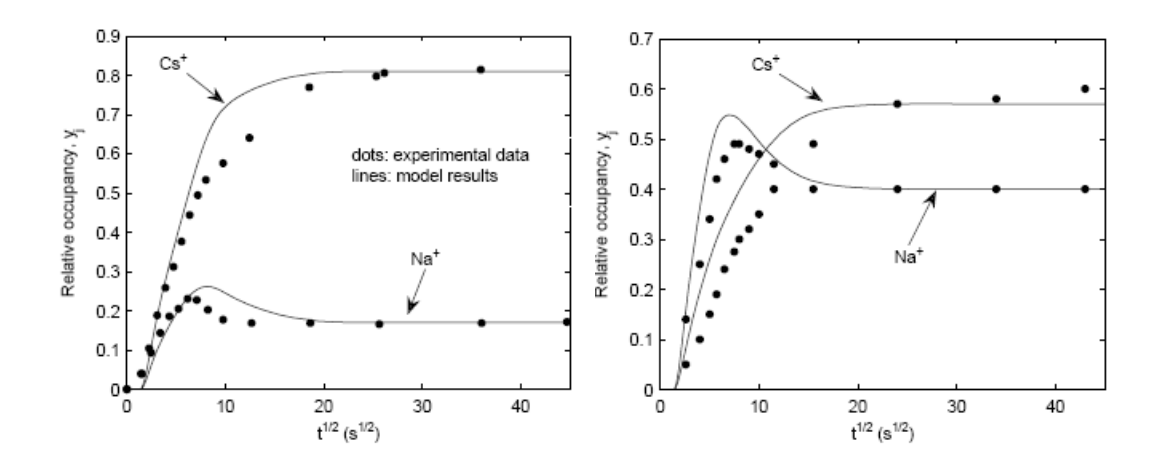


Figure 64 Transient Uptake of Na⁺ and Cs⁺ in the Nafion Membrane. a) For the Equilibrating Solution With NaCl/CsCl Ratio of 1:1 b) With NaCl/CsCl Ratio of 5:1. The Solid Lines Represent Model Results While the Markers Show the Experimental Data of Sodaye et al.

Figure 64a and 64b show the comparison of our model results with the experimental data for the solutions containing NaCl/CsCl ratio of 1:1 and 5:1, respectively. As shown, the model predictions are in good agreement with the experimental data. This is significant as no fitting parameters are used. Using diffusivity values reported for the membrane in the specific heteroionic form resulted in the match. As it is seen in these figures initially Na⁺ occupies more of the available sites than Cs⁺ does because of the greater diffusivity of the former. However, owing to the greater affinity of the Cs⁺ ions to the membrane, more of the sites are occupied by Cs⁺ ions after certain time when the process reaches steady-state. Initial bumps in Na⁺ occupancies can be explained by the non-ideality of the adsorption process due to Langmuir isotherms which results in temporal enhancement in species diffusion characteristics.

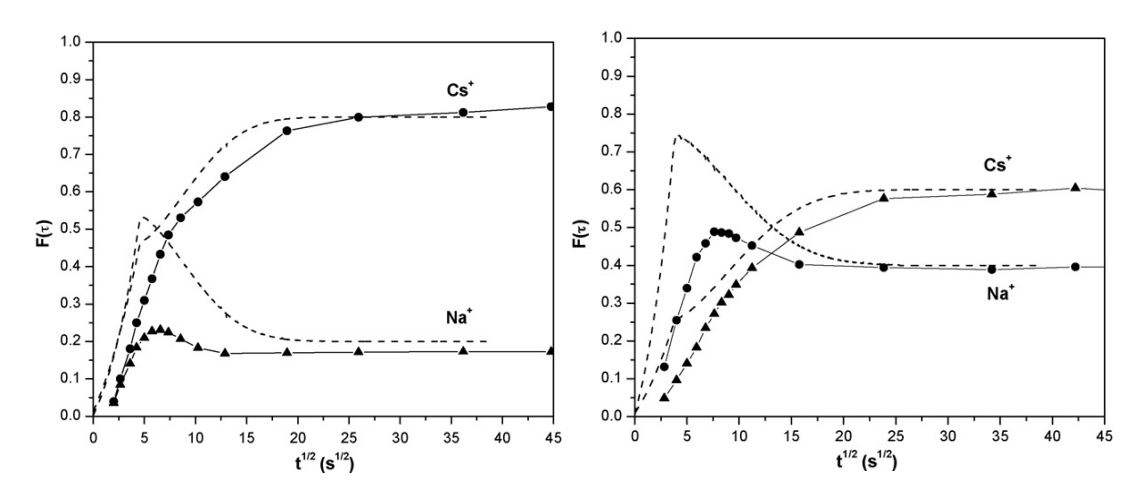


Figure 65 Model prediction of Sodaye et al for the Same Data Given in Figure 64.

On the other hand Figure 65a and 65b show the comparison of the same experimental data of Sodaye et al. 13 with their own model. $F(\tau)$ in these figures are called "fractional attainment of the equilibrium" which corresponds to what is defined as "relative occupancy: earlier. Comparing Fig. 64 and Fig. 65 it is observed that our model has an improved representation of the multicomponent ion exchange process in a Nafion membrane.

There are some significant differences between our model and that of Sodaye et al. The main difference is the diffusion coefficients used in both calculations. Sodaye et al. used diffusion coefficients for Na⁺ and Cs⁺ cation determined for membrane in each homoionic form. Membrane water content is different for each homoionic form and the diffusivities are related to these values. However, the diffusivities need to be corrected to account for the membrane water content in the mixed form. Another difference between two models is that they do not consider H⁺ in their multicomponent diffusion model and neglect the effects of gradients in the protonic occupancy on the other species. Finally, they do not account for the interactions between the cation pairs.

Although our model shows advances in representation of the multicomponent adsorption and the competitive ion exchange, it requires further improvements as the match between the model results and the experimental data is not exact. The first improvement might be in the diffusivity values used in the model. Although we claim that using Yaeger's data is a better approximation than the values used by Sodaye et al. it is not expected that the data is exactly up to date because Yaeger et al. 10 reported the values for a Nafion membrane which was fabricated in 1981. Even if the architecture of the membrane has not changed significantly, new experiments should be carried out to update the properties of the cations for a current membrane. Also, protonic conductivity

should be determined for the membrane in mixed ionic form because the value for the mixed form might differ from that determined for the membrane in pure H⁺ form. Finally the Maxwell-Stefan diffusivities for a species pair are determined via Eq. 29. Applicability of this equation can be argued. However, it is reported to be a good approximation for the diffusion in zeolite matrices which show similarities to the polymer electrolyte membrane in terms of mass transfer characteristics¹³.

Cation Transport in an Operating PEFC

Following the validation of the model with experimental data, the model is utilized to investigate the cationic transport and its effects during fuel cell operation. For that purpose two different cases of contamination are assumed: NaCl at the air stream and NaCl at the fuel stream. The operating conditions and the dimensions of the cell considered in these simulations are listed in Table XII.

Table XII: Geometrical and Operational Parameters

Fuel and air channel width Fuel and air channel depth ^a	0.5 mm 0.5 mm
Land area width	0.5 mm
GDL thickness	0.2 mm
CL thickness	10 □m
Membrane thickness (Nafion 112)	50.8 □m
GDL, CL and membrane depth ^a	1 mm
Fuel and air channel, GDL, CL and membrane length	50 mm
Anode and cathode inlet relative humidity	30/30 %
Operating temperature (°C)	80
Anode and cathode back-pressure (atm)	1

^a half of the actual depth is considered due to symmetry of the

Figure 66 shows the profiles for Na⁺ occupancy of the available sites in the MEA when only the air stream is contaminated. Profiles are drawn along the lines passing through the points both under the rib and under the channel. The lines where the profiles are investigated are shown in Fig. 63b. Line 1, 2 and 3 are for under the rib, mid-membrane

and under the channel respectively. Distribution of the cation in the MEA is governed by both concentration gradient and the potential field. While concentration gradient drives the species from cathode to anode, opposing to this, ionic potential field drives the cations from anode to cathode. Na⁺ is assumed to enter the MEA from the cathode and leave from the anode so Na⁺ concentration is greater at the cathode. In addition, ionic potential gradient causes migration of cations at the anode to the cathode and as a result, Na⁺ accumulates more at the cathode.

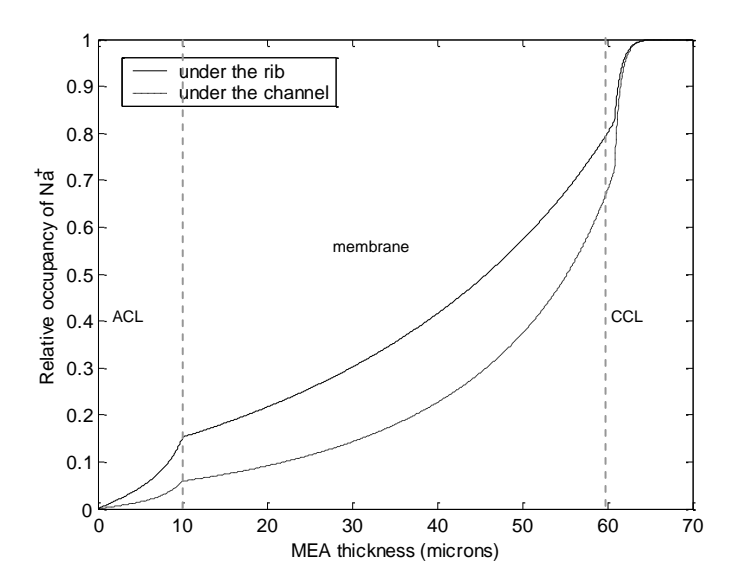


Figure 66 Na⁺ Relative Occupancy Distribution in the MEA During the Fuel Cell Operating at 0.7 V When the Contamination is in the Air Stream. Solid Line is the Profile Along Line 1 (Under the Rib) and Dashed Line is Along Line 3 (Under the Channel) Shown in Figure 63b.

Comparing the two profiles in Fig. 66, it is observed that Na^+ occupancy is higher under the rib areas. This is due to the enhanced diffusivity of Na^+ with the increased water content under the rib areas. Membrane water content is higher under the cathode current collector landing than that under the channel because water generated during the reaction has a longer path for diffusion. As a result, more water is accumulated under the current collector rib. Increased water content enhances the diffusivity of H^+ as well as Na^+ . However, it is assumed that the cathode reaction is slower than the Na^+ uptake in the model, which is controlled by H_j in Eq. 52. Indeed with an increased diffusivity Na^+ uptake will be faster. Increase in water content results in Na^+ being more advantageous for occupying the available sites of the catalyst layer. Thus, Na^+ concentration increases with the increased water content under the rib areas.

On the other hand if Na⁺ is in the fuel stream instead of air, the distribution is significantly different as seen in Figure 67. In this case, cations entering the MEA from the anode are carried to the cathode side and both concentration gradient and potential field work in the same direction. As a result a very big portion of the available sites in the MEA is occupied by the contaminant cations. This phenomenon is analogous to the mass transfer governed by both diffusion and advection. Similar to a species transfer in a flow field, distribution of the cation in the membrane is more uniform compared to that observed in the previous case when the contamination was introduced from the air side.

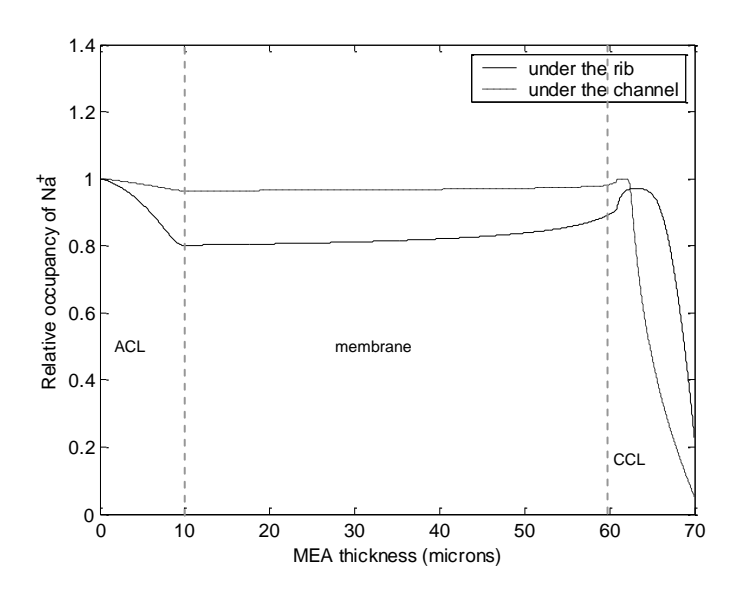


Figure 67 Na⁺ Relative Occupancy Distribution in the MEA During the Fuel Cell Operating at 0.7 V When the Contamination is in the Fuel Stream. Solid Line is the Profile Along Line 1 (Under the Rib) and Dashed Line is Along Line 3 (Under the Channel) Shown in Figure 63b.

Another difference between Fig. 64 and Fig. 65 is that Na⁺ occupancy is lower under the rib areas near the anode in the case when Na⁺ is in the fuel stream. This is related to the increase in water content under the anode current collector rib. Unlike the previous case when Na⁺ is in the air stream, the increase in water content under the cathode current collector rib areas results in greater Na⁺ occupancy. This can be explained by the distinct reaction kinetics at the anode and the cathode. Due to the fast anode reaction, increase in water content has a more positive effect on the H⁺ generation than

that on the Na⁺ uptake at the anode. However, due to the slower cathode kinetics, Na⁺ occupancy becomes larger with the increase in water content under the rib areas.

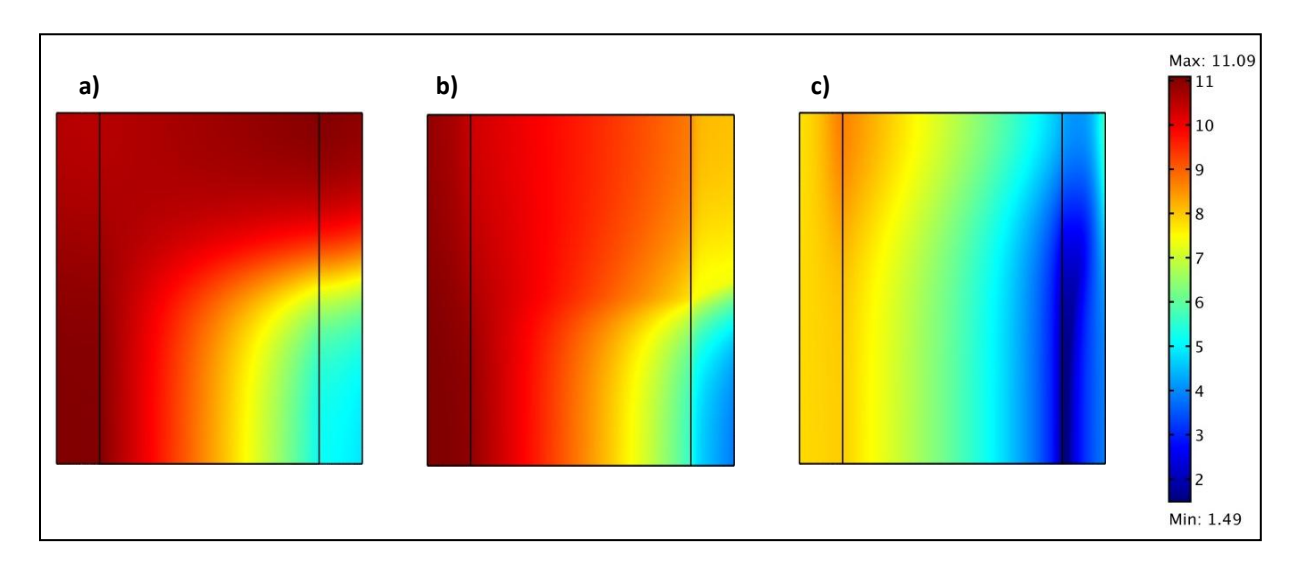


Figure 68 Water Content Distribution in the MEA for the Fuel Cell Operating at 0.7 V With 100/80 % Anode and Cathode Relative Humidities When a) Gases are Not Contaminated b) Contamination is in the Air Stream c) Contamination is in the Fuel Stream.

Cation distribution and the membrane water content are strongly coupled as the changes in one affect the other. While the diffusivities of the cations are strong functions of the membrane water content; electro-osmotic drag, water diffusivity and water sorption isotherms strongly depend on the cationic composition in the ionomer. Exchange of H⁺ with Na⁺ in the membrane results in higher electro-osmotic drag, lower water diffusivity and reduced water uptake. As a result membrane water content decreases with the contaminant cations existing in the MEA.

Figure 68 shows the membrane water content in the MEA for three different cases: a) when the gas streams are not contaminated, b) when Na^+ is on the air stream and c) when Na^+ is on the fuel stream. There is a small change between the non-contaminated case and the air side contaminated case while there is a significant difference when the contamination is at the anode side. The main effect of Na^+ is reducing the water sorption in the ionomer. As explained by Jalani and Datta²², water sorption in the membrane decreases due to various reasons: the reduction in the ionic hydration capacity, increase in the size of counter cation, decrease in the charge density, and the decrease in membrane swelling. In the case when the membrane is in pure Na form the equilibrium value for the membrane water content is λ =7.36 when gas phase water

activity is unity. Recall that this value is 14 for the protonated membrane (Nafion) at 30°C. Another significant effect of Na⁺ content in the membrane is on the electro-osmotic drag. When the membrane is in the pure Na form, electro-osmotic drag coefficient is reported to be 9.2 for pure water while this value is 2.6 in the pure H⁺ form membrane⁷.

For the non-contaminated case the water content is higher at the anode side as the anode stream is 100% humidified while the cathode is 80% humidified. Also as discussed before, water accumulation is more under the rib areas. For the second case when contamination is in the air stream, it is seen that the water content decreased at the cathode due to the significant occupation of the available sites by the foreign cations. However, at the anode side the water content is very similar to the noncontaminated case since Na⁺ occupation at the anode is much lower. The distribution is very different for the case when the contamination is at the fuel stream. At the anode when most of the sites are occupied by Na⁺, the water content reduces to 7.5 (even though the anode gas is fully humidified), close to the value for the membrane in Na form. As it will be discussed later, in case of contamination with Na⁺ at the fuel stream, current density drops to impractical values and as a result, water generation is negligible at the cathode. With the occupation of the available sites in the cathode by Na⁺, water content decreases to very low values such that dry-out is observed at the cathode membrane interface. Note that in the simulated case cathode inlet relative humidity is smaller than that for the anode.

Effect of the contamination on the fuel cell performance is both by the occupation of available sites by the foreign cations and the reduced water content hence decreased protonic conductivity. Figure 69 shows the anodic and cathodic transfer current densities for non-contaminated gases, contamination in the air stream and contamination in the fuel stream. Transfer current density may also be interpreted as the reaction rate. With the occupation of the available sites by the contaminant cations, reaction rate decreases. This drop is more significant when the contaminant is found at the fuel stream. For the case when the contamination is from the air stream the cathodic transfer current density increases near the membrane interface while the average is still lower than the value for non-contaminated case. Recalling Fig. 66 the cations accumulate in the cathode close to the GDL while occupying almost all the available sites and forcing the protons to accumulate near the membrane interface. The displacement of protons by sodium ions in the cathode means those catalytically active sites in the cathode are no longer utilized to generate current to be used by the external circuit; i.e. fuel cell reaction rate decreases. Hence, due to the displacement of the protons towards the membrane, the reaction rate is almost zero near the GDL while it is increased near the membrane interface.

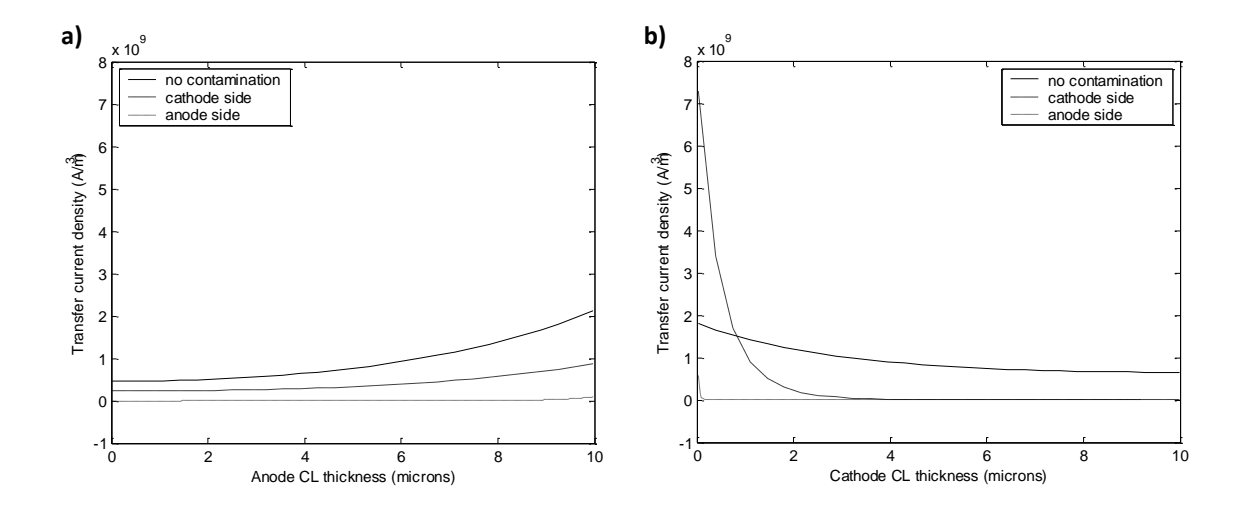


Figure 69 Transfer Current Densities a) at the Anode b) at the Cathode. Solid Lines Represent no Contamination, Dashed Lines Represent Cathode Side Contamination and Dotted Lines Represent Anode Side Contamination Cases. The Profiles are Drawn Along Line 2 Shown in Fig. 63.

For a better comparison of the effect of contamination on the cell performance protonic current densities are plotted in Figure 70. The average of the protonic current density over the membrane gives the operating current density of the cell at the specified voltage. It is predicted that presence of Na⁺ in the air channel results in a drop of current density from 0.9 to 0.7 A/cm² whereas for fuel side contamination the operating current density drops to 0.05 A/cm². For the cathode side contamination current density is greater at the lower half of the membrane while for the anode side contamination it is greater at the upper half corresponding to under the rib areas. This is because contaminant cations occupies more sites under the rib for cathode side contamination while for the anode side contamination it is vice versa as described in the previous paragraphs.

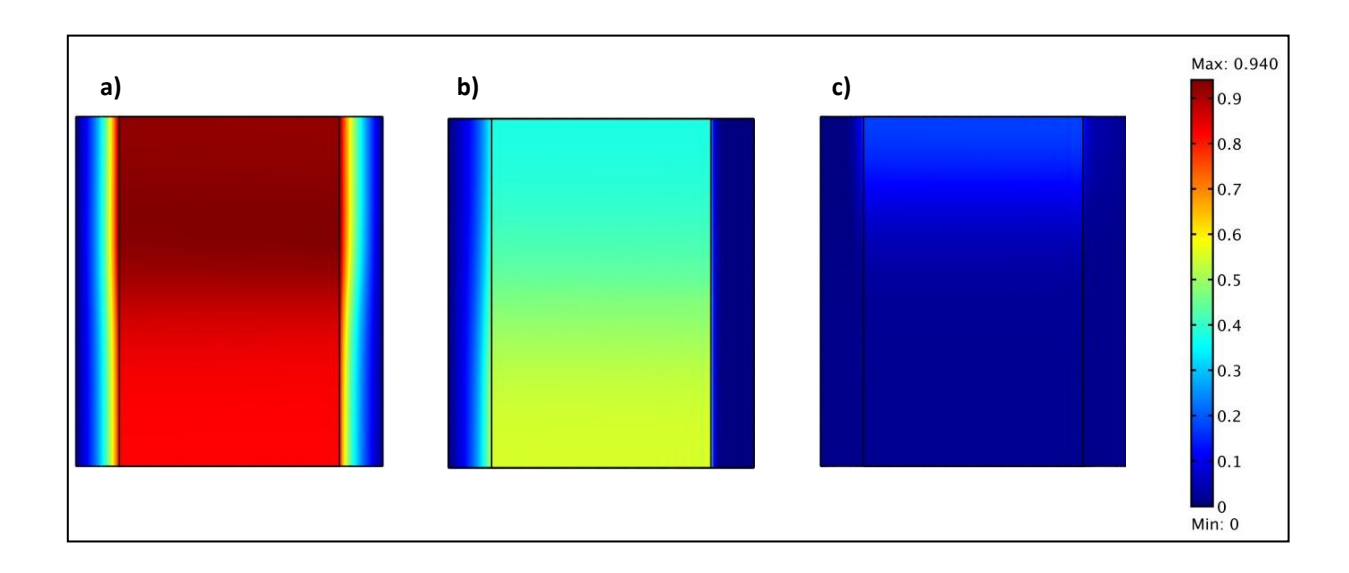


Figure 70 Protonic Current Density Distribution in the MEA for the Fuel Cell Operating at 0.7 V When a) Gases are Not Contaminated b) Contamination is in the Air Stream c) Contamination is in the Fuel Stream.

As mentioned previously, in a contaminated fuel cell performance also decreases due to the decreased water content. Decrease in water content results in a drop in self diffusivity of the protons hence the protonic conductivity, as a result the useful ionic current transmitted via protons decreases. In Figure 71 protonic conductivities are shown. Note that conductivity is a function of not only the water content but also protonic occupancy. For the cathode side contamination, the conductivity drops from 6.5 to 1 S/m at the membrane cathode interface while it drops from 9.5 to 7.8 S/m at membrane anode interface. Corresponding average protonic occupancies are 0.25 and 0.9 at the cathode and anode interfaces respectively. If the water content did not decrease with the Na⁺, the drop in the protonic conductivity would be solely due to occupation of the available sites by Na⁺. In such case the conductivity would decrease from 6.5 to 2.13 at the cathode interface and from 9.5 to 8.55 at the anode interface as implied by Eq. 31. Hence the rest of the drop in the conductivity is ascribed to the decrease in membrane water content. For the fuel side contamination, the protonic conductivity drops to very low values making the fuel cell generate impractically low current densities.

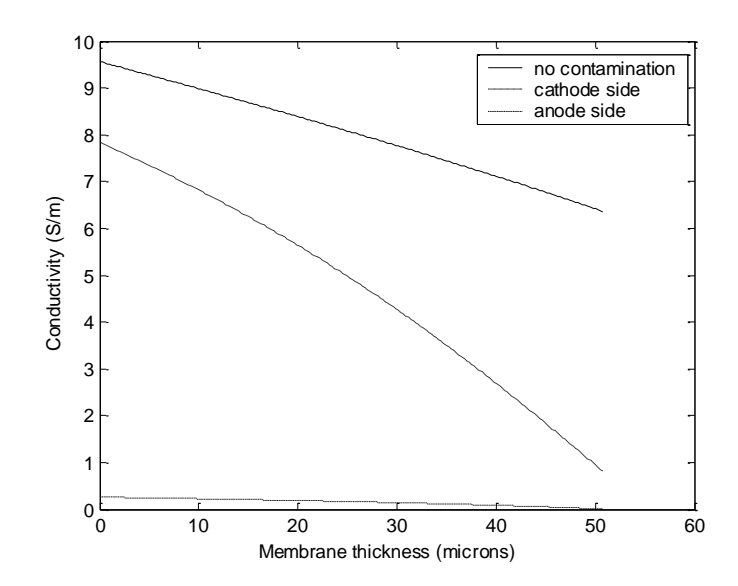


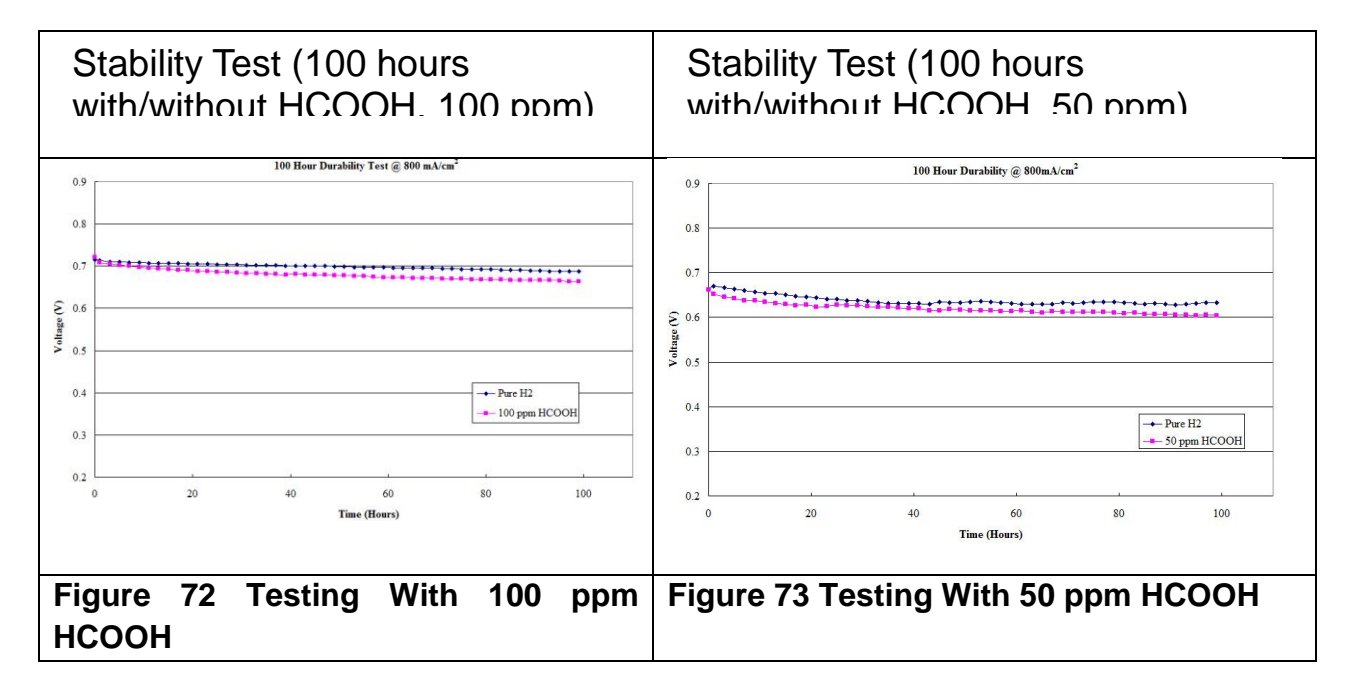
Figure 71 Protonic Conductivity Distribution in the Membrane Along Line 3 (Mid-Membrane) for the Fuel Cell Operating at 0.7 V. Solid Lines Represent no Contamination, Dashed Lines Represent Cathode Side Contamination and Dotted Lines Represent Anode Side Contamination Cases. The Profiles are Drawn Along Line 2 Shown in Fig. 63b.

5.0 Contaminant Model Validation

The cation transfer model is validated against the experimental data found in the open literature. For the validation, a cation exchange process in the polymer electrolyte membrane is investigated. Competitive adsorption of Na⁺ and Cs⁺ in a protonated membrane is studied. Then the equations describing the cation transfer in the membrane are implemented in the fuel cell model. Cation distributions in the membrane during the fuel cell operation are predicted. The effects of both air side and fuel side contamination on the electrochemical performance of the PEFC are addressed and the degradation in PEFC performance is predicted.

6.0 Novel Mitigation Technologies

Of the impurities that our team was assigned to investigate, namely hydrocarbons and halogenates, formic acid proved to have the most significant impact of the group on fuel cell performance. Our focus with regard to mitigation technologies was on 1) understanding the mechanism of performance impact, and 2) developing a means of mitigating this performance impact. Figure 72 shows significant performance degradation of the fuel cell with a formic acid concentration of 100 ppm. Figure 73 shows that this degradation is lessened, but still significant, with 50 ppm of formic acid.



100 hour stability tests with pure H_2 and 100 ppm HCOOH were conducted in H_2 . After operating with pure H_2 for 100 hours, the fuel cell is conditioned at 0.6 V for 12 hours. 100 ppm HCOOH is then introduced into H_2 and another 100 hour test is started. Each symbol in the figure is an average of two hour data points. The same tests were done with 50 ppm formic acid in hydrogen. Cross-over (CO) corrected CVs performed periodically during the 100 hour contamination period with 100 ppm HCOOH. The scan range is 0.05-1.0 V and rate is 20 mV/s. 4 cycles were recorded in each CV measurement. The cell is kept at open circuit at 80° C and 25 psig back pressure. Anode and cathode RH are 100% RH and 75% RH, respectively and flow rates are controlled at 250 sccm on both sides.

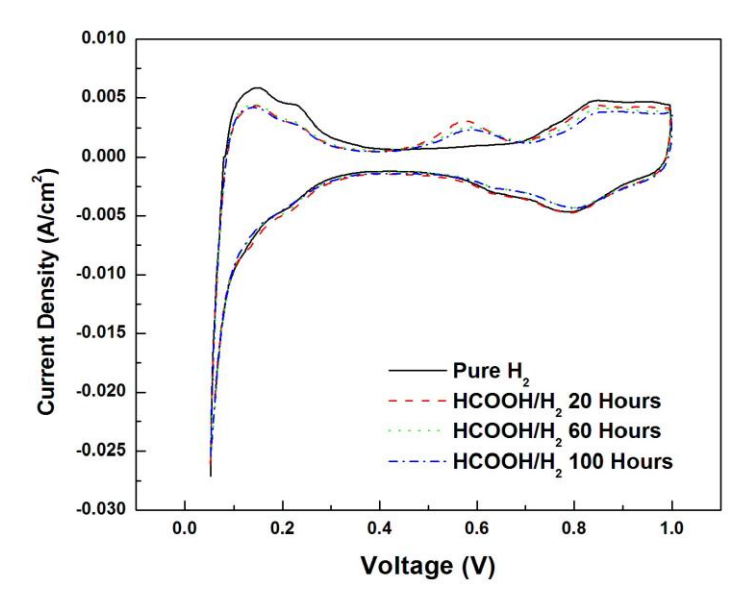


Figure 74 CO Corrected CV's

Cyclic voltammetry scans performed before and after contamination test show that ECA of the cathode decreased, signifying that HCOOH negatively affects the cathode catalyst layer. These data are shown below in Figure 75.

Scan Range	Scan Rate	Cycles	Flow Rates (A/C)	Temperatur	Pressure
				е	
0.05-0.6 V	20 mV/sec	4	250/250 sccm	Room	Ambient

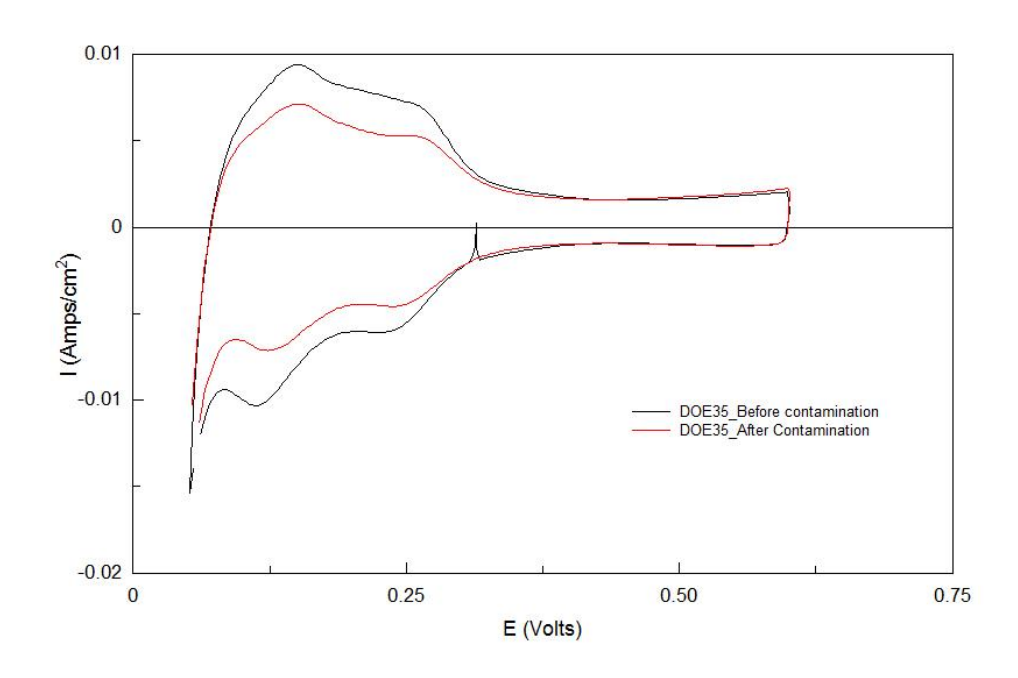


Figure 75 Cyclic Voltammetry Scans Conducted Before and After Contamination Events

1) Hot Cyclic Voltammetry Scans During Contamination and Recovery Period

CV scans were performed periodically (every 20 hours) during contamination and recovery period to provide more details of the contamination on the cathode. During CV scans, the cell temperature, the dew points, and the pressures remained unchanged. Pure nitrogen was passed across the cathode at 250 sccm while $HCOOH/H_2$ was passed across the anode at 250 sccm.

Scan	Scan Rate	Cycles	Flow	Rates	Cell	Dew	Pressure
Range			(A/C)		Temp	Points(A/C)	
0.05-0.6	20 mV/sec	4	250/250) sccm	80 °C	80/73 °C	25/25 psig
V							

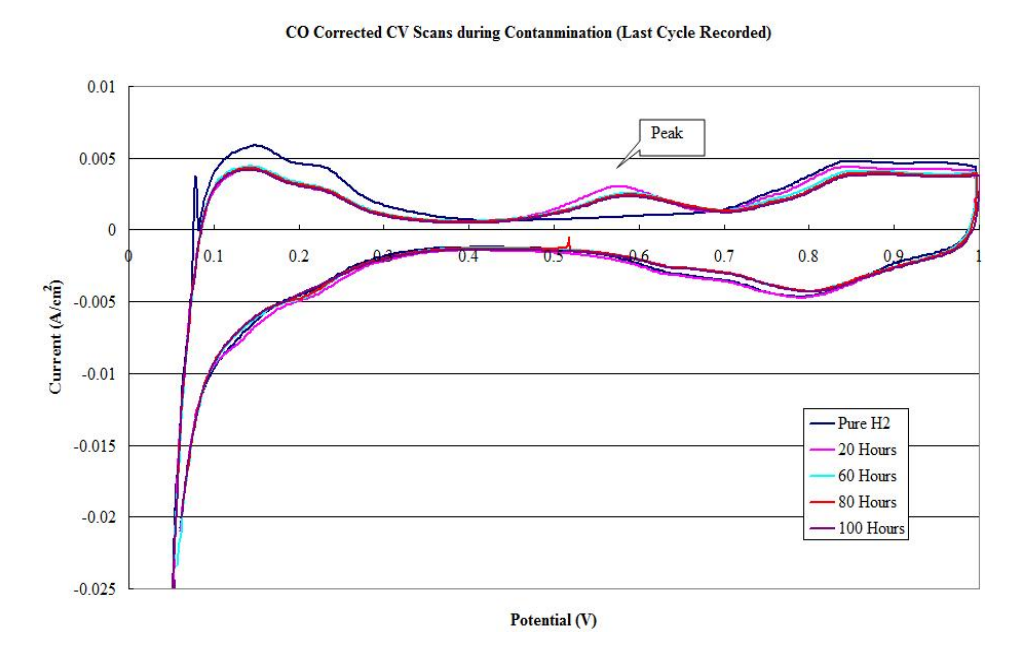


Figure 76 CV Scans Performed Every 20 Hours

CVs were performed every 20 hours to characterize any poison on the cathode. The last cycle of each scan is shown above. CVs show a decrease in H_2 absorption peaks and an oxidation peak at 0.6 V could be absorbents on Pt surface.

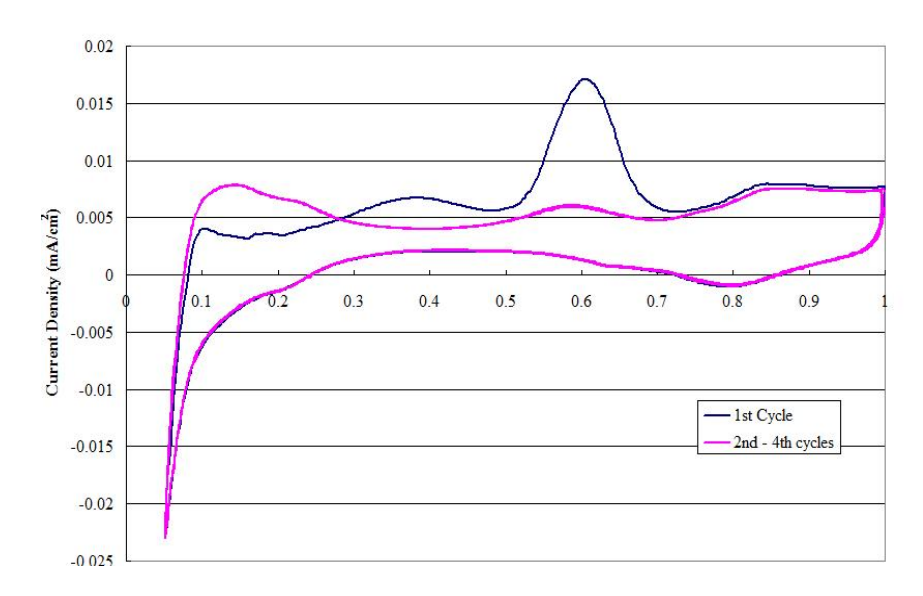


Figure 77 Example of Individual CV Scan

An example of individual CV scan is shown above. Each scan consists of 4 cycles. In the 1st CV cycle, the hydrogen absorption peak almost disappeared. Pt surface seems to be covered by absorbents (peaks at 0.4V and 0.6 V). The absorbent is oxidized around 0.4 V & 0.6 V (e.g. CO) in the 1st cycle. Therefore, in the next 3 cycles recovery of H_2 absorption peak is observed, but evidence of surface coverage still exists.

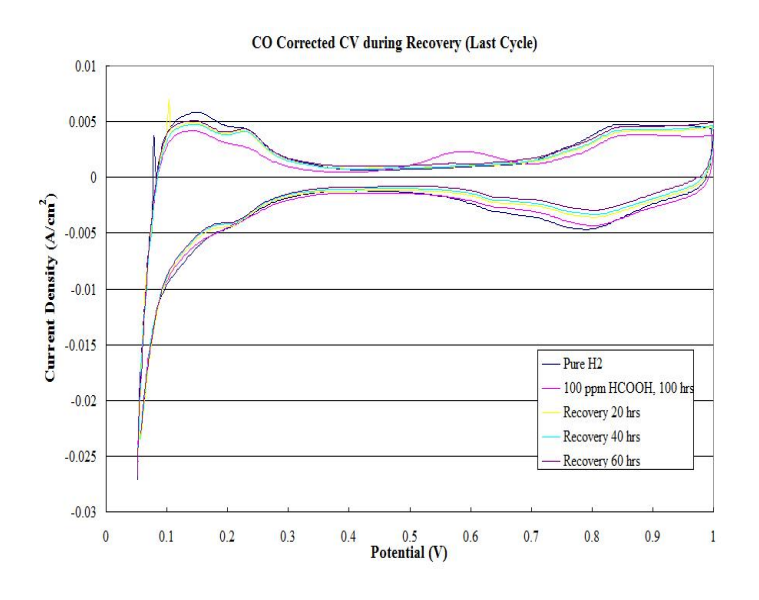


Figure 78 CV's Taken Every 20 Hours During the Recovery Period

After recovery with pure H₂ for 20 hours, hydrogen absorption peaks are partially recovered. Further running (up to 100 hrs) with pure H₂ does not result in further

recovery. Studies showed that formic acid can crossover the membrane and contaminate the cathode. The contamination cannot be fully recovered just by purging pure H_2 through the anode.

Disassembly and inspection of these cells revealed a spotting on the anode and cathode flow fields. The flow fields were exposed to air over two days and the spotting was no longer apparent on the flow fields indicating some organic material. Polar solvents were used in the past to lift the organic material and study it using FTIR, but were unsuccessful. Non-polar solvents failed to lift the material from the surface of the flow fields with much success, but our studies suggest that it may be paraformaldehyde.

There are three primary choices for means of dealing with any performance impact from formic acid impurities. These include developing improved materials that resist contaminating effects of the formic acid, changing the operating conditions such that performance impacts will be minimal or recoverable, and developing processes for cleaning up the contaminating species. We showed that the mechanism for formic acid contamination and performance impact is complex, affecting several different parts of the electrochemical cell. Therefore developing advanced materials that resist the effects of formic acid will very likely prove to be complex and expensive. Operating conditions can be influenced to a degree, but studies have shown that transient conditions in operating fuel cells, particularly for automotive applications, can be quite variable, and not easily controlled. Perhaps the easiest and most practical means of handling formic acid contamination involves cleaning up the process gas.

Experiments were conducted in an effort to remove the residual formic acid with water, and also with a solid sorbent. In this regard a laboratory absorption system was constructed from laboratory glassware. Experiments were run by bubbling the formic acid laden fuel stream through either a water bath or a solid powder sorbent and the amount of formic acid picked up and remaining in the fuel stream was analyzed. This configuration is shown in Figure 79.

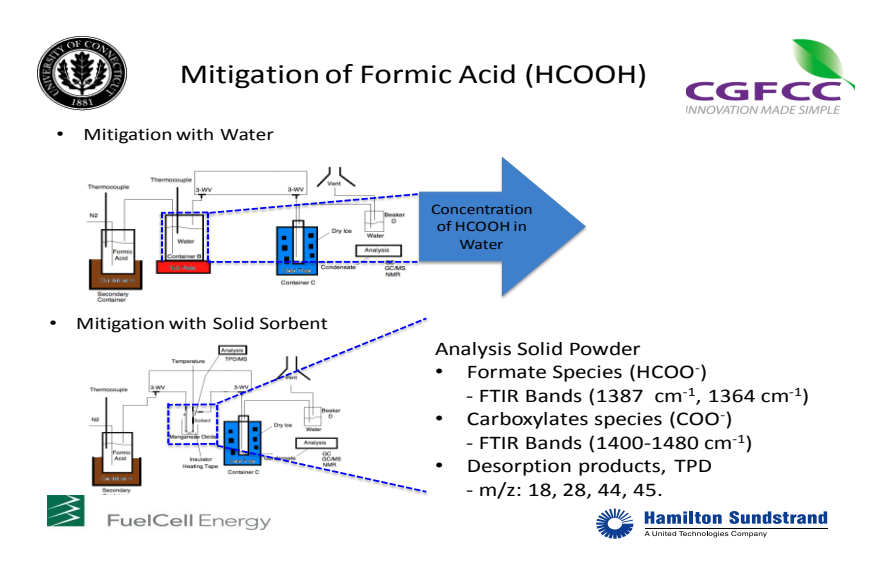


Figure 79 Evaluation of a Formic Acid Sorption Technique for Mitigation of the Effects of Formic Acid on Fuel Cell Performance

Results of these tests indicate that formic acid can be removed to manageable levels using these simple techniques. Feasibility in a viable system configuration may be worthwhile pursuing in future programs.

7.0 Outreach

As part of this program our team participated in several important outreach activities. Perhaps the most important was our participation in the hydrogen Fuel Quality Working Group (FQWG). In that regard, our focus was to characterize the effects of common hydrocarbon and halogenated hydrocarbon impurities on fuel cell performance. This was part of an organized, multi-laboratory effort to support the development of an ISO hydrogen fuel quality standard. Much of the testing for this program was done in support of this effort.

In addition, several papers, student theses, and conference proceedings were generated as part of this effort, in a concerted effort to disseminate results of these studies. Many of them are included in the list below.

Publications / Presentations:

- 1. "Effects of Impurities on Fuel Cell Performance and Durability", Presentation at the DOE Program Kickoff Meeting, February, 2007
- 2. "Effects of Impurities on Fuel Cell Performance and Durability", Poster Presented at the DOE Annual Merit Review, May, 2007.
- 3. "Effects of Impurities on Fuel Cell Performance and Durability", Presentation to FreedomCAR, November, 2007.
- 4. "Effects of Impurities on Fuel Cell Performance and Durability", Workshop Held by National Research Council, Canada, March, 2008.
- 5. "Effects of Impurities on Fuel Cell Performance and Durability", Presentation to the Fuel Quality Working Group, March/April, 2008.
- 6. "The Effects of Cationic Contamination on the Physio-Chemical Properties of Perfluoroionomer Membranes", Ph. D. Dissertation Defense by T. Molter, April, 2008
- 7. "The Effects of Cationic Contamination on the Physio-Chemical Properties of Perfluoroionomer Membranes", Ph. D. Dissertation by T. Molter, May, 2008
- 8. "Effects of Impurities on Fuel Cell Performance and Durability", Presentation at the DOE Annual Merit Review, June, 2008.
- 9. "Effects of Impurities on Fuel Cell Performance and Durability", Presentation to FreedomCAR, August, 2008.
- 10. "Effects of Impurities on Fuel Cell Performance and Durability", Modeling Workshop, Denver, CO, November, 2008.
- 11. "Fuel Cells and Transportation", School of Engineering Seminar Series, The University of Vermont, December, 2008.
- 12. "Evaluation of the Effects of Impurities on Fuel Cell Performance and Integrity", NRC Canada, February, 2009.
- 13. M.F. Serincan, U. Pasaogullari, T. Molter "Effect of cathode side cationic contamination on the performance of an operating PEFC", *Proceedings of 7th ASME International Fuel Cell Science, Engineering &Technology Conference,* 8-10 June, 2009 Newport Beach, CA.
- 14. X. Zhang, U. Pasaogullari, T. Molter, J. Preston, "Influence of Ammonia on Membrane-Electrode Assemblies in Polymer Electrolyte Fuel Cells", *Proceedings of 7th ASME International Fuel Cell Science, Engineering & Technology Conference*, 8-10 June, 2009 Newport Beach, CA.
- 15. M. F. Serincan, "Multiphysics Modeling of Fuel Cells", Ph.D. Defense, June, 2009.
- X. Zhang, H. Galindo, H. Graces, P. Baker, X. Wang, U. Pasaogullari, S. Suib, T. Molter, "Influence of Formic Acid Impurity on Proton Exchange Membrane Fuel Cell Performance", ECS Trans., 25 (1), 1633 (2009)
- 17.X. Zhang, M. Serincan, U. Pasaogullari, T. Molter. "Contamination of Membrane-Electrode Assemblies by Ammonia in Polymer Electrolyte Fuel Cells", *ECS Trans.*, 25 (1), 1565 (2009)

- 18. X. Zhang, U. Pasaogullari, T. Molter, "Influence of ammonia on membraneelectrode assemblies in polymer electrolyte fuel cells", Inter. J. of Hydrogen Energy, 34(22), 9188 (2009)
- 19. X. Zhang, H. Galindo, H. Garces, P. Baker, X. Wang, U. Pasaogullari, S. Suib, T. Molter, "Influence of Formic Acid Impurity on Proton Exchange Membrane Fuel Cell Performance", J. of Electrochem. Soc. 157 B409 (2010)

References

- R. Halseid, P.J.S. Vie, and R. Tunold, *Journal of Power Sources* **154,** 343 (2006).
- M.S. Mikkola, T. Rockward, F.A. Uribe, and B.S. Pivovar, *Fuel Cells* **2,** 153 (2007).
- H.J. Soto, W.K. Lee, J.W.V. Zee, and M. Murthy, *Electrochemical and Solid-State Letters* **6**, A133 (2003).
- F.A. Uribe, S. Gottesfeld, and T.A. Zawodzinski, *Journal of the Electrochemical Society* **149**, A293 (2002).
- ⁵ A. Goswami, A. Acharya, and A.K. Pandey, *J. Phys. Chem. B* **105**, 9196 (2001).
- T. Okada, Y. Ayato, H. Satou, M. Yuasa, and I. Sekine, *J. Phys. Chem. B* **105**, 6980 (2001).
- ⁷ T. Okada, H. Satou, M. Okuno, and M. Yuasa, *J. Phys. Chem. B* **106,** 1267 (2002).
- G. Pourcelly, P. Sistat, A. Chapotot, C. Gavach, and V. Nikonenko, *Journal of Membrane Science* 110, 69 (1996).
- ⁹ Z. Samec, A. Trojanek, J. Langmaier, and E. Samcova, *Journal of the Electrochemical Society* **144**, 4236 (1997).
- H.L. Yeager and A. Steck, *Journal of the Electrochemical Society* **128**, 1880 (1981).
- ¹¹ T. Okada, *Journal of Electroanalytical Chemistry* **465**, 1 (1999).
- ¹² T. Okada, *Journal of Electroanalytical Chemistry* **465,** 18 (1999).
- S. Sodaye, C. Agarwal, and A. Goswami, *Journal of Membrane Science* **314,** 221 (2008).

- ¹⁴ B.L. Kienitz, H. Baskaran, and T.A.Z. Jr, *Electrochimica Acta* **54**, 1671 (2009).
- T.A. Greszler, T.E. Moylan, and H.A. Gasteiger, in *Handbook of Fuel Cells Fundamentals, Technology and Applications* (John Wiley & Sons Ltd., 2009).
- ¹⁶ A.Z. Weber and C. Delacourt, *Fuel Cells*, 459 (2008).
- ¹⁷ R.E.D.L. Rue and C.W. Tobias, *Journal of the Electrochemical Society* **106**, 827 (1959).
- J.R. Wilke, *Journal of Physical Chemistry* **18**, 517 (1950).
- G. Suresh, S. Sodaye, Y.M. Scindia, A.K. Pandey, and A. Goswami, *Electrochimica Acta* **52**, 5968 (2007).
- H. Yasuda, C.E. Lamaze, and L.D. Ikenberry, *Macromolecular Chemistry* **118,** 19 (1968).
- J.T. Hinatsu, M. Mizuhata, and H. Takenaka, *Journal of the Electrochemical Society* **141**, 1493 (1994).
- N.H. Jalani and R. Datta, *Journal of Membrane Science* **264**, 167 (2005).
- T.E. Springer, T.A. Zawodinski, and S. Gottesfeld, *Journal of the Electrochemical Society* **136**, 2334 (1991).
- ²⁴ K.S. Forland, T. Okada, and S.K. Ratkje, *Journal of the Electrochemical Society* **140**, 634 (1993).
- Do, Chemical Engineering Science **56**, 4351 (2001).
- Toray Carbon Paper Specification Sheet (Toray Industries Inc., Advanced Composites Department, Tokyo, 2001).
- H. Ju, H. Meng, and C.Y. Wang, *International Journal of Heat and Mass Transfer* **48,** 1303 (2005).
- ²⁸ H. Wu and P. Berg, *Journal of Power Sources* **165**, 232 (2007).
- Product Information, DuPont Nafion PFSA Membranes N-112, NE-1135, N-115, N-117, NE-1110 Perfluorosulfonic Acid Polymer, NAE101 (DuPont, 2004).